

SANDIA REPORT

SAND91-1124 • UC-261

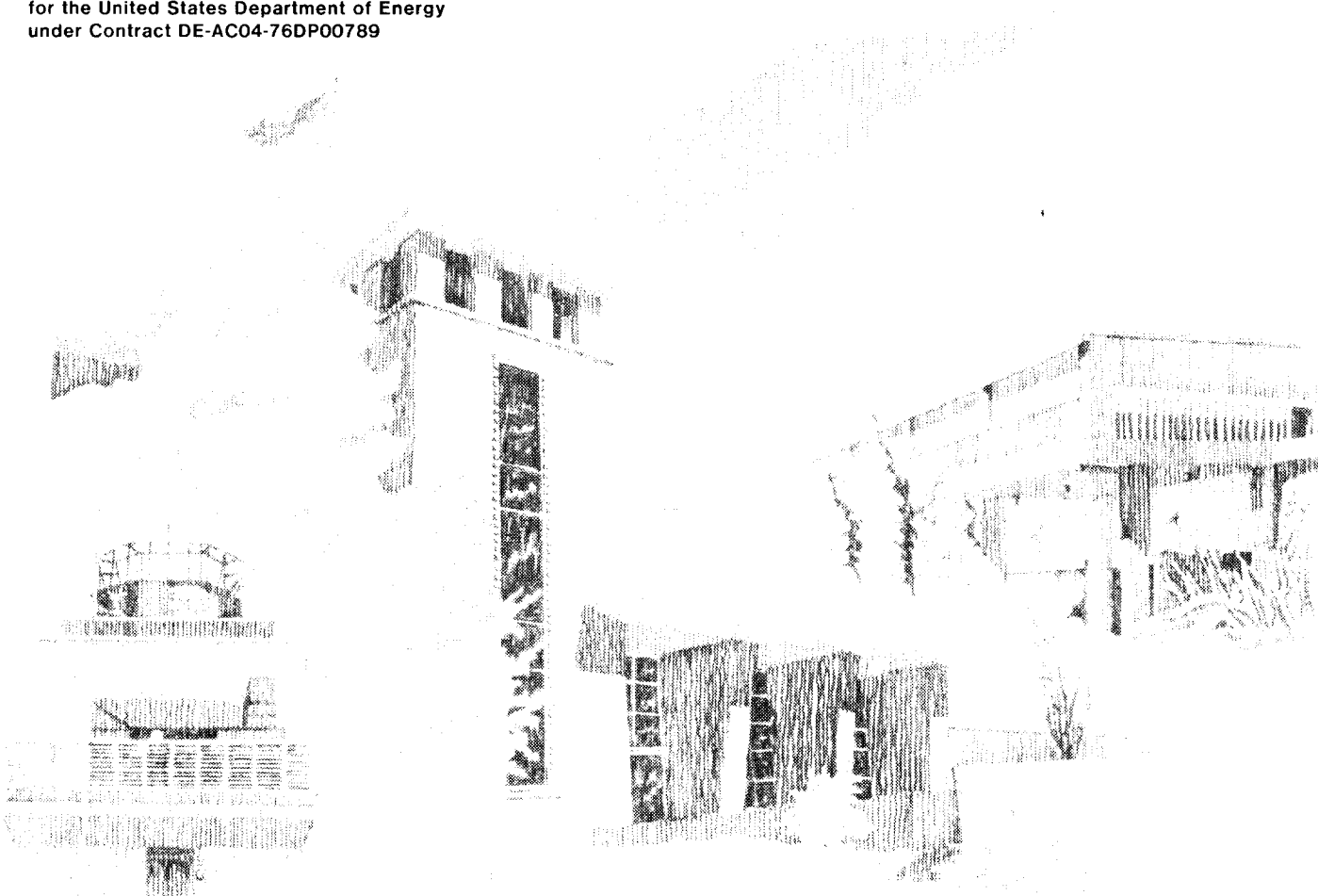
Unlimited Release

Printed September 1991

Numerical Simulation of VAWT Stochastic Aerodynamic Loads Produced by Atmospheric Turbulence: VAWT-SAL Code

Gregory F. Homicz

Prepared by
Sandia National Laboratories
Albuquerque, New Mexico 87185 and Livermore, California 94550
for the United States Department of Energy
under Contract DE-AC04-76DP00789



Issued by Sandia National Laboratories, operated for the United States Department of Energy by Sandia Corporation.

NOTICE: This report was prepared as an account of work sponsored by an agency of the United States Government. Neither the United States Government nor any agency thereof, nor any of their employees, nor any of their contractors, subcontractors, or their employees, makes any warranty, express or implied, or assumes any legal liability or responsibility for the accuracy, completeness, or usefulness of any information, apparatus, product, or process disclosed, or represents that its use would not infringe privately owned rights. Reference herein to any specific commercial product, process, or service by trade name, trademark, manufacturer, or otherwise, does not necessarily constitute or imply its endorsement, recommendation, or favoring by the United States Government, any agency thereof or any of their contractors or subcontractors. The views and opinions expressed herein do not necessarily state or reflect those of the United States Government, any agency thereof or any of their contractors.

Printed in the United States of America. This report has been reproduced directly from the best available copy.

Available to DOE and DOE contractors from
Office of Scientific and Technical Information
PO Box 62
Oak Ridge, TN 37831

Prices available from (615) 576-8401. FTS 626-8401

Available to the public from
National Technical Information Service
US Department of Commerce
5285 Port Royal Rd
Springfield, VA 22161

NTIS price codes
Printed copy: A04
Microfiche copy: A01

Numerical Simulation of VAWT Stochastic Aerodynamic Loads Produced by Atmospheric Turbulence: VAWT-SAL Code

Gregory F. Homicz
Computational Aerodynamics Division
Sandia National Laboratories
Albuquerque, N. M. 87185-5800

Abstract

Blade fatigue life is an important element in determining the economic viability of the Vertical-Axis Wind Turbine (VAWT). A principal source of blade fatigue is thought to be the stochastic (*i.e.*, random) aerodynamic loads created by atmospheric turbulence. This report describes the theoretical background of the VAWT Stochastic Aerodynamic Loads (VAWT-SAL) computer code, whose purpose is to numerically simulate these random loads, given the rotor geometry, operating conditions, and assumed turbulence properties. A Double-Multiple-StreamTube (DMST) analysis is employed to model the rotor's aerodynamic response. The analysis includes the effects of Reynolds number variations, different airfoil sections and chord lengths along the blade span, and an empirical model for dynamic stall effects. The mean ambient wind is assumed to have a shear profile which is described by either a power law or a logarithmic variation with height above ground. Superimposed on this is a full 3-D field of turbulence: *i.e.*, in addition to random fluctuations in time, the turbulence is allowed to vary randomly in planes perpendicular to the mean wind. The influence of flow retardation on the convection of turbulence through the turbine is also modeled. Calculations are presented for the VAWT 34-m Test Bed currently in operation at Bushland, Texas. Predicted time histories of the loads, as well as their Fourier spectra, are presented and discussed. Particular emphasis is placed on the differences between so-called "steady-state" (mean wind only) predictions, and those produced with turbulence present. Somewhat surprisingly, turbulence is found to be capable of either increasing or decreasing the average output power, depending on the turbine's tip-speed ratio. A heuristic explanation for such behavior is postulated, and a simple formula is derived for predicting the magnitude of this effect without the need for a full stochastic simulation.

ACKNOWLEDGEMENTS

The author wishes to express his appreciation to Dr. Henry Dodd, Supervisor of the Wind Energy Research Division, for the programmatic support and encouragement he provided during the course of this work. He is also indebted to Drs. Dale Berg, Paul Klimas, and Paul Veers for numerous technical discussions, and to Drs. Berg, William Oberkampf, and James Strickland for their review of this manuscript.

CONTENTS

	ACKNOWLEDGEMENTS.....	4
	CONTENTS	5
	LIST OF FIGURES	6
	NOMENCLATURE	7
1	INTRODUCTION	11
2	AERODYNAMIC MODEL	13
	2.1 Rotor Geometry and Grid Definition	13
	2.2 DMST Analysis	15
	2.3 Dynamic Stall Model	18
	2.4 Massé Modification	20
3	STEADY-STATE RESPONSE	21
	3.1 Mean Wind Shear.....	21
	3.2 Iterations for Interference Factors	21
	3.3 Loading Calculation	23
4	STOCHASTIC RESPONSE	25
	4.1 3-D Turbulence Simulation	25
	4.2 Turbulence Convection	31
	4.3 Loading Calculations	34
5	RESULTS AND DISCUSSION	38
	5.1 Case 1: 20.1 m/sec (45 mph), 10% Turbulence	39
	5.2 Case 2: 20.1 m/sec (45 mph), 30% Turbulence	47
	5.3 Case 3: 8.9 m/sec (20 mph), 10% Turbulence.....	50
	5.4 Case 4: 8.9 m/sec (20 mph), 30% Turbulence.....	55
	5.5 Effect of Turbulence on Average Output Power	58
	5.6 Run Times	63
6	CONCLUSIONS & SUGGESTIONS FOR FUTURE WORK	64
	REFERENCES	66

LIST OF FIGURES

Figure 1.	VAWT Rotor Geometry and Grid	13
Figure 2.	Magnified View of the n^{th} Blade Element	14
Figure 3.	Turbulence Simulation Grid	26
Figure 4.	Spatial Interpolation Cell for Turbulence	34
Figure 5.	Transformation of Nodal Loads to Frame Rotating with Blade 1	36
Figure 6.	DOE/USDA 34-m VAWT Test Bed	38
Figure 7.	Aerodynamic Interference Factors for Cases 1 and 2	40
Figure 8.	Streamwise Turbulence in Stationary Frame for Case 1	41
Figure 9.	Streamwise Turbulence in Rotating Frame for Case 1	42
Figure 10.	Variations in Angle-of-Attack for Case 1	44
Figure 11.	Mean and Ensemble-Averaged Rotor Torque vs. θ for Case 1	44
Figure 12.	Maximum Relative Error vs. Number of Samples for Case 1	45
Figure 13.	Instantaneous Rotor Torque vs. θ for Case 1	46
Figure 14.	Mean and Ensemble-Averaged Rotor Torque PSD for Case 1	46
Figure 15.	Variations in Angle-of-Attack for Case 2	48
Figure 16.	Mean and Ensemble-Averaged Rotor Torque vs. θ for Case 2	48
Figure 17.	Maximum Relative Error vs. Number of Samples for Case 2	49
Figure 18.	Instantaneous Rotor Torque vs. θ for Case 2	49
Figure 19.	Mean and Ensemble-Averaged Rotor Torque PSD for Case 2	50
Figure 20.	Aerodynamic Interference Factors for Cases 3 and 4	51
Figure 21.	Variations in Angle-of-Attack for Case 3	52
Figure 22.	Mean and Ensemble-Averaged Rotor Torque vs. θ for Case 3	53
Figure 23.	Maximum Relative Error vs. Number of Samples for Case 3	53
Figure 24.	Instantaneous Rotor Torque vs. θ for Case 3	54
Figure 25.	Mean and Ensemble-Averaged Rotor Torque PSD for Case 3	54
Figure 26.	Variations in Angle-of-Attack for Case 4	55
Figure 27.	Mean and Ensemble-Averaged Rotor Torque vs. θ for Case 4	56
Figure 28.	Maximum Relative Error vs. Number of Samples for Case 4	57
Figure 29.	Instantaneous Rotor Torque vs. θ for Case 4	57
Figure 30.	Mean and Ensemble-Averaged Rotor Torque PSD for Case 4	58
Figure 31.	Steady-State Performance Curve for Constant Ω	59
Figure 32.	Turbine Power Sensitivity to Turbulence, S_t	61

NOMENCLATURE

a	interference factor; ratio of local to incoming wind speed
A	projected area of the rotor in the (y,z) plane, Eq. (5)
A_M	empirical constant in Massé modification to Gormont model, Eq. (33)
B	number of blades
c	blade chord length; also used as a dimensionless constant in Eqs. (67), (70)
C	coherence decay coefficient, Eq. (53)
C_L, C_D	sectional lift and drag coefficients
C_P	performance coefficient, $P / ((1/2) \rho V_{eq}^3 A)$
C_N, C_T	sectional normal and tangential force coefficients
f	frequency
$f(a)$	iteration function defined by Eq. (37)
F_x	x-component of force exerted on a streamtube
$F(a), G(a)$	functions defined by DMST analysis, Eqs. (27) and (28)
\mathbf{H}	spectral influence matrix, Eqs. (55)–(56)
i	integer index used to delineate time and/or azimuthal intervals, Eq. (2); also used to represent $\sqrt{-1}$
i_r, i_c	integer indices referring to rows and columns, respectively, of the turbulence simulation grid, Fig. 3; $i_r = 1, \dots, N_{ver}$ and $i_c = 1, \dots, N_{hor}$
i_{rev}	integer index used to number revolutions within a sample, $i_{rev} = 1, \dots, N_{rev}$
i_{sam}	integer index used to number samples within the ensemble, $i_{sam} = 1, \dots, N_{sam}$
j, k	integer indices used for rows and columns, respectively, of the matrices \mathbf{S} and \mathbf{H} , Eqs. (54) and (56)
K_1	empirical coefficient in Gormont model, Eq. (29)
l_s	spanwise length of a blade element
n	exponent (not necessarily integer) used to characterize local topography in power law, Eq. (35)
N	force normal to the blade section, Fig. 1
N_{hor}, N_{ver}	number of horizontal, vertical elements in rectangular array of turbulence simulation points, Fig. 3
N_{be}	number of blade elements defined by node points, $N_{node} - 1$
N_{node}	number of blade node points at which aerodynamic loads are to be computed, $N_{be} + 1$
N_{pts}	number of turbulence simulation points, $N_{hor} \times N_{ver}$, Fig. 3
N_{ran}	number of time points in the loading simulation for each sample, $N_{rev} \times N_\theta$

N_{rev}	number of revolutions in a sample
N_{sam}	number of samples in the ensemble
N_{turb}	number of discrete time points in turbulence simulation
N_{θ}	number of θ increments, or time intervals, in one revolution
p^+, p^-	pressures on the up/downwind faces of actuators
P	turbine output power
r	radial coordinate from the rotor axis in a horizontal (x, y) plane
R	force directed radially inward from blade to axis of rotation; the horizontal component of N , Fig. 1
R_{eq}	equatorial radius
Re	Reynolds number, Wc/ν
s	spanwise coordinate along the blade
S_{jk}^u, S_{jk}^v	cross-spectral density of u, v turbulence between points j and k ; Eqs. (51)–(52)
S_t	turbine power sensitivity to turbulence, Eq. (79)
\mathbf{S}	spectral density matrix, Eq. (54)
t	time used to describe turbine motion, Eq. (2); also used for airfoil thickness in Eq. (30)
t_{ts}	time used in turbulence simulation, Eq. (66)
Δt	time interval used for turbine motion, Eq. (1)
Δt_{ts}	time interval used in turbulence simulation, Eqs. (67) and (70)
T	tangential force along path of rotation, Fig. 1
\mathcal{T}	torque
u, v, w	turbulent velocity components along x, y, z respectively
V	local mean wind speed
V_{eq}	ambient wind speed at equatorial height
V_{ref}	ambient wind speed at reference height, z_{ref}
W	relative velocity sensed by a blade element, Eq. (17)
x, y, z	Cartesian coordinate system, with $x > 0$ pointing upwind, Fig. 1
\mathbf{X}	diagonal matrix of white-noise inputs used in turbulence simulation, Eq. (58)
z_o	a roughness height used to characterize topography, Eqs. (34) and (50)
z_{ref}	reference height at which wind speed is input

Greek

α_g	geometric angle-of-attack, Eq. (18)
$(\alpha_{ref})_{L,D}$	reference angle-of-attack used by Gormont model to transform C_L and C_D , Eq. (29)
α_{ss}	steady-state stall angle
β	azimuthal spacing between blades, $2\pi/B$
γ_L, γ_D	empirical functions used by Gormont model to transform lift and drag, Eqs. (29) and (30)
γ_{jk}	coherence between fluctuations at points j and k , Eq. (52)
δ	blade inclination angle from vertical, Fig. 1
θ	azimuthal angle in a horizontal (x, y) plane; $\theta = 0$ when looking into the wind, and increases in a counter-clockwise direction
λ, μ	exponents used to adjust decay of coherence with f and Δr , Eq. (53)
ν	air kinematic viscosity
σ_u, σ_v	rms turbulence intensities, Eq. (49)
ρ	air density
Φ_{kq}	random phase of q^{th} harmonic in turbulence simulation, Eq. (60)
χ	reference tip-speed ratio, $\Omega R_{eq}/V_{ref}$
Ω	rotor angular velocity
ξ	dimensionless spanwise integration variable along a blade element

Subscripts

∞	refers to ambient, or freestream conditions ahead of the rotor
$a1, a2$	refer to aerodynamic control points on a blade element, Fig. 2
b	refers to a load integrated over the b^{th} blade, $b = 1, \dots, B$
el	refers to a load integrated over a blade element, $el = 1, \dots, N_{be}$
m	refers to the midpoint of a blade element, Fig. 2; also used as an integer index in Eq. (60) to delineate discrete turbulence values
n	refers to the n^{th} blade node, Fig. 2, or the loading at that node, $n = 1, \dots, N_{node}$
q	refers to q^{th} harmonic in turbulence simulation
t	refers to a load integrated over the whole turbine
ts	refers to quantity used in turbulence simulation
u, d	refers to conditions at the upwind/downwind actuator, respectively

Superscripts

G	refers to airfoil characteristics as modified by Gormont dynamic stall model
M	refers to Massé modification to Gormont model predictions
S	refers to steady-state two-dimensional airfoil characteristics
T	transpose of a matrix

Miscellaneous

$(\dot{\quad})$	time derivative
$(\overline{\quad})$	time-averaged quantity
$\langle \quad \rangle_E$	ensemble-averaged quantity
$\langle \quad \rangle_S$	sample-averaged quantity

1 INTRODUCTION

The past 10–15 years have witnessed a resurgence of interest in the Vertical-Axis Wind Turbine (VAWT). The VAWT offers several advantages when compared to the more conventional Horizontal-Axis (HAWT) machines. The VAWT is inherently omnidirectional, and hence obviates the need to provide a yawing mechanism for keeping the machine turned into the wind. The transmission and electrical generation equipment can be located at ground level, thus tending toward a simpler, lighter structure. The VAWT is also better able to withstand high winds. In one sense, the price paid for structural simplicity is aerodynamic complexity: VAWT aerodynamics is inherently unsteady, and highly nonlinear. However, the relatively recent development of several methods capable of predicting steady-state performance has greatly increased our understanding of VAWT aerodynamics.

Another factor that has come to play an important role in determining the economic viability of such machines is their expected lifetime. Turbine blades have been known to fail due to structural fatigue after as little as 2–3 years, despite having been designed for a fatigue life many times that. This has proven to be a problem for both HAWT and VAWT designs. The steady-state performance codes on which these designs are based assume the ambient wind does not vary with time. In the case of a VAWT, this means that each blade's angle-of-attack, and hence the aerodynamic loads, will vary cyclically, with a period equal to a time span of one revolution. The spectrum of such a load-time history consists of the fundamental frequency, Ω , and its harmonics—the so-called 'per rev' frequencies—with no excitation between them. However, carefully resolved experimental load spectra show excitation at frequencies intermediate between these frequencies, suggesting that random loads are being generated which destroy the periodicity. The most likely source of these random, or stochastic, loads is turbulence in the atmosphere, which is often neglected on the grounds that the effects of such random fluctuations will average out to zero in the long run. The results to be presented here will show that this is not always the case. Furthermore, blade fatigue is inherently a local phenomenon which is impacted by the blades' load distribution with respect to both position and frequency.

Recent attempts to predict stochastic loads have included analyses in both the frequency and time domains. Frequency domain analysis is predicated on being able to form the total system response as a linear superposition of the response to individual harmonic components of the wind. It is restricted to situations where the unsteady aerodynamic response is linear, and can be viewed as a small perturbation of the otherwise steady aerodynamic loading. Such conditions can be reasonably argued in the case of the HAWT, particularly if mean wind shear and tower wake effects are neglected. A good example of frequency domain analysis applied to the HAWT can be found in Ref. [1]. On the other hand, VAWT aerodynamics, even without turbulence present, is characterized by large variations in angle-of-attack, often as much as $\pm (20^\circ\text{--}30^\circ)$. The blades then are operating in a stalled condition much of the time, and if the fluctuations are rapid enough, the hysteresis phenomenon known as *dynamic stall* may occur. Such nonlinear phenomena require that the simulation be carried out in the time domain. References [2], [3], and [4] are good examples of this type of analysis.

The present model is an extension of the earlier SWILT model developed by Veers[2]. New features include the ability to accommodate different chord lengths and airfoil sections along the blade span, the influence of Reynolds number variations in both space and time, and the inclusion of an empirical model for dynamic stall behavior. References [5] and [6] describe an earlier version of the present model, which followed Veers[2] in using a simple 1-D turbulence simulation. This

version also assumed that the interference factors (Sections 2 and 3.2 below) were independent of azimuth. Both simplifications have now been relaxed. The model and results described here employ a full 3-D turbulence simulation, using the method first outlined by Veers in Ref. [2], and later described in more detail in Ref. [7]. The interference factors are also now allowed to vary with azimuth as well as elevation. Though the principal motivation for the development of this model was to provide inputs to structural analysis codes capable of predicting fatigue, the discussion here will focus more on the aerodynamic aspects.

The next section describes the aerodynamic analysis used. Section 3 describes how this analysis is applied to the prediction of the turbine's steady-state performance, *i.e.*, its response to a steady, mean wind. Section 4 then discusses the simulation of a random, three-dimensional turbulence field, and the stochastic loads that it generates. Numerical results are presented in Section 5 for the 34-m VAWT Test Bed operating in Amarillo, Texas. Finally, Section 6 draws conclusions from the predictions made thus far, and makes suggestions for future work.

2 AERODYNAMIC MODEL

Two of the most successful approaches for predicting VAWT performance are the Double Multiple-StreamTube (DMST) analysis, as typified by Ref. [8], [9], and [10], and the vortex method, e.g., Ref. [11]. Comparisons of code predictions using both methods with experimental data have appeared in the literature[12],[13]. The approximate DMST analysis is able to predict the periodic loads and average output power about as well as the more refined vortex models. The latter can provide more details of the flow within the turbine than the DMST models, but consume considerably more computer time. Since stochastic analyses in the time domain require long record lengths to reduce statistical scatter, the DMST method was chosen. The model used here most closely resembles that developed by Paraschivoiu, and embodied in his CARDA and CAARDAV computer codes[8].

2.1 Rotor Geometry and Grid Definition

A right-handed Cartesian (x, y, z) coordinate system is depicted with a schematic of the rotor in Fig. 1. Its origin is at the intersection of the rotor axis with the ground. The positive x -axis points

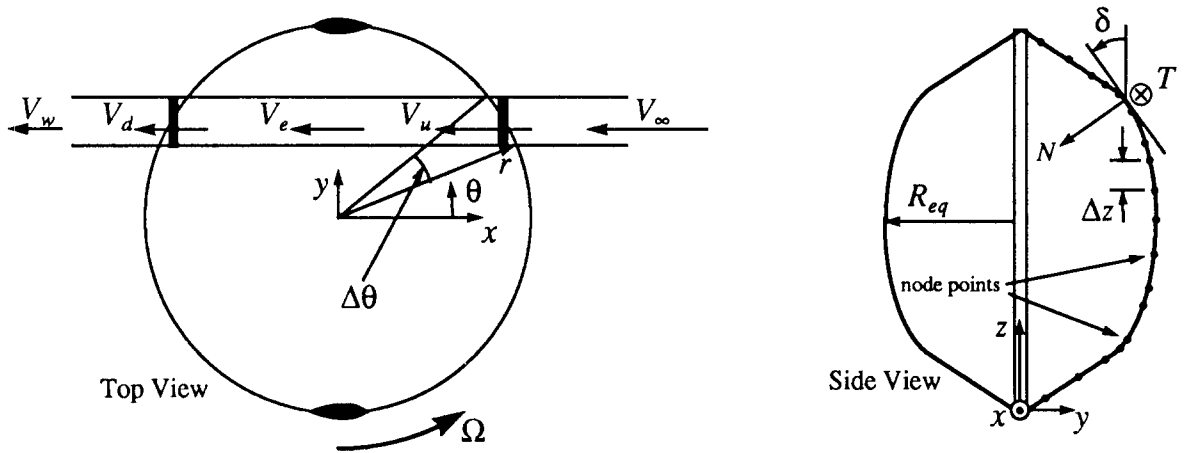


Figure 1. VAWT Rotor Geometry and Grid

into the oncoming wind, with the y -axis in the lateral direction; the z -axis points vertically up from the ground. The rotor is assumed to operate at a constant angular velocity, Ω . In the horizontal plane, the blades' path is divided into N_θ equal increments, each of angular width

$$\Delta\theta = (2\pi)/N_\theta = \Omega\Delta t, \quad (1)$$

at which the loading is to be evaluated. Once Ω and N_θ are specified, the above relation defines both $\Delta\theta$ and Δt . The direction $\theta = 0$ is parallel to the positive x -axis, and θ increases going counter-clockwise. Thus,

$$\theta = \theta_0 + i\Delta\theta \quad \text{at} \quad t = i\Delta t \quad (2)$$

where we arbitrarily take $\theta_0 = -\pi/2 - \Delta\theta/2$. For reasons that will become clear in Section 3.3, N_θ should be chosen to be a multiple of the number of blades, B .

In the side view shown in Fig. 1, the blade *node points* at which aerodynamic loads are to be calculated are shown schematically with a “•”. A total of N_{node} such points are read in, typically from a NASTRAN file, with an associated (r_n, z_n) coordinate pair for each point, $n = 1, \dots, N_{node}$.

The nodal coordinates serve to define the blade shape; the same set of node points is used for all B blades. The span between adjacent node points will be referred to as a *blade element*; the n^{th} element is bracketed by the n and $n+1$ node points, the count starting at the bottom of a blade and going upward. There are a total of $N_{be} = N_{node} - 1$ such elements. A blade element sweeps out a horizontal slice through the turbine with each revolution. The intersection of each such slice with the azimuthal sectors defined above delineates the set of ‘Multiple StreamTubes’ from which the analysis derives its name. The passage of one such streamtube through the rotor is shown schematically in Fig. 1.

The node points do *not* need to be uniformly spaced, and in general will not be. However, the analysis does assume that the aerodynamic cross-section and the chord length, both of which are specified by the user, are constant over each blade element. Designs employing step changes in section and/or chord along the span can still be accommodated by placing a node point wherever such a change occurs. In this way, the section properties and chord for the elements on either side of the discontinuity remain uniform.

A magnified view of a single blade element is shown in Fig. 2. For the purposes of the iterations

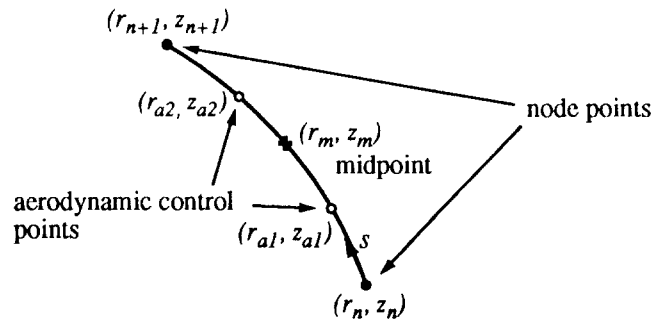


Figure 2. Magnified View of the n^{th} Blade Element

described in Section 3.2, we need the coordinates of the midpoint, which are calculated from:

$$\begin{aligned} r_m &= (r_n + r_{n+1}) / 2 \\ z_m &= (z_n + z_{n+1}) / 2 \quad n = 1, \dots, N_{be} \end{aligned} \quad (3)$$

Also required for the analysis are the inclination angle from the vertical, δ (*cf.* Fig. 1),

$$\delta = \tan^{-1} \left(\frac{r_n - r_{n+1}}{z_{n+1} - z_n} \right), \quad (4)$$

and the cross-sectional area, A , that the turbine presents to the oncoming wind:

$$A = 2 \int_{z_{\min}}^{z_{\max}} r dz \quad (5)$$

where z_{\min} and z_{\max} are the heights of the lowest and highest nodes, respectively. The integral is approximated from the set of (r_n, z_n) coordinates using the trapezoidal rule.

2.2 DMST Analysis

The loading on a blade element depends on the local relative velocity, which is the resultant of the *local* wind speed, V , and the rotational motion, Ωr . But V depends on how much the turbine has retarded the ambient wind, which in turn is a function of the blade load. To break this circular cycle of dependence, Double-Multiple-StreamTube (DMST) analysis uses a combination of actuator disc and blade element theories. As depicted in Fig. 1, each streamtube intersects the blades' path twice, once on the upwind pass, and again on the downwind pass. At these intersections we imagine the turbine replaced by a tandem pair of actuator discs, upon which the flow may exert a force—hence the ‘Double’ modifier in the method’s name.

Consider for the moment just the upwind actuator. As shown in Fig. 1, the flow velocity far upstream is V_∞ . How this is determined will be discussed in Section 3.1, but for now we will assume it is given. The local wind speed at the actuator is denoted by V_u , and that far downstream (the “equilibrium” value) is V_e . Since the turbine is extracting energy from the wind, it follows that $V_e < V_u < V_\infty$. The actuator can sustain a pressure difference across it, and hence has the following streamwise force exerted on it by the fluid:

$$\overline{\Delta F_{x,u}} = (p_u^+ - p_u^-) \Delta A \quad (6)$$

where p_u^+ and p_u^- are the pressures on the up/downwind faces of the actuator, respectively, and ΔA is the streamtube area.

By applying Bernoulli’s equation between the far upstream station and the actuator, and between the actuator and the downstream equilibrium conditions, we get:

$$\begin{aligned} \frac{1}{2} \rho V_\infty^2 + p_\infty &= \frac{1}{2} \rho V_u^2 + p_u^+ \\ \frac{1}{2} \rho V_u^2 + p_u^- &= \frac{1}{2} \rho V_e^2 + p_\infty \end{aligned} \quad (7)$$

Using these to substitute for p_u^+ and p_u^- in Eq. (6) yields:

$$\overline{\Delta F_{x,u}} = \frac{1}{2} \rho (V_\infty^2 - V_e^2) \Delta A \quad (8)$$

By Newton’s Law, $\overline{\Delta F_{x,u}}$ must also equal the mass flux through the actuator times the net velocity change:

$$\overline{\Delta F_{x,u}} = (\rho V_u \Delta A) (V_\infty - V_e) \quad (9)$$

Equating (8) and (9) gives

$$V_u = \frac{1}{2} (V_\infty + V_e) \quad \text{or,} \quad V_e = 2V_u - V_\infty \quad (10)$$

This is the well-known result that the velocity at the actuator is the average of the far upstream and downstream values. Using Eq. (10) in (9), and noting that (neglecting streamtube divergence) $\Delta A = \Delta z r \Delta \theta \cos \theta$, we obtain:

$$\overline{\Delta F_{x,u}} = 2\rho r \Delta \theta \Delta z \cos \theta V_u (V_\infty - V_u) \quad (11)$$

Equation (11) represents the force on the actuator in terms of global velocity changes. Next, we look ‘inside’ the actuator and recognize that it is a rotating blade element which is responsible for the loads. We need to relate the streamwise force it experiences to the airfoil’s tabulated aerodynamic characteristics. From simple analytic geometry (*cf.* Fig. 1), one can write the instantaneous streamwise force on the element as:

$$\Delta F_x = \Delta F_N \cos \delta \cos \theta + \Delta F_T \sin \theta \quad (12)$$

where ΔF_N and ΔF_T are the normal and tangential components, respectively, of the incremental force. In terms of the sectional force coefficients,

$$C_N = \frac{\Delta F_N}{(1/2) \rho W^2 \Delta A_b} \quad C_T = \frac{\Delta F_T}{(1/2) \rho W^2 \Delta A_b} \quad , \quad (13)$$

where $\Delta A_b = c \Delta z / \cos \delta$ is the incremental blade element area, and W is the relative velocity sensed by the element; the latter will be defined shortly. For the upwind actuator, this becomes:

$$\Delta F_{x,u} = \frac{1}{2} \rho W_u^2 \frac{c \Delta z}{\cos \delta} [C_N \cos \delta \cos \theta + C_T \sin \theta] \quad . \quad (14)$$

This equation is for the instantaneous force experienced while a blade element is between $\theta \pm (\Delta \theta) / 2$; when no blade is present the force is zero. For a rotor with B identical blades, a given streamtube during one revolution will feel B such ‘blips’, each of duration $\Delta \theta / \Omega$, with an amplitude given by the right-hand side of Eq. (14). Time-averaging such a variation results in an additional multiplicative factor of $(B \Delta \theta / 2\pi)$:

$$\overline{\Delta F_{x,u}} = \rho W_u^2 \left(\frac{B \Delta \theta}{4\pi} \right) \left(\frac{c \Delta z}{\cos \delta} \right) [C_N \cos \delta \cos \theta + C_T \sin \theta] \quad . \quad (15)$$

Assuming the blade chord is tangent to the path of rotation, the unknown coefficients C_N and C_T are related to the more usual lift and drag coefficients, and the geometric angle-of-attack, α_g , through:

$$\begin{aligned} C_N &= C_L \cos \alpha_g + C_D \sin \alpha_g \\ C_T &= C_L \sin \alpha_g - C_D \cos \alpha_g \end{aligned} \quad (16)$$

C_L and C_D can be determined on a quasi-steady basis by interpolation in tables of two-dimensional airfoil characteristics as functions of α_g and $Re = Wc/\nu$ [14]. For the general case with turbulence present, W and α_g are given by:

$$W = \left\{ [\Omega r - (V + u) \sin \theta - v \cos \theta]^2 + [(V + u) \cos \theta - v \sin \theta]^2 \cos^2 \delta \right\}^{1/2} \quad (17)$$

$$\alpha_g = \tan^{-1} \left\{ \frac{[(V + u) \cos \theta - v \sin \theta] \cos \delta}{\Omega r - (V + u) \sin \theta - v \cos \theta} \right\} \quad (18)$$

where the turbulence components, (u, v) , will be discussed in Section 4; for the present discussion, they may be assumed to be zero. Equations (17) and (18) are written here without the subscript ‘ u ’ because they apply at either actuator location. When Eq. (18) is rewritten in nondimensional form, it becomes clear that α_g is largely determined by the local dimensionless speed ratio $(\Omega r / V)$. If one assumes that the principal θ dependence arises from the terms explicitly involving $\cos \theta$ and $\sin \theta$,

it can be shown that in the limit $(\Omega r)/V \gg 1$, the maximum/minimum excursions in α_g are approximately given by $(\alpha_g)_{max} \approx -(\alpha_g)_{min} \approx \tan^{-1}(\Omega r/V)^{-1} \approx (\Omega r/V)^{-1}$ rad. As will be seen in Section 5, this turns out to be a better approximation for $(\alpha_g)_{max}$, which occurs on the upwind blade passage, than for $(\alpha_g)_{min}$, which occurs on the downwind blade passage. The reason is that such a simplified analysis neglects the fact that V also depends on θ .

Once V_u is specified, Eqs. (17) – (18) define W_u and α_g , and hence C_N and C_T . Thus Eqs. (11) and (15) represent a pair of equations in the two unknowns V_u and $\Delta F_{x,u}$; the latter is easily eliminated. By introducing the upstream *interference factor*¹,

$$a_u \equiv \frac{V_u}{V_\infty} , \quad (19)$$

we obtain the following equation for a_u :

$$\frac{Bc}{8\pi r} \left[C_N \cos\theta + C_T \frac{\sin\theta}{\cos\delta} \right] \left(\frac{W_u}{V_u} \right)^2 a_u^2 = a_u (1 - a_u) \cos\theta . \quad (20)$$

If the assumption is made that a_u depends on z , but can be treated as independent of θ , the above equation can be integrated from $\theta = -\pi/2$ to $\pi/2$, and results in Eqs. (11)–(12) of Ref. [6]. In this case a single iteration process is sufficient to determine a_u in each horizontal slice during the upwind blade passage; the resulting a_u applies to each streamtube in that slice. The analysis has since been generalized so that a_u can vary with both z and θ , *i.e.*, a different a_u applies in each streamtube. Equation (20) then can be manipulated into the following form:

$$a_u = \frac{1}{1 + G_u(a_u)} \quad (21)$$

where the function $G_u(a_u)$ is understood to depend implicitly on z and θ , and is given by:

$$G_u(a_u) = \frac{Bc}{8\pi r \cos\theta} \left[C_N \cos\theta + C_T \frac{\sin\theta}{\cos\delta} \right] \left(\frac{W_u}{V_u} \right)^2 . \quad (22)$$

Equations (21) and (22) apply only to the upwind actuator in each streamtube, $-\pi/2 \leq \theta \leq \pi/2$. a_u can be found by iteration (*cf.* Section 3.2 below), and then the equilibrium wind speed far downstream of the upwind actuator is determined by Eq. (10). This serves as the incoming wind sensed by the downwind actuator (Fig. 1), for which an analysis paralleling that described above can be carried out. Analogous to Eq. (10), one obtains for the local wind speed at the downwind actuator, V_d :

$$V_d = \frac{1}{2} (V_e + V_w) \quad \text{or,} \quad V_w = 2V_d - V_e . \quad (23)$$

Defining a downwind interference factor by

$$a_d = \frac{V_d}{V_e} , \quad (24)$$

¹The reader is cautioned that the literature sometimes refers to this as the *induction factor*. Also, some investigators prefer to work with the interference factor defined as $1 - V_u/V_\infty$.

the equation which a_d must satisfy is

$$a_d = \frac{1}{1 + G_d(a_d)} \quad , \quad (25)$$

where

$$G_d(a_d) = \frac{-Bc}{8\pi r \cos\theta} \left[C_N \cos\theta + C_T \frac{\sin\theta}{\cos\delta} \right] \left(\frac{W_d}{V_d} \right)^2 \quad . \quad (26)$$

Equations (25) and (26) apply to the downwind actuators, $\pi/2 \leq \theta \leq 3\pi/2$.

By making use of absolute values, the governing equations for both the upwind and downwind interference factors may be written in a common form:

$$a_{u,d} = \frac{1}{1 + G_{u,d}(a_{u,d})} \equiv F(a_{u,d}) \quad , \quad (27)$$

where

$$G_{u,d}(a_{u,d}) = \frac{Bc}{8\pi r |\cos\theta|} \left[C_N \cos\theta + C_T \frac{\sin\theta}{\cos\delta} \right] \left(\frac{W_{u,d}}{V_{u,d}} \right)^2 \quad . \quad (28)$$

The double subscripts ‘ u,d ’ indicate the equations’ applicability to either the up- or downwind actuator, as determined by θ . Equations (27) and (28) are the main results of this section. The primary difference between these results and Eqs. (11)–(12) of Ref. [6] is the absence of an integral over θ in the above. This is because the present equations are solved anew for each streamtube, rather than averaging over all the streamtubes in a given horizontal slice. The iteration procedure used to accomplish this will be discussed in Section 3.2.

2.3 Dynamic Stall Model

The use of static (*i.e.*, steady) airfoil characteristics in Eq. (16) needs to be augmented for low values of the reference tip-speed ratio, $\chi = \Omega R_{eq}/V_{ref}$. Equation (18) then predicts angles-of-attack well beyond the static stall margin, and the hysteresis phenomenon known as *dynamic stall* comes into play. This will most likely manifest itself first near the blade roots, where the local tip-speed ratio, $\Omega r/V_{u,d}$, can be considerably less than χ . Berg[15] and Paraschivoiu[10] demonstrated improved agreement with turbine performance data by employing the empirical model proposed by Gormont[16], and for this reason it has been incorporated in the present model. Only an outline of the major elements of the Gormont model will be given here, for the sake of completeness. For details and justification for the particular form of the empirical relations, the reader is advised to consult Ref. [16].

Let α_g denote the instantaneous geometric angle-of-attack, as predicted from Eq. (18). The essence of the Gormont model is the transformation of this angle into a so-called reference angle-of-attack, α_{ref} , given by:

$$(\alpha_{ref})_{L,D} = \alpha_g - K_1 \gamma_{L,D} \sqrt{\left| \frac{c\alpha_g}{2W} \right|} \operatorname{sgn}\dot{\alpha}_g \quad , \quad (29)$$

where the subscripts L and D refer to the fact that a different α_{ref} is used for predicting the dynamic lift and drag¹. $\dot{\alpha}_g$ is the time derivative of α_g , which is approximated numerically by a first-order backward difference between α_g and its value at the previous time step, α_{old} . K_1 is an empirical constant which takes on the value 1.0 for $\dot{\alpha}_g > 0$, and 0.5 when $\dot{\alpha}_g < 0$. $\gamma_{L,D}$ is an empirical function of the local Mach number, M , and the airfoil section's thickness-to-chord ratio, t/c , whose form depends on whether the lift or drag is being transformed:

$$\begin{aligned} (M_1)_L &= 0.4 + 5 \left(0.06 - \frac{t}{c}\right) & (M_1)_D &= 0.2 \\ (M_2)_L &= 0.9 + 2.5 \left(0.06 - \frac{t}{c}\right) & (M_2)_D &= 0.7 + 2.5 \left(0.06 - \frac{t}{c}\right) \\ (\gamma_{max})_L &= 1.4 - 6 \left(0.06 - \frac{t}{c}\right) & (\gamma_{max})_D &= 1.0 - 2.5 \left(0.06 - \frac{t}{c}\right) \end{aligned} \quad (30)$$

$$\gamma_{L,D} = (\gamma_{max})_{L,D} - \left[\frac{M - (M_1)_{L,D}}{(M_2)_{L,D} - (M_1)_{L,D}} \right] (\gamma_{max})_{L,D}$$

The transformed values of the lift and drag coefficients are then obtained from:

$$C_L^G = \left[\frac{C_L^S(\alpha_{ref_L})}{(\alpha_{ref_L} - \alpha_{L=0})} \right] \alpha_g \quad (31)$$

$$C_D^G = C_D^S(\alpha_{ref_D}) \quad (32)$$

The superscript “ S ” is used to denote the two-dimensional, steady-state airfoil characteristics. For the present analysis, these are tabulated for each airfoil section as functions of Re and α (*cf.* Sheldahl & Klimas[14]); bilinear interpolation is used to evaluate them for intermediate values. The superscript “ G ” is used to denote the values modified according to the Gormont rule. $\alpha_{L=0}$ represents the zero-lift angle-of-attack; the present analysis assumes symmetrical airfoil sections, and hence this quantity is zero.

Equations (29)-(32) introduce a dependence of the loading on both the magnitude and sign of $\dot{\alpha}_g$, in addition to α_g . In this way, they are able to empirically mimic the airfoil's hysteresis response. Specifically, when $\dot{\alpha}_g > 0$, they have the effect of reducing the angle-of-attack at which the data tables are entered—in effect, moving the airfoil further away from stall. Conversely, when $\dot{\alpha}_g < 0$, the reference angle-of-attack is increased, *i.e.*, the airfoil is moved closer to, or more deeply into, stall. Equation (31) adjusts the effective lift-curve slope to that appropriate to α_{ref_L} . Let α_{ss} represent the static stall angle, by which we mean the angle below which the section lift characteristics are *strictly linear*. Then if α_g and α_{ref_L} are both less than α_{ss} , it follows that $C_L^G = C_L^S$; only if one or the other of these angles exceeds α_{ss} will the lift be modified. In general, the drag will be modified in any event.

Two caveats should be mentioned in connection with the use of the Gormont model. It is very important that the static lift characteristics be strictly linear below α_{ss} . Otherwise, use of the above transformations can lead to physically inappropriate discontinuities in C_L^G vs. α_g . It is also

¹Gormont[16] refers to lift and moment stall, using the subscripts L and M . But his rule for transforming the drag coincides with that for the moment, and in the present application L and D are more meaningful.

necessary that Eqs. (29)–(32) be used at *all* angles-of-attack, not simply for angles above α_{ss} . Failure to do so can lead to spurious discontinuities in C_D^G as a function of α_g .

2.4 Massé Modification

It should be kept in mind that the Gormont model was developed for helicopter blades, which tend to be thinner, and experience smaller angle-of-attack variations, than typical VAWT blades. In the present analysis it is being applied to thicker airfoils, and much wider excursions in angle-of-attack, than those for which it was intended to be used. This has led to speculation that use of the Gormont model may overestimate dynamic stall effects in VAWT applications. Berg[15] found that a heuristic modification to the model suggested by Massé[17], which reduces its influence at high α 's, further improved the agreement with measured load data. The general form of this modification is:

$$\begin{aligned} C_{L,D}^M &= C_{L,D}^S + \left[\frac{A_M \alpha_{ss} - \alpha_g}{A_M \alpha_{ss} - \alpha_{ss}} \right] (C_{L,D}^G - C_{L,D}^S) & \alpha_g \leq A_M \alpha_{ss} \\ C_{L,D}^M &= C_{L,D}^S & \alpha_g > A_M \alpha_{ss} \end{aligned} \quad (33)$$

where A_M is an empirical constant chosen to give the best agreement with available data. This has the effect of allowing the Gormont model to have its full impact at $\alpha_g = \alpha_{ss}$, *i.e.*, $C_{L,D}^M = C_{L,D}^G$. But its effects are gradually mitigated at larger angles until, at $\alpha_g = A_M \alpha_{ss}$, static characteristics are recovered, $C_{L,D}^M = C_{L,D}^S$. Static characteristics continue to be used for all $\alpha_g > A_M \alpha_{ss}$. Massé[17] used the value $A_M = 1.8$. However, Berg[15] found the best agreement with available 17-m VAWT data was obtained with $A_M = 6.0$. Equations (29) – (33), with $A_M = 6.0$, are used here to obtain the C_L and C_D needed for Eq. (16).

It is recognized that such an *ad hoc* approach to dynamic stall modeling leaves much to be desired. Studies are underway to obtain stall data for conditions more typical of VAWT applications, *e.g.* Ref. [18]. It is hoped these efforts will lead to a more fundamental understanding and improved analytical modeling of the phenomena.

3 STEADY-STATE RESPONSE

The model first predicts the VAWT steady-state performance, *i.e.*, the periodic loads generated by the steady mean wind, for two reasons. First, the steady-state loads provide a convenient benchmark against which to compare the stochastic loads, so as to gauge the effects of turbulence. Secondly, as discussed in Section 4, we will use the interference factors and Reynolds number variations predicted for the steady wind during the stochastic loads calculation, thus realizing a great savings in execution time.

The next section describes how the mean wind is modeled. This is followed by a discussion of how the interference factors and the periodic loads are calculated.

3.1 Mean Wind Shear

By definition, the mean ambient wind is assumed to be steady with respect to both time and direction. It can, however, vary with height above the ground. Several empirical laws have been proposed to describe this variation. Two of the most commonly used are the *logarithmic law*, and the *power law*. The present model allows the user to specify either. The logarithmic variation is given by:

$$\frac{V_{\infty}}{V_{ref}} = \frac{\ln\left(1 + \frac{z}{z_o}\right)}{\ln\left(1 + \frac{z_{ref}}{z_o}\right)} \quad (34)$$

where z_{ref} is the height at which the reference wind speed, V_{ref} , is specified. z_o is the so-called ‘roughness height’, an empirically determined constant. Typical values for z_o range from 10^{-2} to 8×10^{-2} m for relatively flat, open country, to 1 to 10 m for an urban environment. Values for various other types of terrain are given in Table 3.1 of Ref. [19].

The other choice available to the user is the power law variation:

$$\frac{V_{\infty}}{V_{ref}} = \left(\frac{z}{z_{ref}}\right)^n \quad (35)$$

where in this case the local topography is characterized by the exponent, n . Typical values for n are 0.16 for flat, open country, and 0.40 for urban areas. Guidelines for choosing n , and its relationship to z_o in Eq. (34), are discussed in Chapter 3 of Ref. [19]. All the results discussed in this report were generated using the power law variation.

3.2 Iterations for Interference Factors

Together, Eqs. (27) and (28) represent a nonlinear, transcendental equation for the unknown $a_{u,d}$, which must be solved anew in each streamtube using an iteration procedure. *Successive substitution* had worked well for the case with $a_{u,d}$ independent of θ [5]–[6], so it was retained in the generalized analysis. For iteration purposes, all quantities are assumed to be constant over the blade element intersecting the streamtube, with geometric quantities evaluated at the element’s midpoint, (r_m, z_m) in Fig. 2. Within a given streamtube, the mean freestream wind, V_{∞} , is determined by either Eq. (34) or (35) (*cf.* Section 3.1 above). An initial guess is made for a_u (usually 1.0), from which V_u follows by Eq. (19). Equations (17) and (18), with $u = v = 0$, are then used to get W and α_p , and Eqs. (29)–(33) determine C_L and C_D . The latter are used in Eq. (16) for

C_N and C_T , which are needed in the right-hand side of Eq. (28). Finally, Eq. (27) is used to compute a new value of a_u , and the process is repeated to convergence. The iterations for a_d are done subsequent to those for a_u . The procedure is completely analogous, except that now the ‘freestream’ wind is V_e as given by Eq. (10), and the local wind at the actuator is V_d from Eq. (24). A suitable initial guess is $a_d = a_u$.

Dropping the ‘ u,d ’ for the moment, the application of this iteration algorithm to Eq. (27) can be written simply as¹:

$$a_{i+1} = F(a_i) . \quad (36)$$

This method is known to converge provided $|F' \equiv (dF)/(da)| < 1$ in the vicinity of the root we seek (cf. Hildebrand[20], pp. 567 – 569). In the present application it failed to converge whenever the root for a corresponded to a value of α_g very near the value at the previous time step, α_{old} . The reason for the lack of convergence was traced to the Gormont dynamic stall model. Gormont found that switching the empirical constant K_1 (see above) from 1.0 for $|\dot{\alpha}_g| > 0$ to 0.5 when $|\dot{\alpha}_g| < 0$ greatly improved the agreement with experimental data. This results in a discontinuous change in $|F'|$, from a small value when $|\alpha_g| < |\alpha_{old}|$ to a much larger value for $|\alpha_g| > |\alpha_{old}|$. In the latter case, it turned out that $|F'| > 1$, which was the source of the problem.

Accordingly, the method is augmented by another iteration scheme, the so-called *method of false position* (Ref. [20], pp. 572 – 573). If

$$f(a) \equiv a - F(a) , \quad (37)$$

then we seek the root such that $f(a) = 0$. Suppose we already have two iterates, a_i and a_{i-1} , with corresponding values of f given by f_i and f_{i-1} . Then the next iterate is found from:

$$a_{i+1} = a_i - \frac{a_i - a_{i-1}}{f_i - f_{i-1}} f_i . \quad (38)$$

If f_i and f_{i-1} have opposite signs, i.e., if a_i and a_{i-1} straddle the root we seek, this corresponds to inverse linear *interpolation* between the last two iterates to estimate where the intersection of f with the horizontal axis occurs. After f_{i+1} is calculated, whichever of the previous two guesses has an f with the same sign is discarded, and Eq. (38) is applied again. This assures that the root remains bracketed between iterates on opposite sides. Under these circumstances convergence is guaranteed, regardless of the magnitude of $|F'|$. If this method is started with two iterates on the same side of the root, Eq. (38) corresponds to *extrapolation* to the next guess, and convergence cannot be guaranteed.

The code presently starts the iterations using successive substitution, Eq. (36). If, after four iterations, convergence has not been reached, and, $|(F_i - F_{i-1})/(a_i - a_{i-1})| > 0.8$, then the iterations are switched to the method of false position, Eq. (38). This worked even in those few cases where it was necessary to start with iterates on the same side of the root. The convergence criterion used is that the relative error between successive iterates of a be less than 10^{-4} . For the calculations presented in this report, the number of iterations required ranged from a minimum of 2-3 to a maximum of 12. It should be emphasized that this criterion reflects the desired *numerical* accuracy. A low value was chosen to minimize the effects of cumulative numerical errors on the final

¹In this section, i is used as an iteration counter, and should not be confused with the time index used elsewhere in the report.

integrated loads. The *physical* accuracy in the unsteady aerodynamic model is considerably less, primarily due to the empiricism in the Gormont model for dynamic stall (*cf.* Sections 2.3 and 2.4 above), coupled with the use of 2-D steady airfoil characteristics. Once convergence is reached, the $a_{u,d}$ and the final Re are stored as functions of z and θ for subsequent use in the loading calculations.

3.3 Loading Calculation

With the interference factors evaluated, it is straightforward to get the aerodynamic loads at any θ from the C_N and C_T given by Eq. (16). These coefficients are proportional to the loading per unit span. The tangential and normal forces integrated over any blade element are given by:

$$T_{el}(\theta) = \frac{1}{2}\rho \int_{el} W^2 c C_T ds \quad N_{el}(\theta) = \frac{1}{2}\rho \int_{el} W^2 c C_N ds \quad , \quad (39)$$

where the integrals extend over the span of the element. The sign convention is such that $T > 0$ when it pulls the blade into the direction of travel, and $N > 0$ when it is directed in towards the axis of rotation, as shown in Fig. 1. Two other quantities of interest are the radial force component R (the horizontal component of N), and the aerodynamic torque, \mathcal{T} . These are given by:

$$R_{el}(\theta) = \frac{1}{2}\rho \int_{el} W^2 c C_N \cos\delta ds \quad \mathcal{T}_{el}(\theta) = \frac{1}{2}\rho \int_{el} r W^2 c C_T ds \quad . \quad (40)$$

As noted in Section 2.1, within each element the airfoil section and chord remain constant, so the integrands in Eqs. (39) and (40) are smoothly varying. Consider just the tangential force for the moment, and let us refer to the lower and upper nodes bounding the element as points A and B, respectively. Then defining the dimensionless coordinate $\xi = s/l_s$, where l_s is the element's span, we can write:

$$T_{el}(\theta) = \int_A^B \tau(s) ds = l_s \int_0^1 \tau(\xi) d\xi \quad (41)$$

where $\tau(\xi) \equiv \frac{1}{2}\rho W^2 c C_T$ $l_s \approx \sqrt{(r_A - r_B)^2 + (z_A - z_B)^2}$

Two-point Gaussian quadrature (*cf.* Hildebrand[20] pp. 390–392) is used to approximate the integral:

$$T_{el}(\theta) \approx \frac{l_s}{2} \sum_{i=1}^2 \tau(\xi_i) \quad \xi_i = \frac{1 \pm g}{2} \quad g = 0.57735\dots \quad (42)$$

This is the integrated load on the element. The model splits this into two discrete loads at the node points, which are used as inputs to subsequent structural analysis models. To be consistent with that analysis, the loads are distributed using the same shape functions used in formulating the structural finite elements, and the result is:

$$T_A = \frac{l_s}{2} \sum_{i=1}^2 (1 - \xi_i) \tau(\xi_i) \quad T_B = \frac{l_s}{2} \sum_{i=1}^2 \xi_i \tau(\xi_i) \quad . \quad (43)$$

It is easily verified from Eqs. (42) and (43) that $T_{el} = T_A + T_B$, as it should. Note that the total load at the n^{th} node, T_n , consists of contributions from both element $n-1$ (where it plays the role of point

B) and from element n (where it plays the role of point A). The abscissae at which the integrand is evaluated correspond to the *aerodynamic control points* shown in Fig. 2. In physical coordinates, their location is given by

$$r_{ai} = r_n - \xi_i (r_n - r_{n+1}) \quad z_{ai} = z_n + \xi_i (z_{n+1} - z_n) \quad i = 1, 2. \quad (44)$$

The same type of quadrature is used to obtain the other loads defined by Eqs. (39)–(40). The end result of the spatial integrations is the set of nodal loads, $T_n, N_n, R_n, \mathcal{T}_n$, $n = 1, \dots, N_{node}$.

The integrated torque over the entire blade, \mathcal{T}_b , is obtained by summing over all elements on the blade, or equivalently, over all the nodal loads:

$$\mathcal{T}_b(\theta) = \sum_{el=1}^{N_{be}} \mathcal{T}_{el}(\theta) = \sum_{n=1}^{N_{node}} \mathcal{T}_n(\theta) \quad (45)$$

The same procedure is followed to obtain T_b, N_b , and R_b as functions of θ . Since we've assumed (for the purposes of this section) that no turbulence is present, the blade loading is periodic and depends only on θ , irrespective of any absolute time reference. Hence for a rotor with B evenly-spaced blades, the total torque on the turbine, \mathcal{T}_t , is just

$$\mathcal{T}_t(\theta) = \sum_{b=1}^B \mathcal{T}_b[\theta + (b-1)\beta] \quad \beta = \frac{2\pi}{B} \quad (46)$$

This summation presumes that β , the azimuthal spacing between blades, is an integral multiple of $\Delta\theta$. Since $\beta/(\Delta\theta) = (2\pi)/B + (2\pi)/N_\theta = N_\theta/B$, this is the reason for choosing N_θ to be a multiple of B .

The average power out is predicted by

$$P_0 = \overline{\mathcal{T}_t} \Omega = \frac{\Omega}{2\pi} \int_{-\pi/2}^{(3\pi)/2} \mathcal{T}_t(\theta) d\theta \quad (47)$$

The subscript "0" is used to denote that this is the steady-state average power, as distinguished from that with turbulence present. In addition to the total P_0 , the model also tabulates the fraction that each blade element is responsible for, in effect giving the distribution of power with blade span. Finally, the model does a Fourier analysis of the periodic loads and torque to get a picture of their harmonic content. This information is output in the form of a power spectral density (PSD) of N_b, R_b, T_b , and \mathcal{T}_t vs. frequency. Since these loads are periodic, their spectra are discrete—*i.e.*, they contain excitation only at the fundamental frequency and its harmonics.

Presentation of the steady-state load predictions is deferred until Section 5, where they are discussed along with the stochastic predictions. The next section describes how the latter are calculated.

4 STOCHASTIC RESPONSE

The first step in predicting the stochastic response of the turbine is the definition of the ambient wind environment, now assumed turbulent, in which it operates. At each instant, the total wind is assumed to be a linear superposition of a steady, or mean, component $\vec{V}_\infty = (-V_\infty, 0, 0)$, plus a random fluctuation $\hat{v} = (u, v, w)$. Modeling of the mean component has already been discussed in Section 3.1, and the same equations are used here. The next section describes how the present model simulates a random three-dimensional field of turbulence. This is followed by a discussion of how the convection of the turbulence through the turbine is modeled. Then the procedure for integrating this field with the aerodynamic analysis of Section 2 is discussed.

4.1 3-D Turbulence Simulation

The present model only attempts to simulate an ambient field of turbulence being advected through the rotor. Any influence of the rotor on this turbulence pattern is neglected, with one exception that will be noted below. Also neglected is any additional turbulence generated by the turbine itself, *e.g.*, that in the boundary layers and wakes shed by the blades and the tower. Even if the latter two effects could be accurately modeled, a questionable point given the current state-of-the-art, they would require at least an order of magnitude more in computer resources. Moreover, given the approximate nature of the aerodynamic model, it is debatable whether their inclusion would significantly increase the fidelity of the simulations.

Turbulence in the Earth's boundary layer is neither homogeneous nor isotropic, and a general method for simulating inhomogeneous, anisotropic turbulence has yet to be developed. Accordingly, we make the simplifying approximation that the turbulence can be viewed as *locally* homogeneous and isotropic. Departures from homogeneity and isotropy may be handled in an *ad hoc* manner by allowing global parameters such as the turbulence intensity or integral scale to vary with height above ground (*e.g.*, Frost, et al[19], Chapter 4).

Several different approaches have evolved for simulating atmospheric turbulence in wind turbine applications (Refs. [2], [7], [21], [22], and [23]). These were recently compared by Walker, et al[24]. The model by Thresher, et al[21] – [22] assumes the random pattern of turbulence can be expanded in a series, each term of which is a product of spatially and temporally varying functions. Thus far it has only been developed for HAWT geometries, and in order to truncate the series it is assumed that only frequencies less than twice the rotational frequency have an appreciable effect on response. Powell & Connell[23] start by deriving an autocorrelation for the fluctuations sensed by a point rotating with a blade. From this, a power spectral density is obtained, which is then used to generate a time series of the fluctuations sensed by the rotating point. This model has been developed for both HAWT and VAWT geometries, but has the drawback of being able to simulate the time history at only one point on one blade.

The method used here to compute the turbulent velocity components is the same as that employed by Veers[2][7], based on the work of Shinozuka & Jan[25]. In broad terms, this method works in a stationary coordinate frame to generate values of turbulence at discrete points in space and time. Values applicable to the rotating points of interest at appropriate instants are then sampled from the full field. This approach has two advantages: first, the process of generating the turbulence field is completely divorced from the geometric and operating characteristics of the rotor; second, one can sample the field at as many points as one needs. Earlier numerical predictions based on this method (Refs. [2], [5], and [6]) employed a simple 1-D simulation, *i.e.*, the turbulence was assumed to vary only in the streamwise (x) coordinate. However, the method is

readily extendable to a full 3-D variation (Refs. [7] and [25]), which is how it has been implemented in the present model.

A stochastic time series of turbulence values is generated at each of several points arranged in a rectangular planar (y, z) array, located some distance upstream of the rotor. The points are arranged in N_{ver} rows by N_{hor} columns, as shown in Fig. 3 below. The coordinates of the $(i_r, i_c)^{th}$

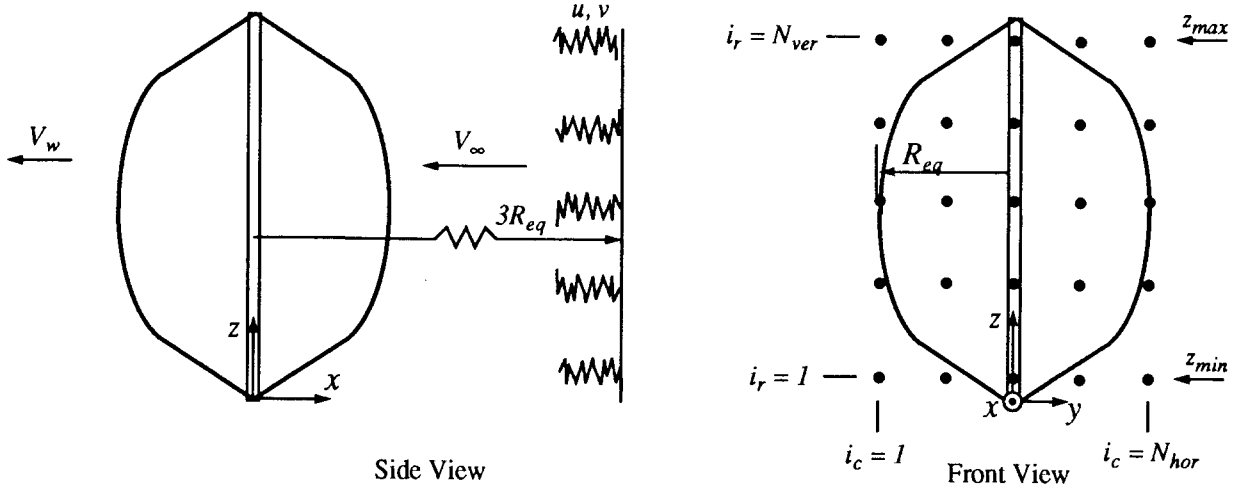


Figure 3. Turbulence Simulation Grid

point are (y_{i_c}, z_{i_r}) as computed from:

$$y_{i_c} = -R_{eq} + (i_c - 1) \Delta y_c \quad \Delta y_c = \frac{2R_{eq}}{N_{hor} - 1} \quad i_c = 1, \dots, N_{hor} \quad (48)$$

$$z_{i_r} = z_{min} + (i_r - 1) \Delta z_r \quad \Delta z_r = \frac{z_{max} - z_{min}}{N_{ver} - 1} \quad i_r = 1, \dots, N_{ver}$$

where z_{max}, z_{min} are the highest and lowest values, respectively, of the z_n discussed in Section 2.1. The model includes both the streamwise, u , and transverse, v , components of the turbulent velocity. The vertical component, w , is neglected on the grounds that it is generally smaller than the other two, and over most of the blade span has little influence on the angle-of-attack.

Turbulence Intensity & Power Spectral Density. It is assumed that the turbulence may be treated as a Gaussian random process, characterized by the root-mean-square turbulence intensity, σ , and the one-sided *power spectral density* (PSD), S_{jj} . Here $j = 1, \dots, N_{pts}$ is a single linear index running over all $N_{pts} = N_{ver} \times N_{hor}$ turbulence generation points in the array. By definition,

$$\begin{aligned} \sigma_u &= (u^2)^{1/2} & \sigma_u^2 &= \int_0^{\infty} S_{jj}^u(f) df \\ \sigma_v &= (v^2)^{1/2} & \sigma_v^2 &= \int_0^{\infty} S_{jj}^v(f) df \end{aligned} \quad (49)$$

where the overbar denotes a time average, and f is the frequency of a particular component in the fluctuations. σ^2 is a measure of the total energy in the signal, and $S_{jj}(f)\Delta f$ can be thought of as the contribution from a bandwidth Δf centered about f .

One can specify the intensities σ_u and σ_v , or use default values supplied by the model. The latter, taken from Chapter 4 of Ref. [19] are given by:

$$\sigma_u = \frac{1.0V_\infty(z = 10 \text{ m})}{\ln\left(\frac{10}{z_o} + 1\right)} \quad \sigma_v = \frac{0.64V_\infty(z = 10 \text{ m})}{\ln\left(\frac{10}{z_o} + 1\right)} \quad , \quad (50)$$

where z_o is the roughness height. The velocity in the numerators is the freestream wind speed at the 10 m level as determined from Eq. (34) or (35). The same intensity is used at all the generation points in Fig. 3; if desired, it is a straightforward extension to allow σ_u and σ_v to vary with height, since the assumed forms for the PSDs (below) already allow such variation.

The PSDs are given in a stationary frame of reference, which is the frame in which such measurements are customarily made. Any of three well known analytical approximations to the PSDs may be used. All of the numerical results presented later employ the analytical expressions suggested by Kaimal[26] for use in the neutrally stable surface layer. These forms were chosen by Frost, *et al*[19], as appropriate for use in wind turbine simulations:

$$S_{jj}^u(f) = \frac{\sigma_u^2 z}{V_\infty(z)} \frac{11.84}{1 + 192 \left[\frac{fz}{V_\infty(z)} \right]^{5/3}} \quad S_{jj}^v(f) = \frac{\sigma_v^2 z}{V_\infty(z)} \frac{6.434}{1 + 70 \left[\frac{fz}{V_\infty(z)} \right]^{5/3}} \quad . \quad (51)$$

It should be noted that the Kaimal spectra implicitly assume that the longitudinal integral scale of the turbulence is linearly proportional to height above ground, z . The numerical coefficients in the numerators of Eq. (51) differ somewhat from those quoted in Refs. [26], [19] and [2]. As noted by Strickland[27], with the original coefficients the integration in Eq. (49) (which can be done analytically for this form) only yielded 0.962 of the variance, σ^2 . This is apparently the result of Kaimal having included only the finite frequency range $0.005 \leq f \leq 10$ Hz in his calculation of the variance (*cf.* p. 290 in Ref. [26]). Accordingly, a factor of $(0.962)^{-1}$ has been applied here, as reflected in Eq. (51). The other options available in the model are the von Kármán or Dryden spectra (see, *e.g.*, Campbell, Ref. [28]).

Coherence & Spectral Density Matrix. We will drop the “ u, v ” sub/superscripts for the time being, with the understanding that the following development applies to each of these components. Although the time series generated at each point of the grid in Fig. 3 is unique, there is some coherence between the fluctuations at different points, as there would be in the actual flow. This is determined by the *cross-spectral density* (CSD), denoted by $S_{jk}(f)$, in the fluctuations at frequency f at points j and k (*cf.* Bendat & Piersol[29], Chapter 1):

$$|S_{jk}(f)| = \gamma_{jk}(f) \sqrt{S_{jj}(f) S_{kk}(f)} \quad . \quad (52)$$

The nondimensional quantity γ_{jk} is termed the *coherence*. It can vary from $\gamma_{jk} = 0$, for statistically independent fluctuations, to $\gamma_{jk} = 1$, for those which are fully coherent. Meteorological data suggest that the coherence decreases with increasing frequency, and increasing spatial separation between the points. Frost[19] suggested an exponentially decaying form, the argument of the exponential

being proportional to the dimensionless parameter $(f\Delta r/V)$. Here we use a generalization suggested by Solari[30][7]:

$$\gamma_{jk} = \exp \left[-C \left(\frac{f\Delta r}{V_m} \right)^\lambda \left(\frac{\Delta r}{z_m} \right)^\mu \right], \quad (53)$$

where $\Delta r = [(\Delta y)^2 + (\Delta z)^2]^{1/2}$, and V_m and z_m represent the average values of the freestream mean wind, and height, respectively, at the two points. The addition of the argument $(\Delta r/z_m)$ allows Eq. (53) to better mimic the falloff in coherence of the lowest frequencies with increasing spatial separation. Values for the coherence decay coefficient, C , and the exponents λ and μ , are chosen empirically; all are assumed positive. Solari actually proposed that C itself be treated as a random variable, along with certain coefficients in the PSDs. The present model neglects any such variations, and treats C as a constant. This expression is used to model the coherence of both the u and v components of the turbulence.

We now have all the information needed to formulate the *spectral density matrix*, \mathbf{S} :

$$\mathbf{S} = \begin{bmatrix} S_{11} & S_{12} & S_{13} & \cdots & \cdots & \cdots & S_{1, N_{pts}} \\ S_{21} & S_{22} & \cdots & \cdots & \cdots & \cdots & \cdots \\ S_{31} & \cdots & \cdots & \cdots & \cdots & \cdots & \cdots \\ \cdots & \cdots & \cdots & \cdots & \cdots & \cdots & \cdots \\ \cdots & \cdots & \cdots & \cdots & \cdots & \cdots & \cdots \\ \cdots & \cdots & \cdots & \cdots & S_{N_{pts}-1, N_{pts}-1} & S_{N_{pts}-1, N_{pts}} \\ S_{N_{pts}, 1} & \cdots & \cdots & \cdots & S_{N_{pts}, N_{pts}-1} & S_{N_{pts}, N_{pts}} \end{bmatrix}. \quad (54)$$

The diagonal elements of this $N_{pts} \times N_{pts}$ matrix are the PSDs defined by Eq. (51), and the off-diagonal elements are the CSDs defined by Eqs. (52)–(53). Note that \mathbf{S} is real, symmetric, and positive definite.¹ Though not written explicitly here, it should be kept in mind that each element of the matrix \mathbf{S} (as well as \mathbf{H} below) is itself a function of frequency, f .

Spectral Influence Matrix & Turbulence Time Series. The key to the simulation is the factoring of \mathbf{S} into an $N_{pts} \times N_{pts}$ *spectral influence matrix*, \mathbf{H} , as follows:

$$\mathbf{S} = \mathbf{H} \mathbf{H}^T, \quad (55)$$

where $()^T$ indicates the transpose operation. This is accomplished by assuming \mathbf{H} to be lower-triangular,

¹In the more general case where the coherence has a phase associated with it, the matrix \mathbf{S} is complex and Hermitian, but the analysis still carries through[25].

$$\mathbf{H} = \begin{bmatrix} H_{11} & 0 & 0 & \dots & \dots & 0 & 0 \\ H_{21} & H_{22} & 0 & \dots & \dots & \dots & 0 \\ H_{31} & \dots & \dots & \dots & \dots & \dots & \dots \\ \dots & \dots & \dots & \dots & \dots & \dots & \dots \\ \dots & \dots & \dots & \dots & \dots & 0 & 0 \\ \dots & \dots & \dots & \dots & \dots & H_{N_{pts}-1, N_{pts}-1} & 0 \\ H_{N_{pts}, 1} & \dots & \dots & \dots & \dots & H_{N_{pts}, N_{pts}-1} & H_{N_{pts}, N_{pts}} \end{bmatrix} \quad (56)$$

Substituting Eq. (56) into (55) leads to the following system of equations for the elements of \mathbf{H} :

$$\begin{aligned} H_{11} &= S_{11}^{1/2} \\ H_{21} &= S_{21}/H_{11} & H_{22} &= (S_{22} - H_{21}^2)^{1/2} \\ H_{31} &= S_{31}/H_{11} & H_{32} &= (S_{32} - H_{31}H_{21})/H_{22} & H_{33} &= (S_{33} - H_{31}^2 - H_{32}^2)^{1/2} \\ & & & \vdots & & \\ & & & \vdots & & \\ H_{jk} &= \left(S_{jk} - \sum_{l=1}^{k-1} H_{jl}H_{kl} \right) / H_{kk} & k &< j \\ H_{jj} &= \left(S_{jj} - \sum_{l=1}^{j-1} H_{jl}^2 \right)^{1/2} & k &= j \\ H_{jk} &= 0 & k &> j \end{aligned} \quad (57)$$

The final step is the evaluation of the turbulence as a Fourier series in time. The series at each point is expressed as a linear superposition of N_{pts} unit-amplitude, white-noise inputs, each of which is independent of the others. The elements of \mathbf{H} represent the weighting factors used in the superposition; specifically, H_{jk} is the amplitude of the k^{th} input signal to be applied to the output signal at the j^{th} point. The random input signals are represented in matrix form by a diagonal matrix, \mathbf{X} , whose elements are given by:

$$\begin{aligned} X_{jj} &= e^{-i\varphi_{kq}} & k &= j \\ X_{jk} &= 0 & k &\neq j \end{aligned} \quad (58)$$

where $i = \sqrt{-1}$. Each of the diagonal elements has unit magnitude, and a random phase, φ_{kq} , which is the phase applied to the q^{th} harmonic in the k^{th} input signal; φ_{kq} is uniformly distributed over the interval 0 to 2π . The column vector of complex Fourier coefficients of the turbulence, \mathcal{V} , is obtained by post-multiplying the matrix \mathbf{H} by \mathbf{X} to obtain an $N_{pts} \times N_{pts}$ matrix, which in turn is post-multiplied by a column vector of 1's, *i.e.*,

$$\mathcal{V} = \mathbf{H} \mathbf{X} \mathbf{1} \quad (59)$$

Each element of the product $\mathbf{H}\mathbf{X}$ represents the complex coefficient multiplying the contribution from the k^{th} input signal to the output at point j ; \mathbf{H} supplies the amplitude, and \mathbf{X} the phase. Multiplying by $\mathbf{1}$ serves to sum over all the columns (input signals), to obtain the total signal at point j . For evaluation purposes, it is best to write out the turbulence time series in summation notation, reintroducing the superscripts “ u , v ” to refer to the specific component. The turbulence values at point j at the m^{th} time instant are given by:

$$\begin{aligned}
 u_{\infty jm} &= \sqrt{2\Delta f_{ts}} \mathcal{R}e \left[\sum_{q=1}^{N_{turb}/2} \sum_{k=1}^j H_{jk}^u(f_q) e^{i(2\pi f_q t_m - \phi_{kq}^u)} \right] & j = 1, \dots, N_{pts} \\
 v_{\infty jm} &= \sqrt{2\Delta f_{ts}} \mathcal{R}e \left[\sum_{q=1}^{N_{turb}/2} \sum_{k=1}^j H_{jk}^v(f_q) e^{i(2\pi f_q t_m - \phi_{kq}^v)} \right] & m = 1, \dots, N_{turb}
 \end{aligned} \tag{60}$$

where $\mathcal{R}e$ indicates that the real part of the complex expression in brackets is to be taken. N_{turb} is the total number of turbulence values, or time instants, in the series. The Central Limit Theorem guarantees that as $N_{turb} \rightarrow \infty$, the above series will converge to a Gaussian signal of zero mean, with the specified σ^2 and S_{jk} [25]. Once the H_{jk} and ϕ_{kq} are known, the entire sequence of values can be computed with one call to a Fast Fourier Transform (FFT) routine.

Equation (60) introduces several new quantities. The subscript “ ∞ ” is used on the left to indicate that these are freestream turbulence values; as will be discussed in Section 4.3, a small modification is made to obtain the local values at the actuator locations. t_m is the m^{th} discrete time value, $t_m = m\Delta t_{ts}$, $m = 1, \dots, N_{turb}$; and Δt_{ts} is the time interval used in the turbulence simulations, which in general is *not* the same as that used to delineate the rotor motion (*cf.* Δt in Eq. (1)). These quantities will be discussed at more length in Sections 4.2 and 4.3. Also, $f_q = q\Delta f_{ts}$ is the q^{th} harmonic frequency in the signal, $q = 1, \dots, N_{turb}/2$. The frequency and time intervals in the turbulence simulation are related (see, *e.g.* Ref. [29]) through $\Delta f_{ts} = (N_{turb}\Delta t_{ts})^{-1}$. Typical values for these parameters, as well as sample turbulence simulations, will be discussed in Section 5 in connection with the numerical results.

Storage Considerations. One drawback to this method of simulating the turbulence field is that the matrices \mathbf{S} and \mathbf{H} require a significant amount of storage. Recall that each of the $N_{pts} \times N_{pts}$ elements is itself a function of frequency, in effect adding a third dimension of size $N_{turb}/2$ (*cf.* Eq. (60) above). In addition, separate \mathbf{S} and \mathbf{H} arrays are required for each turbulence component. Thus, a separate storage location for each element would ordinarily require

$$\underbrace{N_{pts} \times N_{pts}}_{\text{spatial indices}} \times \underbrace{N_{turb}/2}_{\text{frequencies}} \times \underbrace{2}_{\mathbf{S} \text{ and } \mathbf{H}} \times \underbrace{2}_{u \text{ and } v} = 2N_{turb}N_{pts}^2$$

words. For the calculations presented in this report, this represents in excess of 2.5 million words of memory, just for these matrices.

Fortunately, measures can be taken that reduce this number considerably. Recall that \mathbf{S} is symmetric, while \mathbf{H} is lower diagonal. This means that each has only $N_{pts}(N_{pts}+1)/2$ truly independent elements that must be stored. They can be stored more efficiently in a one-dimensional array of this size. Further, once \mathbf{H} is evaluated, there is no need to keep \mathbf{S} . The form of Eq. (57) also shows that the only time that element S_{jk} is needed is when computing H_{jk} . This means the same storage locations can be used for both \mathbf{S} and \mathbf{H} . As a result, the memory required

for these matrices is reduced to only $N_{turb}N_{pts}(N_{pts}+1)/2$ words. This is still a significant amount, and for this reason the method is suitable only on platforms with either large amounts of real memory, or, as is the case for the present calculations, a virtual memory operating system.

When simulating turbulence for use with HAWT geometries, Veers has further streamlined this method, resulting in a decrease in both computing time and storage requirements. For a discussion of this, see Section 6 of Ref. [7].

Specialization to 1-D. A few words are in order regarding the relationship of these more general 3-D results to the earlier 1-D simulation method used in Refs. [2], [5] and [6]. The “1-D” refers not to the number of turbulence components, but rather to the number of coordinates in which they are allowed to vary. Thus, both u and v are still simulated, but they are assumed to vary only with x (or equivalently t), and to be independent of both y and z . This means that not only must σ_u and σ_v be constant in Eq. (51), but z and $V_\infty(z)$ are replaced by their (constant) reference values z_{ref} and V_{ref} , respectively. To achieve perfect coherence in the (y, z) plane, $C \rightarrow 0$ in Eq. (53), and hence $\gamma_{jk} \rightarrow 1$ for all j, k . This results in all the spatial elements of the matrix \mathbf{S} being identical, and equal to the common PSD, $S(f_q)$ say. The \mathbf{H} matrix approaches the limit where all of its elements are zero, except those in the first column, which take on the value $\sqrt{S(f_q)}$. Hence the $k = 1$ term is the only non-zero contribution to the second sum in Eq. (60). The equation reduces to

$$u_{\infty_m} = \sqrt{2\Delta f_{ts}} \mathcal{R}e \sum_{q=1}^{N_{turb}/2} \sqrt{S(f_q)} e^{i(2\pi f_q t_m - \varphi_q)} \quad m = 1, \dots, N_{turb} \quad , \quad (61)$$

where $\varphi_q \equiv \varphi_{1q}$ still varies randomly from 0 to 2π , and the subscript j is now superfluous, since the same turbulence value obtains at all points in the (y, z) plane. This result coincides with Eq. (2) of Refs. [2] and [6], where the coefficients¹ in that result are given by $A_q = \sqrt{2\Delta f_{ts}S(f_q)} \cos \varphi_q$, and $B_q = \sqrt{2\Delta f_{ts}S(f_q)} \sin \varphi_q$. Such a simulation should only be used in cases where the turbine is much smaller than the characteristic scale of the turbulence.

4.2 Turbulence Convection

The preceding section described how time series are calculated to represent the freestream turbulence. Once (u, v) values are generated at the turbulence grid shown in Fig. 3, their convection through the turbine must be modeled. The series so generated represent the random *temporal* variations as sensed by a stationary observer who samples at intervals Δt_s . Equivalently, one can think of an observer convecting with the local mean flow who interprets the series as describing a random *spatial* variation in turbulence, which in his frame of reference is frozen in time. Successive terms then represent the values of (u, v) at intervals $\Delta x = V\Delta t_s$ in the streamwise direction, where V is the local mean windspeed. It is the convection of these data past the stationary observer that produce what to him is a stochastic time variation. This equivalence between temporal (spatial) fluctuations in the stationary (convecting) frames is referred to as Taylor’s hypothesis[31]. Since it neglects the nonlinear interactions between the mean flow and the fluctuations, it is only an approximation, but one which is widely used. It is used here as a straightforward means of correctly sampling the turbulence pattern appropriate to yet a third frame of reference, one rotating with the blade.

¹There is a factor of two difference in the A_q, B_q coefficients quoted in Refs. [2] and [6] only because the FFT routines used in the respective studies normalized the series differently. The final results are equivalent.

The mean windspeed is itself varying with height above ground, owing to the wind shear discussed in Section 3.1. It also varies in the streamwise direction due to retardation by the turbine, which is extracting energy from the air. Unfortunately, the DMST analysis defines this velocity only at locations far up/downstream of the turbine, and at the up/downstream actuators (*cf.* Fig. 1). The continuous variation of V was investigated by Strickland[27] using a vortex model of the turbine. Though by no means exact, he showed that a reasonable approximation was to assume that $V = V_\infty$ up to the point where the streamtube first intersects the blades' path, a linear variation from V_∞ to V_w within the turbine, and a constant value V_w from there on. In the present terms, this means that, for a blade element located at (z, r, θ) the variation of V in the streamtube it intersects is:

$$\begin{aligned} V &= -V_\infty(z) & x &\geq r|\cos\theta| \\ V &= -V_\infty(z) + (x - r|\cos\theta|) \frac{V_w(z, \theta) - V_\infty(z)}{2r|\cos\theta|} & -r|\cos\theta| &\leq x \leq r|\cos\theta| \end{aligned} \quad (62)$$

where V_w follows by combining Eqs. (10), (19), (23), and (24):

$$V_w(z, \theta) = [2a_u(z, \theta) - 1] [2a_d(z, \theta) - 1] V_\infty(z) \quad (63)$$

The absolute value signs are used in Eq. (62) so that it remains valid when the blade is at either the upstream or downstream intersection.

To proceed further, it is necessary to make some arbitrary assumptions about the streamwise location of the plane in which the turbulence is generated, and the instants at which the turbine motion and turbulence simulations are begun. Without loss of generality, we assume that the turbulence generation plane is located at $x = 3R_{eq}$, as depicted in Fig. 3. We can now evaluate the time interval Δt_c required by the turbulence generated at (y_{ic}, z_{ir}) to convect from this plane to the upstream and downstream intersections with its corresponding blade element:

$$\Delta t_c = \int_{3R_{eq}}^{r\cos\theta} \frac{dx}{V} \quad \cos\theta \geq 0 \quad (64)$$

Substitution from Eq. (62) gives

$$\begin{aligned} \Delta t_c &= \frac{3R_{eq} - r\cos\theta}{V_\infty(z)} & \cos\theta &> 0 \quad (\text{upstream}). \\ \Delta t_c &= \frac{3R_{eq} + r\cos\theta}{V_\infty(z)} + \frac{2r\cos\theta}{V_\infty(z) - V_w(z, \theta)} \ln \frac{V_w(z, \theta)}{V_\infty(z)} & \cos\theta &< 0 \quad (\text{downstream}). \end{aligned} \quad (65)$$

The values to be used in Eq. (65) for r, z, θ are the r_m, z_m, θ (*cf.* Figs. 1 and 2) corresponding to the one particular blade element for which z_{ir} lies between z_n and z_{n+1} , and y_{ic} lies between $r_m \sin(\theta \pm (\Delta\theta)/2)$.

Before the rotor motion is initiated, and loading calculations begun, it is necessary to allow sufficient time for enough turbulence to have been generated and convected downstream to fill the turbine. For this reason it is convenient to imagine two clocks. The first measures turbulence simulation time, t_{ts} , which is defined such that $t_{ts} = \Delta t_{ts}$ at the instant when the first terms ($m = 1$ in the turbulence series given by Eq. (60)) are "born" at $x = 3R_{eq}$ and begin to convect downstream. With each succeeding Δt_{ts} , a new turbulence value is born, while its predecessors march

downstream a distance $\Delta x = V\Delta t_{ts}$. The second clock measures turbine time, t , and reads $t = 0$ at the instant when Blade 1 is at $\theta_0 = -\pi/2 - \Delta\theta/2$, and with each succeeding Δt the blades move $\Delta\theta$ in azimuth (*cf.* Eqs. (1)-(2)). The first loading calculations take place for $t = \Delta t$. The relationship between the times measured by these two clocks is,

$$t_{ts} = t + \Delta t_{ts} + (\Delta t_c)_{max} \equiv t + \Delta t_{off} \quad (66)$$

$\Delta t_{off} = \Delta t_{ts} + (\Delta t_c)_{max}$ is the offset required to allow the turbulence time to fill the turbine; $(\Delta t_c)_{max}$ is the maximum time need by turbulence at any of the generation points to convect to the downstream intersection with its corresponding blade element. At first glance, it might appear this would be determined by the generation point closest to z_{eq} , $y = 0$. However, for highly sheared mean winds, this may not be the case. So the second form of Eq. (65), appropriate to the downstream intersection, is evaluated for each of the generation points, and the maximum value is used to determine Δt_{off} . Equation (66) will be needed later in conjunction with the interpolation in the turbulence field.

The interval Δt is defined by Eq. (1), but Δt_{ts} and N_{turb} have yet to be specified. FFT routines are used both to generate the turbulence values from Eq. (60), and to subsequently Fourier analyze the loading predictions. They work most efficiently when the number of points in the time series is large and equal to some power of two, and it is convenient if the number of points in the turbulence series, N_{turb} , is the same as the number of points in the loading time series. If this is so, and the time interval used in both series is the same, $\Delta t_{ts} = \Delta t$, one will run out of turbulence values before the loading simulation is complete, because the turbulence clock must start sooner (Eq. (66)). One could begin repeating turbulence values, *i.e.*, using the u_∞ , v_∞ values from $m = 1, 2, \dots$ for $m = N_{turb} + 1, N_{turb} + 2, \dots$, etc. But this introduces a spurious, albeit low-frequency, periodicity into the turbulence field which may contaminate the predictions.

A better solution is to allow Δt_{ts} to be just enough greater than Δt to allow the loading simulation to finish without running out of turbulence. We set

$$\Delta t_{ts} = c\Delta t \quad (67)$$

where the constant $c > 1$ is to be determined such that the number of terms in the turbulence and loading time series are the same. Let N_{ran} denote the number of points in the time series of random loads. How this number is determined will be discussed in Section 4.3 below, but for the present purpose we can assume it is known. Then it follows that the largest time measured by the turbine clock will be $t_{max} = N_{ran}\Delta t$, at which time the turbulence simulation clock will read (from Eq. (66))

$$(t_{ts})_{max} = N_{ran}\Delta t + \Delta t_{ts} + (\Delta t_c)_{max} \quad (68)$$

But by definition, $(t_{ts})_{max} = N_{turb}\Delta t_{ts}$. If we further require that $N_{turb} = N_{ran}$, and make use of Eq. (67), this becomes

$$(t_{ts})_{max} = cN_{ran}\Delta t \quad (69)$$

By equating (68) and (69), we can solve for c :

$$c = \frac{N_{ran}}{N_{ran} - 1} + \frac{1}{N_{ran} - 1} \frac{(\Delta t_c)_{max}}{\Delta t} \quad (70)$$

N_{ran} is typically a few thousand, so the first term is very close to one, while the second term is much less than one. As a result, usually $1 < c < 1.10$. Having thus specified N_{turb} and Δt_{ts} , the quantity Δf_{ts} in Eq. (60) is now also determined.

4.3 Loading Calculations

Accurate statistical averaging demands that the quantities of interest be averaged over several hundred, even thousands, of turbine revolutions. Storing all the data simultaneously would create prohibitive storage requirements. However, because the turbulence is assumed to be *stationary* in time, *i.e.*, its statistical properties are not changing, the total *ensemble* of all the revolutions in a given run can be broken down into a sequence of much smaller *samples*, each of which is statistically indistinguishable from the others. Then only the data for one sample need be stored at any moment; as each sample is completed, its data are averaged, and then overwritten by that of the following sample. One should not read any deep physical significance into this—a sample is simply a mathematical artifice introduced to avoid having to simultaneously store data for the entire calculation. The number of samples in the ensemble is denoted by N_{sam} . Each sample consists of an integral number of turbine revolutions, N_{rev} , and each revolution is divided into the same number of azimuthal (or time) points, N_{θ} , as is used in evaluating the mean wind response (*cf.* Eqs. (1)–(2)). Thus the total number of time points in each sample, N_{ran} , is equal to $N_{rev} \times N_{\theta}$.

Turbulence Interpolation. As each new sample is begun, both the turbulence and turbine clocks discussed in Section 4.2 are reinitialized, and Eq. (60) is used to generate a unique realization of the turbulence field—unique because the set of random phase angles, ϕ_{kq} , will change from one sample to another. As noted earlier, when $t = 0$ on the turbine clock, Blade 1 is assumed to be at $\theta_0 = -\pi/2 - \Delta\theta/2$, and with each succeeding Δt the blades move counterclockwise through $\Delta\theta$. This uniquely defines the spatial position of each blade element at time t . The loading per unit span is evaluated at the same aerodynamic control points used for the steady-state response (Fig. 2). The first step is the determination of the turbulence at these positions, which involves interpolation in both space and time. A given aerodynamic control point, say at (r_a, z_a, θ) , can be projected onto the (y, z) plane of turbulence grid points to mark out the spatial interpolation cell defined by $z_{ir} \leq z_a < z_{ir+1}$ and $y_{ic} \leq r_a \sin\theta < y_{ic+1}$ as shown in Fig. 4.

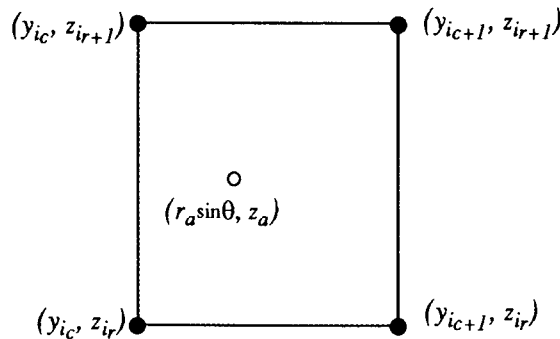


Figure 4. Spatial Interpolation Cell for Turbulence

First we must find the turbulence values appropriate to each corner of the cell. Consider just the corner at (y_{ic}, z_{ir}) for the moment. The turbulence at this point at turbine time t was *generated* at the instant when the turbulence simulation clock read t_g , as given by

$$t_g = t_{ts} - \Delta t_c \quad (71)$$

where t_{ts} is given by Eq. (66), and Δt_c is the convection time obtained from the appropriate form of Eq. (65), depending on whether the element is at its up- or downstream intersection with the current streamtube. In general, t_g will not coincide with any of the t_m values for which turbulence was generated with Eq. (60). Therefore, the value at time t_g is found by linearly interpolating over the interval defined by $t_m \leq t_g < t_{m+1}$. (The precautions taken in Section 4.2 guarantee that t_g will never lie outside the range bracketed by $m = 1$ and $m = N_{turb}$.) The same procedure is followed at each of the other three corners of the cell. It should be emphasized that, while t and t_{ts} are the same for all points, Δt_c and hence t_g will vary because the turbulence generated at different points convects at different speeds. Having thus obtained turbulence values at all four corners of the cell at time t in Fig. 4, the values appropriate to the aerodynamic control point are found using bilinear interpolation with respect to y and z .

Correction for Turbine Interference. The values so obtained represent “freestream” turbulence. In a blade’s rotating reference frame, both the mean and turbulent wind components appear unsteady, and it has no way of differentiating between the two. Therefore, in computing the instantaneous relative velocity, it is assumed that the turbine acts to reduce the streamwise turbulence by the same interference factor, a_u on the upwind side, by which the mean velocity is reduced, *i.e.*, $u = a_u u_\infty$. This is the only manner in which the turbine is allowed to influence the structure of the incoming turbulence. Since the DMST model does not include a transverse momentum balance, the corresponding component is assumed to remain unchanged, *i.e.*, $v = v_\infty$. Analogous considerations apply on the downwind side. These are the values for u and v that are used to evaluate W and α_g from Eqs. (17) and (18).

Instantaneous Loads. The aerodynamic analysis described in Sections 2.2–2.4 is again used to determine the blade loadings. To be most precise, a new iteration should be performed for a_u and a_d at each time step; this was the procedure adopted by Veers[2]. However, this greatly increases run time in a stochastic calculation requiring several thousand time points. Instead, the present model makes the reasonable assumption that, *on the average*, these quantities will not deviate significantly from the values already computed based on the mean windspeed, *cf.* Section 3.2. Hence Eqs. (17) and (18) are employed to compute the instantaneous W and α_g sensed by the blade using the mean a_u and a_d .

Technically, the instantaneous Re should also be used in the interpolation for C_L and C_D . But note that while turbulence can cause large fluctuations in α_g , its influence on Re is less pronounced. A considerable time savings results if the Re based solely on the mean wind, computed and stored previously for each blade element as a function of θ , is used. This effectively reduces the number of dimensions in which one must interpolate from two down to one. The remaining interpolation, with respect to angle-of-attack, is always done using the instantaneous α_g as computed from Eq. (18) with u and v included. The errors introduced by these time-saving artifices will tend to cancel one another out in the statistical averages, and in any event are no worse than the uncertainties in the semi-empirical aerodynamic model. Calculations were done earlier, using the simpler 1-D turbulence model, using both the instantaneous and mean wind Re [5]. Use of the instantaneous Re increased the run time by approximately 25% with no perceptible difference in the ensemble-averaged loading distributions, thus justifying the use of the mean wind Re .

Once W , α_g , and Re are computed as described above, the same analysis and subroutines are used to compute the sectional aerodynamic coefficients (Sections 2.2–2.4), and the same Gaussian procedure is used to integrate along the blade span and distribute the loading between the nodes (Section 3.3), as were used for the steady-state response. This is done to assure that, when comparing steady-state and stochastic loads, any differences are solely the result of having

introduced turbulence, and not a computational artifact. For the purpose of providing inputs to simulation models of blade fatigue, it is the instantaneous aerodynamic loads that are of most interest. Thus, after each sample is complete, the instantaneous time histories of the forces at each node on all B blades are output to a special file for subsequent use. These forces are decomposed into three components in a Cartesian coordinate system rotating with the reference blade, Blade 1, as shown in Fig. 5.

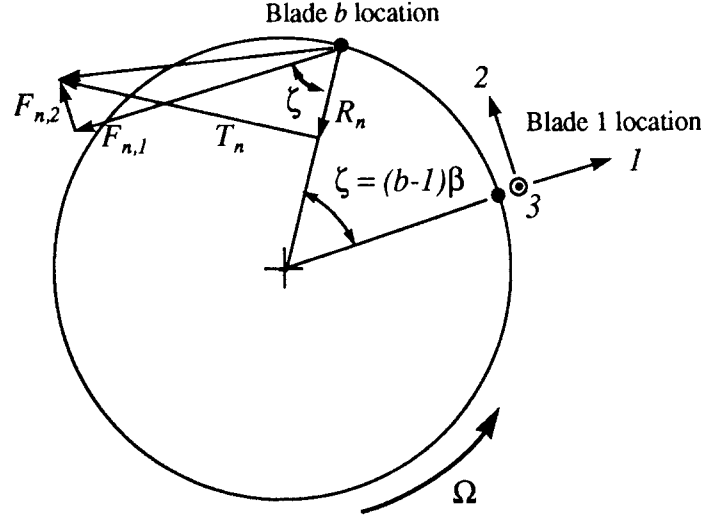


Figure 5. Transformation of Nodal Loads to Frame Rotating with Blade 1

Coordinate 1 is oriented radially outward from Blade 1; coordinate 2 is tangential to Blade 1's path and in the direction of rotation; and coordinate 3 coincides with the z axis. If the blades are numbered counterclockwise, the azimuthal spacing between the b^{th} blade and the reference blade is $\zeta = (b-1)\beta$, as shown in the figure. In terms of R_n and T_n , the instantaneous radial and tangential loads at node n of the b^{th} blade, the desired components $F_{n,1}$, $F_{n,2}$, and $F_{n,3}$ are given by:

$$\begin{aligned} F_{n,1} &= -R_n \cos(b-1)\beta - T_n \sin(b-1)\beta \\ F_{n,2} &= -R_n \sin(b-1)\beta + T_n \cos(b-1)\beta \\ F_{n,3} &= -R_n \tan\delta \end{aligned} \quad (72)$$

At the end of each sample, the model can also output the instantaneous integrated blade loads, N_b , R_b , T_b , and \mathcal{T}_b , for $b = 1, \dots, B$, and the total turbine torque, \mathcal{T}_t , versus time (or θ). Note that, whereas the steady-state loads repeated identically with every revolution, the stochastic loads do not. For example, $\mathcal{T}_b(\theta; i_{rev})$ is now used to denote the instantaneous, integrated torque on the b^{th} blade at position θ during the $(i_{rev})^{\text{th}}$ revolution in the sample, $i_{rev} = 1, \dots, N_{rev}$, as computed from Eq. (45). Similarly, Eq. (46) for the instantaneous torque on the whole turbine is generalized to

$$\mathcal{T}_t(\theta; i_{rev}) = \sum_{b=1}^B \mathcal{T}_b[\theta + (b-1)\beta; i_{rev}] \quad \beta = \frac{2\pi}{B} \quad (73)$$

Statistically Averaged Loads. When comparing load predictions with experimental data, it is necessary to average both over a large population in order to obtain results that are statistically reproducible. Accordingly, after each sample is completed, the *sample-averaged* loading vs. θ , denoted by $\langle \rangle_S$, is calculated. Using \mathcal{T}_t as an example, this is given by:

$$\langle \mathcal{T}_t(\theta) \rangle_S = \frac{1}{N_{rev}} \sum_{i_{rev}=1}^{N_{rev}} \mathcal{T}_t(\theta; i_{rev}) \quad . \quad (74)$$

The calculation of the sample-averaged distributions is an intermediate step towards obtaining the *ensemble-averaged* distributions, written as $\langle \rangle_E$. Upon completion of the $(i_{sam})^{\text{th}}$ sample, $i_{sam} = 1, \dots, N_{sam}$, the latter are updated according to:

$$\langle \mathcal{T}_t(\theta) \rangle_E = \frac{\langle \mathcal{T}_t(\theta) \rangle_S + (i_{sam} - 1) \langle \mathcal{T}_t(\theta) \rangle_E^{old}}{i_{sam}} \quad , \quad (75)$$

where it is understood that the ensemble-average on the right side represents that after $(i_{sam}-1)$ samples. Since $\langle \rangle_S$ is averaged over a population of only N_{rev} data points, while $\langle \rangle_E$ is averaged over $N_{sam} \times N_{rev}$, the ensemble-average is more statistically significant; as noted earlier, sample-averaged quantities are introduced solely to reduce storage requirements. The same procedure is followed to obtain sample- and ensemble-averaged distributions for the other load components as well. The model can output ensemble-averaged variations for $N_b, R_b, T_b, \mathcal{T}_b$, and \mathcal{T}_t , as functions of θ . As discussed later in Section 5, changes in $\langle \mathcal{T}_t(\theta) \rangle_E$ from one sample to the next are also monitored to gauge the convergence of the calculations.

The time histories of the loads within each sample contain $N_{ran} = N_{rev} \times N_\theta$ points. With one call to an FFT routine, the sample-averaged amplitude spectrum of any load may be found. From this, the sample-averaged loading PSD is easily computed. This in turn is used to update the ensemble-averaged PSDs via the same rule used in Eq. (75); at the end of the calculation, these are output for N_b, R_b, T_b , and \mathcal{T}_t . The zero-frequency (DC) component of the PSD represents the square of the time-averaged load over the whole ensemble. Thus, in the case of the turbine torque, multiplication of this predicted \mathcal{T}_t by Ω yields the average power out including the effects of turbulence, denoted by $\langle P \rangle$.

5 RESULTS AND DISCUSSION

Simultaneous measurements of the mean wind, turbulence, and local aerodynamic loads are needed to validate the model in a quantitative sense. Turbulence measurements performed on the DOE/USDA 34-m VAWT Test Bed erected at Bushland, Texas have been reported by Connell & Morris[32]. These measurements were designed for comparison with the Pacific Northwest Laboratory (PNL) theory of single-point rotationally-sampled turbulence[23]. Specifically, the turbulence was measured at six fixed anemometers arranged in a circle at the equatorial height, but 3 m outward from the path of rotation. Their proximity to the blades prevents using this data as input to the present simulation, which requires “freestream” values. Another problem is that the only available aerodynamic data were for the turbine torque, T_t , which is the sum of the spatially-integrated loads on both blades. A model could exhibit reasonable agreement with such data and still be significantly in error where the local loads are concerned. Conversely, discrepancies between the theory and data would provide no clue as to which portion(s) of the blades, or even which blade, were most responsible. Thus there remains a need for simultaneous data on both freestream turbulence and local loads for use in validating practical stochastic models.

In the meantime, the present model has been applied to the 34-m Test Bed for the purpose of illustrating the influence of two important parameters: the reference tip-speed ratio, $\chi = \Omega R_{eq}/V_{ref}$, and the relative turbulence intensity, σ/V_{ref} . The 34-m VAWT Test Bed is shown below in Fig. 6.

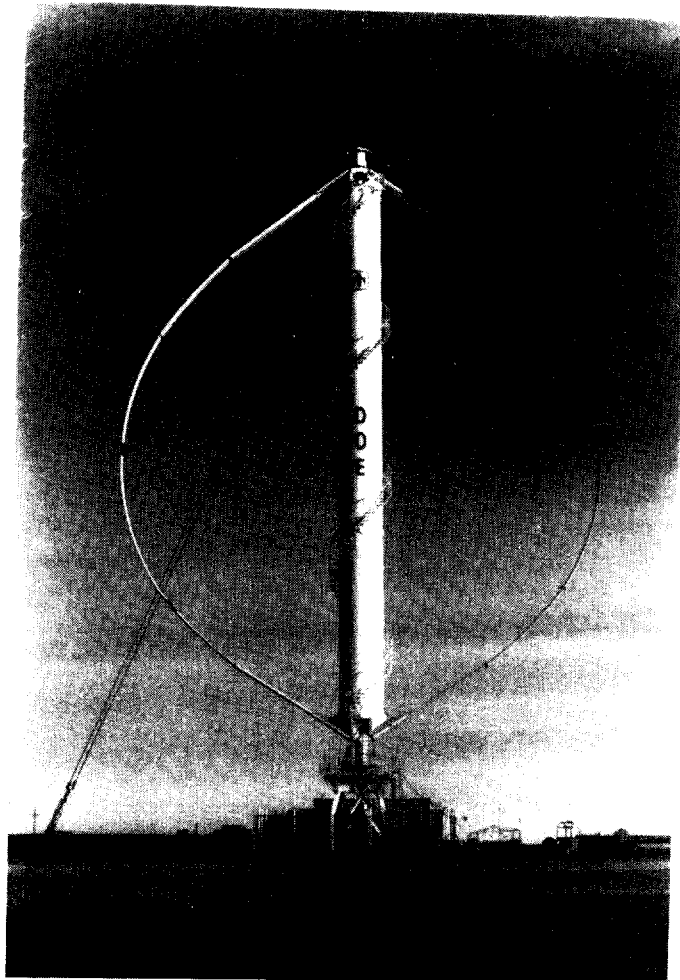


Figure 6. DOE/USDA 34-m VAWT Test Bed

It is a two-blade design with a maximum diameter of 33.5 m (110 ft), rated at 500 kw. Two different airfoil sections are employed on each blade, a NACA 0021 for inboard sections, and a Sandia 0018/50 near the equator. The latter was designed specifically to have favorable natural laminar flow characteristics, with VAWT applications in mind[33]. Chord lengths of 1.22 m, 1.07 m, and 0.91 m (4 ft, 3.5 ft, 3 ft) are used progressing outwards from the tower to the equator. The transitions between these sections are idealized as stepwise discontinuities in the model. A more detailed discussion of the design can be found in Refs. [34] and [35].

The blade geometry was defined by a total of $N_{node} = 39$ node points, for which the (r_n, z_n) coordinate pairs were read from a NASTRAN file; these in turn defined the $N_{be} = 38$ blade elements for which aerodynamic predictions were made. All of the calculations presented here are for a constant rotor rpm of 37.5 (3.93 rad/sec). Each revolution was resolved into $N_\theta = 36$ increments, corresponding to $\Delta\theta = 10$ deg, $\Delta t = 0.044$ sec.

Inputs to the model characterizing the wind were estimated as follows. The mean wind shear is represented by the power law in Eq. (35) with $n = 0.17$. The reference height at which wind speed is specified is $z_{ref} = 28.8$ m (94.5 ft), which is just above the equator. For the turbulence PSDs we use the Kaimal spectra[19][26]. This form implicitly assumes a streamwise integral scale which grows linearly with z ; the coefficients in Eq. (51) give a value of 80.5 m (264 ft) at the equatorial plane. Typically, σ_v is only 80% or so of σ_u [19], so the model allows for independent specification of these two quantities. However, as stated earlier we are not comparing these predictions with any particular data set, but rather wish to study the influence of overall turbulence intensity. Thus, for simplicity it was assumed that $\sigma_v = \sigma_u$. The parameters used to describe the coherence in Eq. (53) were given the nominal values used by Solari[30]: $C = 12.0$, $\lambda = 1.0$, and $\mu = 0.25$. The turbulence grid depicted in Fig. 3 consisted of $N_{ver} = 5$ rows by $N_{hor} = 5$ columns. $N_{turb} = 2016$ turbulence values were computed from Eq. (60) for each sample.

Each calculation consisted of $N_{sam} = 50$ samples, with $N_{rev} = 56$ revolutions per sample. Hence ensemble-averaged quantities presented below represent averages over a total of 2800 revolutions, representing approximately 75 min of operation. This is sufficient to assure that further increases in the number of samples would change the ensemble-averaged load distributions by no more than 1%, as will be illustrated below. Each sample contains $N_{ran} = N_{rev} \times N_\theta = 2016$ load vs. time points.

To bracket the influence of mean wind speed and turbulence intensity, results are presented for a matrix of four cases. These consist of both low and high values of the mean wind, 8.9 m/sec (20 mph) and 20.1 m/sec (45 mph), and, at each speed, two turbulence intensities, 10% and 30%.

5.1 Case 1: 20.1 m/sec (45 mph), 10% Turbulence

The first case is for a wind speed, V_{ref} , of 20.1 m/sec (66 fps or 45 mph), producing a reference tip-speed ratio $\chi = 3.27$; a relative turbulence intensity of 10% is assumed. Before discussing the loads themselves, it is instructive to consider some of the intermediate quantities that precede them. Figure 7 displays the azimuthal variation of the interference factors, $a_{u,d}$. The open symbols connected by solid lines represent the variations at Blade Elements 6, 20, and 34, located approximately 1/4, 1/2, and 3/4 of the way up the turbine. Recall that these are assumed to depend only on the mean wind, and hence the same $a_{u,d}$ apply to Case 2 (below) as well. Also shown in this figure are earlier estimates, based on the simplified analysis of Ref. [6], in which the $a_{u,d}$ were assumed to be functions only of z . These are indicated by the solid symbols connected by horizontal dashed lines. The line extending from $-90^\circ \leq \theta \leq 90^\circ$ is the constant a_u value, and that from $90^\circ \leq \theta \leq 270^\circ$ is the constant a_d value. As one might expect, these earlier values represent some weighted average of the newer azimuthally-dependent predictions.

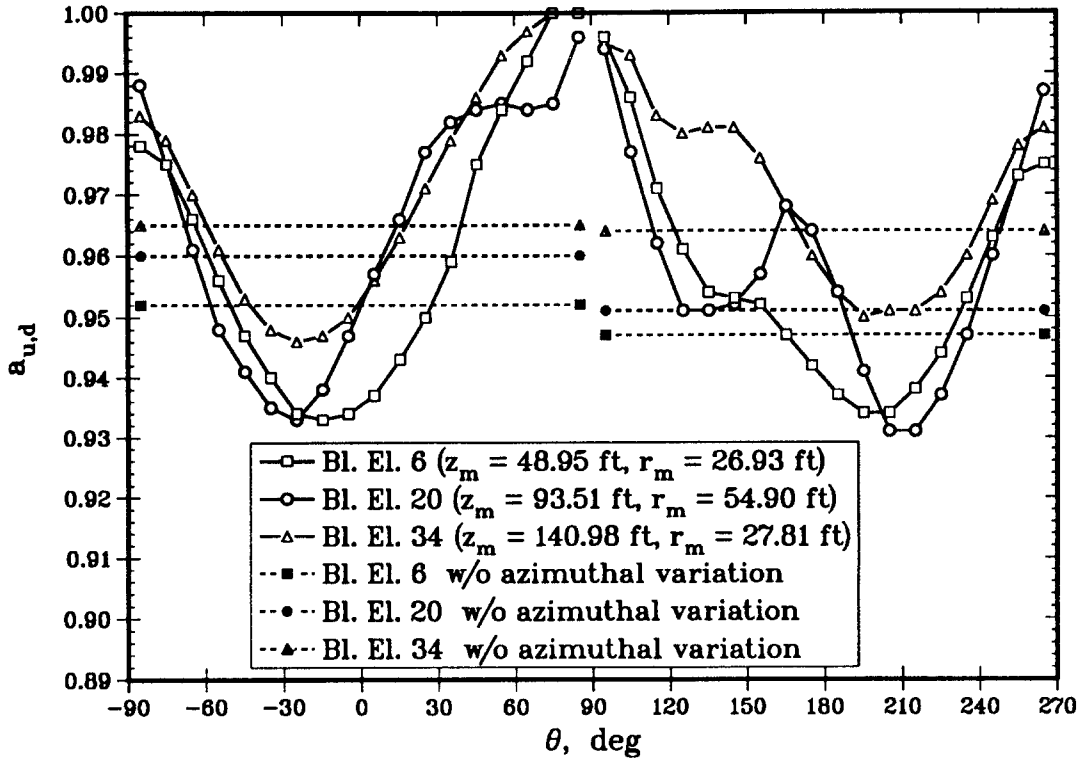


Figure 7. Aerodynamic Interference Factors for Cases 1 and 2

Note that for Blade Element 20 (near the equator) there is a pronounced rise in the curve in the vicinity $120^\circ \leq \theta \leq 200^\circ$. Examination of the numerical output indicates that $-16^\circ \leq \alpha_g \leq -11^\circ$, which is well outside the static stall margin of the SAND 0018/50 airfoil. The blade element's lift/drag ratio, L/D , falls as low as 3-4; in contrast, $L/D \sim 60-70$ in unstalled regions. As a result, the tangential force pulling the blade along is greatly reduced, and for $165^\circ \leq \theta \leq 185^\circ$ actually becomes negative. The flow in this region is much less retarded, as reflected by the increased interference factor. Such behavior remains to be corroborated by experimental data; but the dramatic drop in L/D is at least in qualitative agreement with the flow visualization studies of Reda[36], who reports that the angle-of-attack range noted above is characterized by massive, unsteady, leading edge separation.

Some of the turbulence values that were generated for the stochastic analysis in this case are illustrated in Fig. 8(a-c). The time span shown in this figure is a little more than half the total record length for one sample; the interval between discrete values is $\Delta t_s = 0.047$ sec. The instantaneous values of freestream turbulence as predicted by Eq. (60) are plotted, normalized by their rms value, $\sigma_u = 2.0$ m/sec (6.60 fps). Fluctuations at three different points of the turbulence grid are shown, corresponding to $i_r = 3, i_c = 3, 4,$ and 5 in Fig 3. These values are also representative of those for Case 2, as both cases have the same mean wind, and the effect of the different σ_u is removed by the normalization. One can see that there is a greater degree of correlation between grid points in the low frequency fluctuations than there is in the high frequencies. Also, the degree of correlation decreases with the separation between points. Figure 9 displays the turbulent fluctuations as sensed by a blade in the rotating frame. These are the normalized values experienced by an aerodynamic control point very near the equator, at $z_{al} = 28.0$ m (91.96 ft), $r_{al} = 16.8$ m (54.98 ft) on Blade Element 20.

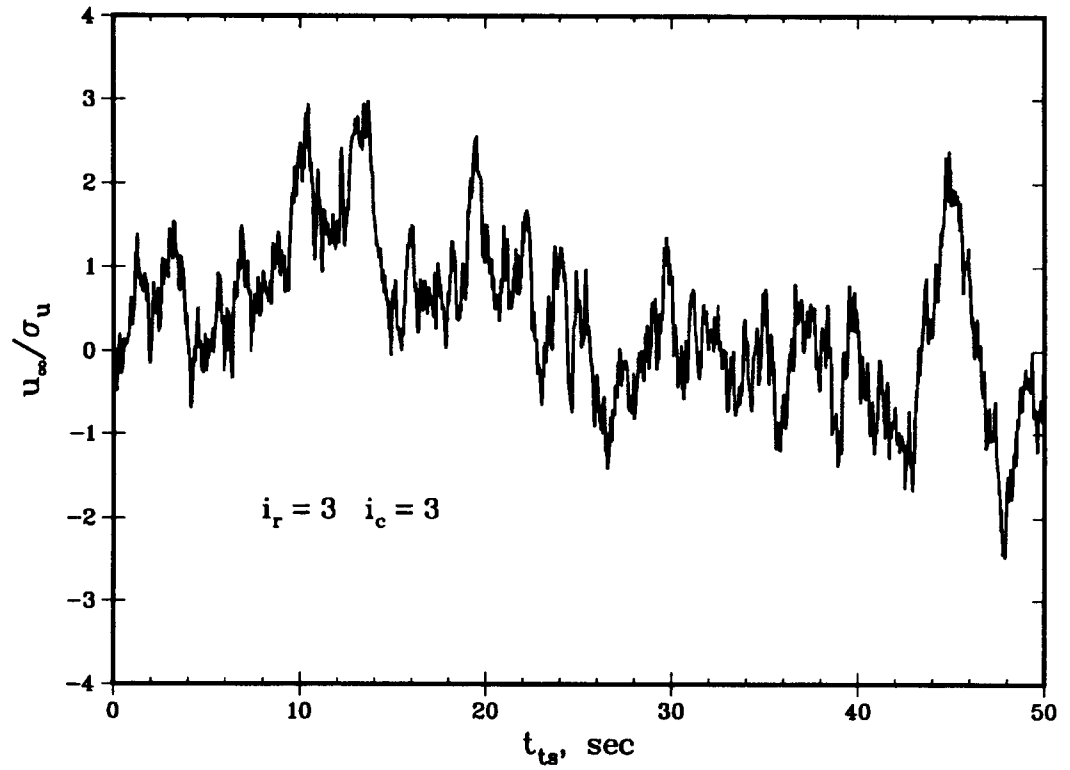


Figure 8a. Streamwise Turbulence at $i_r = 3, i_c = 3$ in Stationary Frame for Case 1

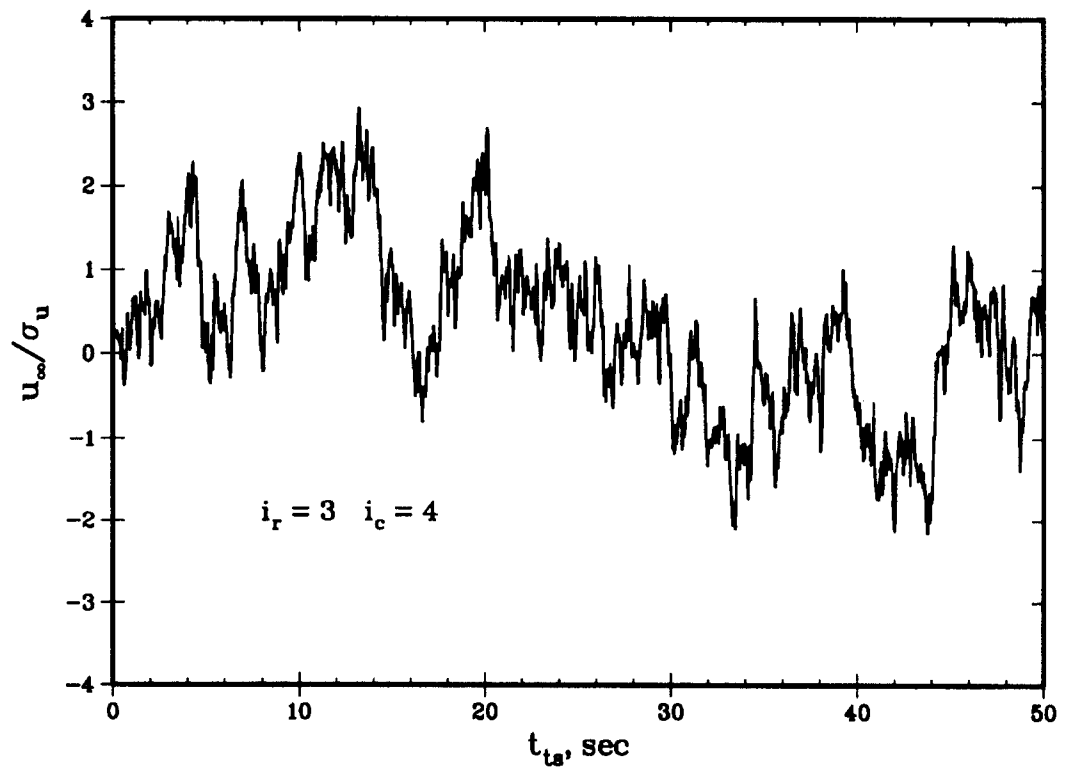


Figure 8b. Streamwise Turbulence at $i_r = 3, i_c = 4$ in Stationary Frame for Case 1

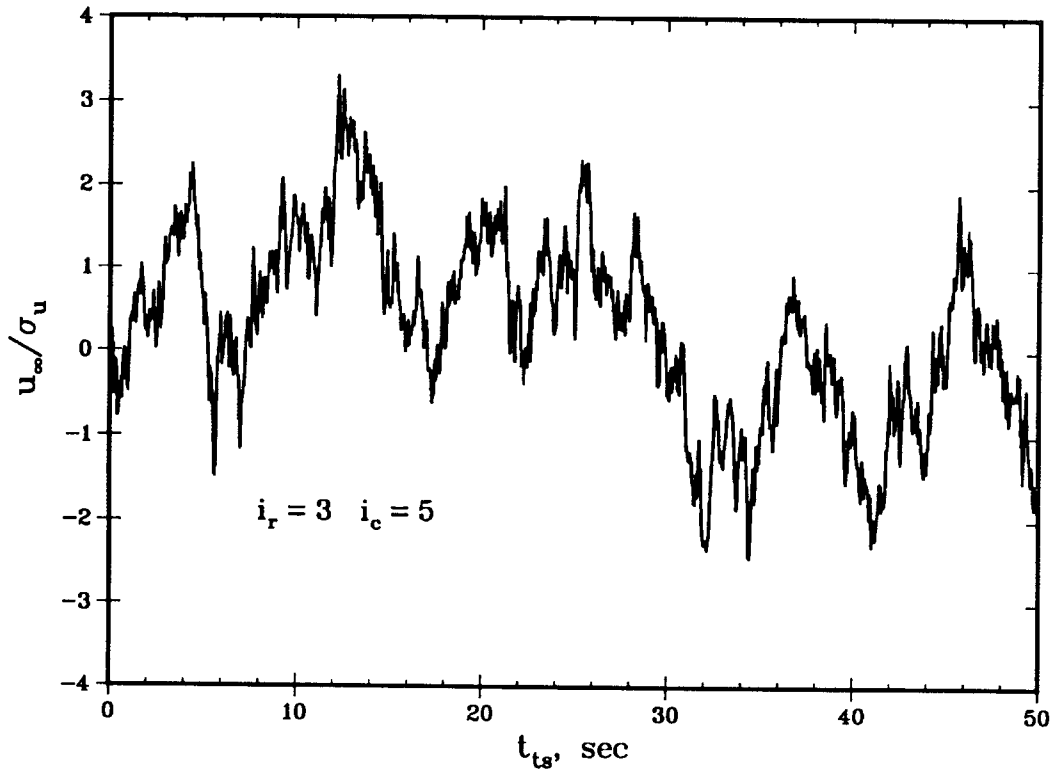


Figure 8c. Streamwise Turbulence at $i_r = 3, i_c = 5$ in Stationary Frame for Case 1

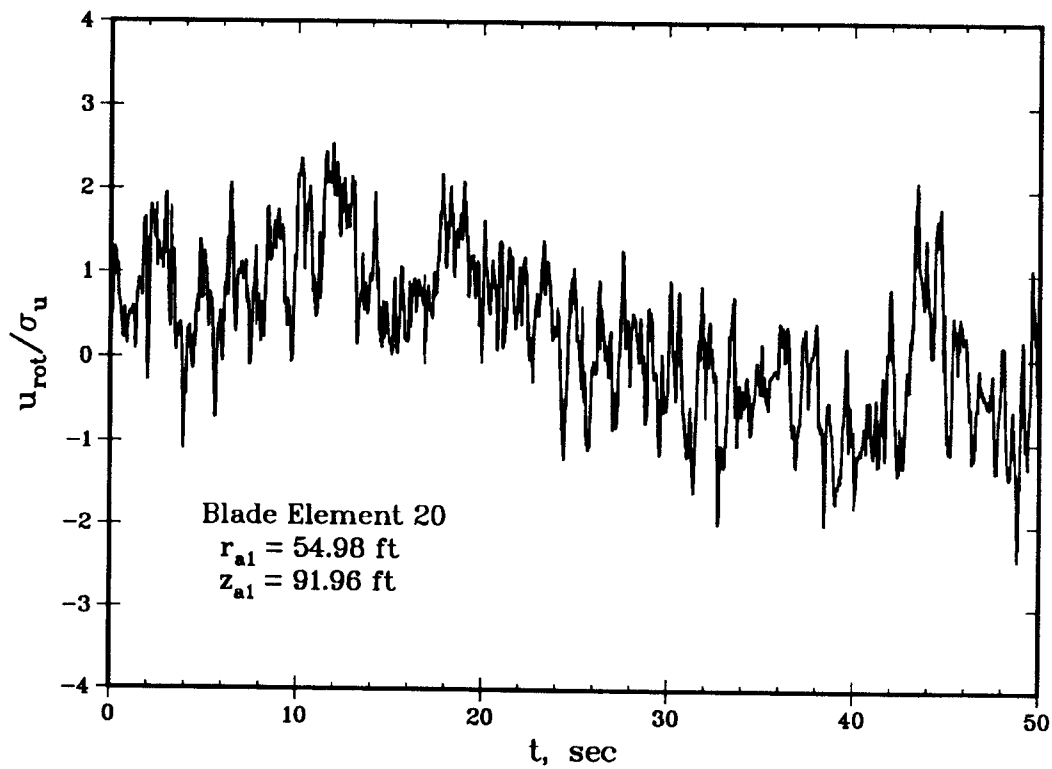


Figure 9. Streamwise Turbulence in Rotating Frame for Case 1

The geometric angle-of-attack variations sensed at this same point are shown in Fig. 10. The solid curve is the variation produced by the mean wind alone, without turbulence; this would repeat identically with each revolution. It behaves more or less sinusoidally, but note that the minimum in the curve on the downwind side, $\alpha_g \sim -15^\circ$, is slightly less than the maximum on the upwind side, $\alpha_g \sim 17^\circ$. This is primarily the result of the wind energy extracted on the upwind pass resulting in $V_d < V_u$. The open symbols are the instantaneous random variations, for each of five distinct revolutions, produced when the turbulence displayed in Fig. 9 is introduced. As one would expect, the stochastic values tend to cluster fairly close to the steady-state distribution at this low turbulence intensity.

Figure 11 compares the steady-state vs. stochastic response of the turbine, as typified by the variation of the integrated rotor torque, \mathcal{T}_i , with θ . Here θ is the azimuthal position of the turbine, which by definition coincides with that of the reference blade (Blade 1). The solid curve is the periodic variation generated when only the mean wind is considered. This variation is cyclic, in that it is repeated identically with each revolution. Note that there are two identical peaks in each revolution, *i.e.*, the fundamental frequency is not Ω but rather 2Ω , owing to the fact that the rotor torque is the sum of the torques on two identical, evenly-spaced blades. This is often referred to as a “two per-rev” variation. Put another way, there is no way to physically differentiate between the situation that exists when the rotor is at θ , from that when it is at $\theta + 180^\circ$. In general, for a rotor with B blades, the rotor torque will exhibit B peaks during one revolution, corresponding to a fundamental frequency of $B\Omega$.

The predicted steady-state output power is the average torque, as determined by the solid line, multiplied by Ω . For this case, as well as Case 2 below, this turns out to be $P_0 = 540$ kw. The performance coefficient, defined as

$$C_p = \frac{P}{(1/2)\rho V_{eq}^3 A}, \quad (76)$$

is the ratio of the aerodynamic power transmitted to the shaft normalized by the rate at which the wind’s kinetic energy is being convected through the turbine¹. For Cases 1 and 2, this is only 0.12; the turbine is producing a large amount of power in an absolute sense, but relatively speaking, only a small fraction of the available wind energy is being harnessed. This is because χ is low enough that the blades are stalled much of the time (*cf.* Eq. (18) and Fig. 10). This stalling also manifested itself in Fig. 7, where it was seen that all the $a_{u,d}$ were in excess of 0.93.

The dashed curve in Fig. 11 represents the ensemble-averaged variation with turbulence present, as determined from Eq. (75). If the aerodynamic response were perfectly linear, the two curves would coincide. Though they are very similar at this low turbulence level, one can see that the turbulence slightly lowers the peaks in the distribution, while raising the dips, or valleys. The area under the dashed curve, which is proportional to the average power in the presence of turbulence, is slightly less than for the solid curve. These differences are the result of aerodynamic nonlinearities associated with stall. It is encouraging to note that the “two per-rev” variation is maintained by the ensemble-averaged results, thus confirming that the two blades are statistically indistinguishable. At this point one might wonder how many samples, in this case each

¹The use of V_{eq} in Eq. (76) is somewhat arbitrary; V_{ref} could have been used instead. In the present case, this would have little effect on the numerical values, as the equatorial and reference heights are quite close. The important thing is that, having made the choice, one stick with it consistently.

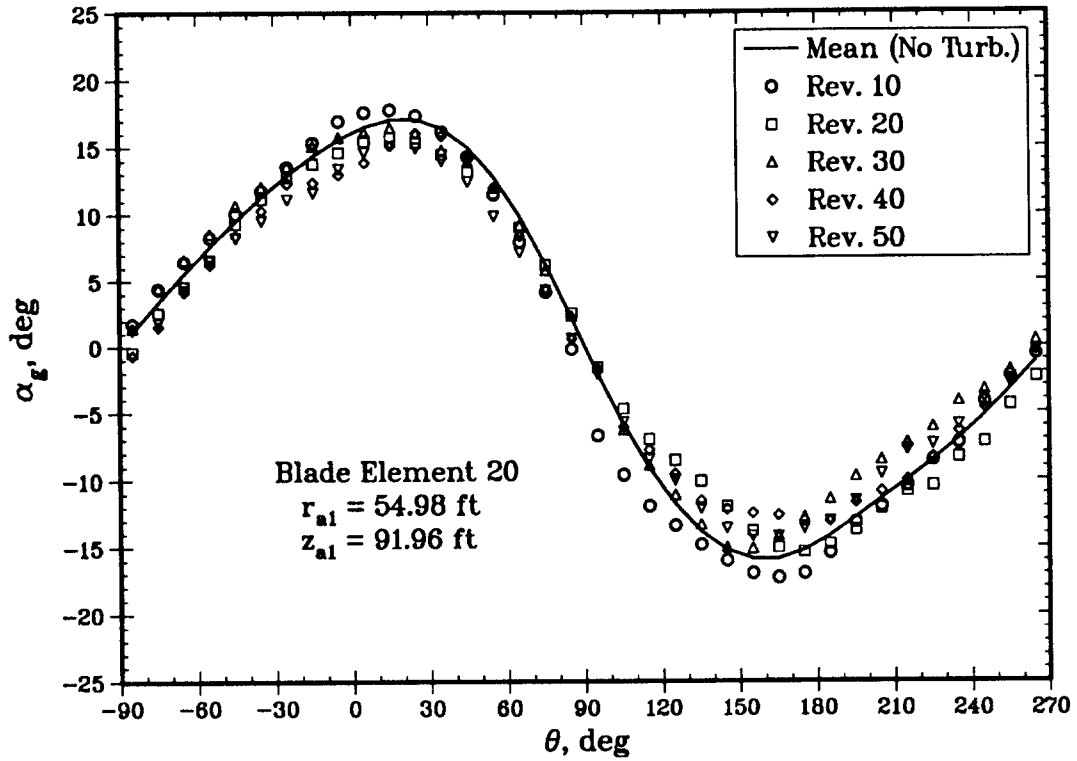


Figure 10. Variations in Angle-of-Attack for Case 1

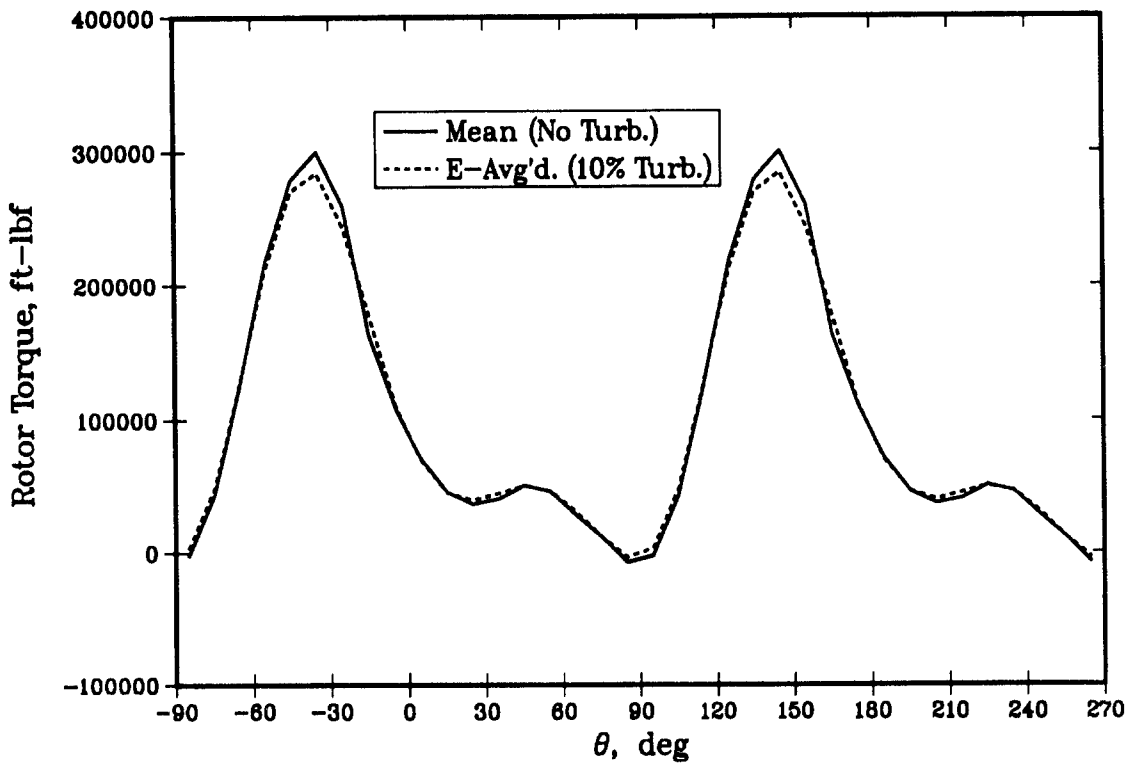


Figure 11. Mean and Ensemble-Averaged Rotor Torque vs. θ for Case 1

representing 56 revolutions, must be simulated before the ensemble-averaged curve stops changing. To study this convergence, we define a maximum relative error as,

$$E_{max} = \left\{ \frac{\langle \mathcal{T}_i(\theta) \rangle_E - \langle \mathcal{T}_i(\theta) \rangle_E^{old}}{\langle \mathcal{T}_i(\theta) \rangle_E} \right\}_{\max \text{ over all } \theta}$$

The denominator is the running estimate of the ensemble-average after the current number of samples, i_{sam} ; the second term in the numerator is that after $i_{sam}-1$. Figure 12 displays the decay of

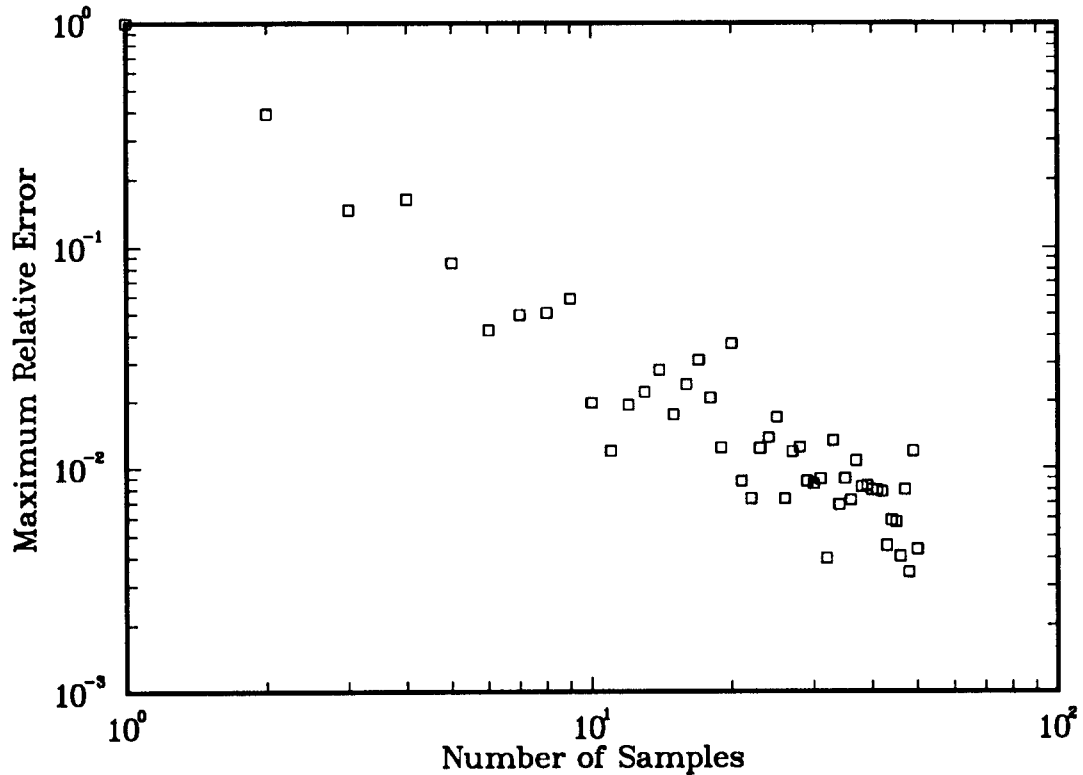


Figure 12. Maximum Relative Error vs. Number of Samples for Case 1

this error vs. the number of samples. As can be seen from the figure, after only 30 to 40 samples, this measure of convergence has fallen below 10^{-2} , which is probably sufficiently accurate for most engineering calculations. In retrospect, this may even be too stringent a measure of convergence. As can be seen from Fig. 11, $\mathcal{T}_i(\theta)$ passes through zero, and in the later stages of the calculation, it is this region of θ that invariably determines E_{max} , even though in the limit $\mathcal{T}_i \rightarrow 0$ the above definition is indeterminate.

The ensemble-averaged rotor torque is useful primarily for making comparisons with experimental data, and studying changes in average output power. It can be misleading in regard to blade fatigue effects. At first glance, one might conclude from Fig. 11 that turbulence is beneficial to fatigue life, in that it appears to lower the peaks in the distribution, while raising the valleys. This certainly would run counter to our intuition. However, the dashed curve only represents the average of several thousand instantaneous distributions, and is not truly representative of any one of them. It is the instantaneous fluctuations that matter most from a fatigue standpoint, and Fig. 13 shows these for five different revolutions chosen arbitrarily from the first sample (the same ones shown in Fig. 10). As one would expect, they show larger amplitude

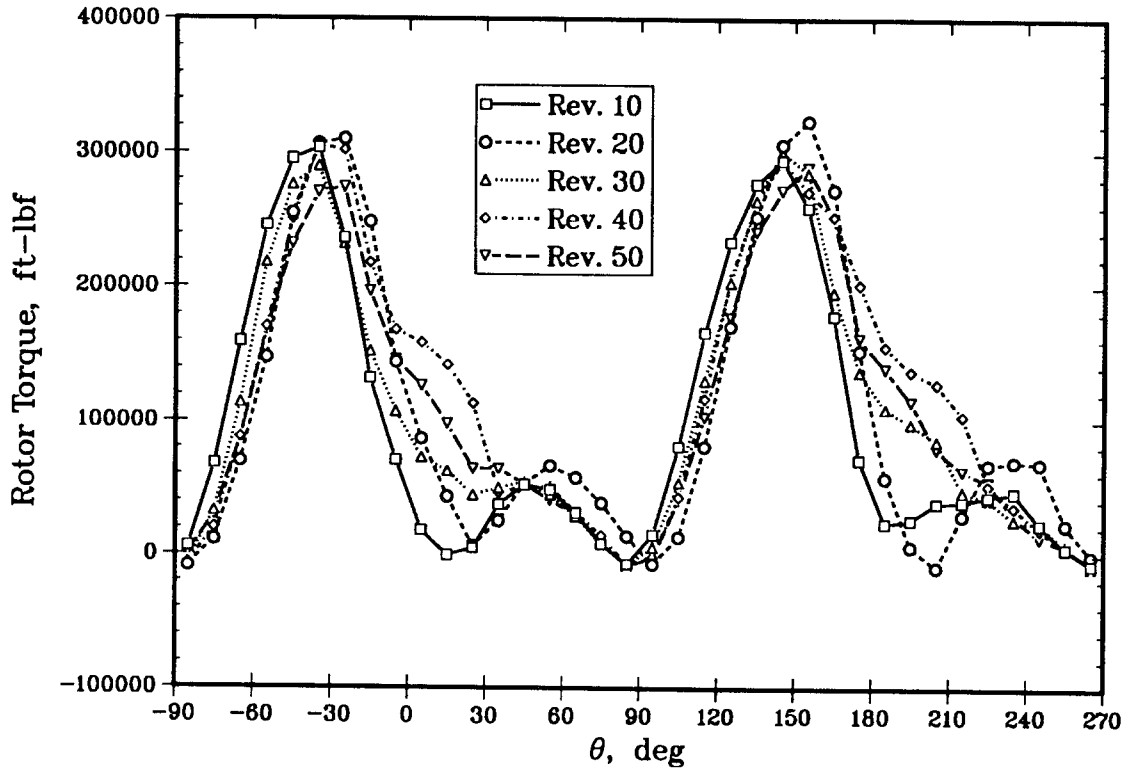


Figure 13. Instantaneous Rotor Torque vs. θ for Case 1

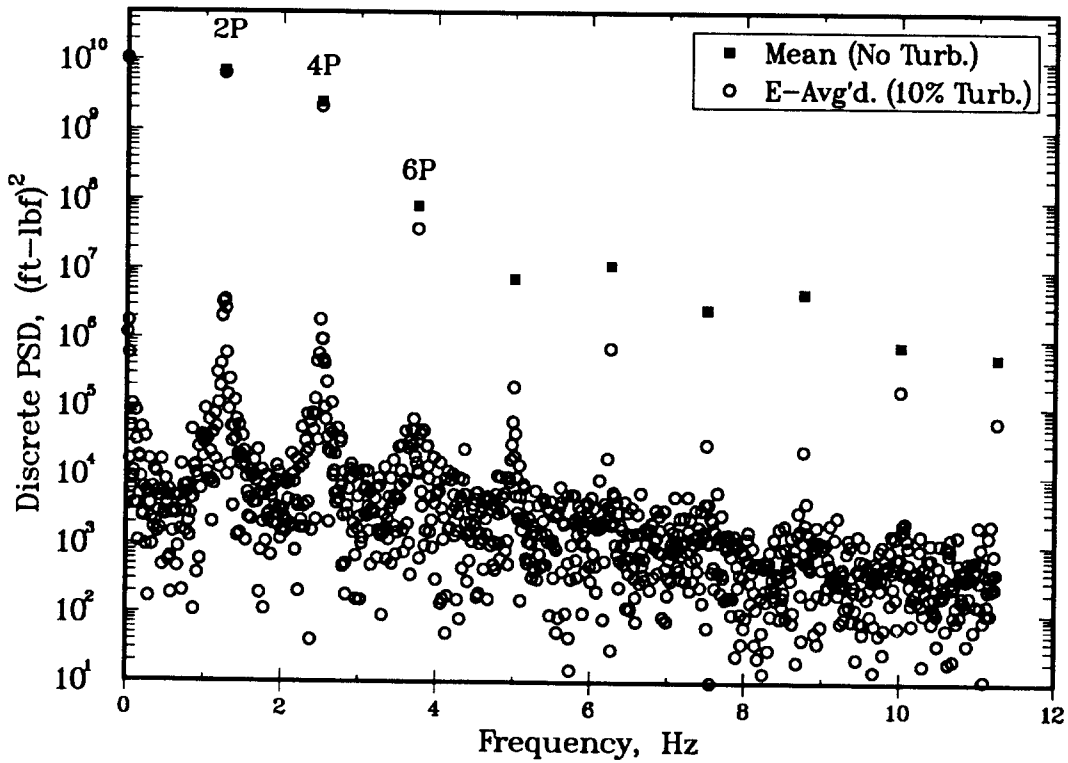


Figure 14. Mean and Ensemble-Averaged Rotor Torque PSD for Case 1

fluctuations and a higher frequency content than the ensemble-averaged curve. It should also be kept in mind that these are loads that have already been spatially integrated; the local loads are likely to be even more erratic. Clearly, this is likely to have a negative impact on blade fatigue life.

The frequency characteristics of the rotor torque are displayed more explicitly in Fig. 14, which compares the PSD of the mean rotor torque and the ensemble-averaged PSD of the stochastic fluctuations. Since the mean wind response is periodic, its spectrum is discrete. It contains a fundamental at $B\Omega$, in this case 1.25 Hz, which is labelled “2P” in the figure for “two per-rev”. Higher harmonics are also present, at 4P, 6P, etc. The most notable difference in the ensemble-averaged spectrum is the presence of significant broadband excitation at frequencies between the harmonics, reflecting the random high-frequency fluctuations in Fig. 13. The “scatter-shot” nature of the data is the result of the very close spacing between points, $\Delta f = 0.011$ Hz, and the fact that no smoothing of the spectrum has been performed. The excitations at the fundamental and first few harmonics are very little changed by the turbulence, while the higher harmonics are considerably reduced. The $f = 0$ component is practically unchanged. These findings reflect the trends in Fig. 11, *i.e.*, that the ensemble-averaged distribution smooths out ‘sharp’ features in the mean wind response, while leaving the area under the curve more or less unchanged. The average output power is directly proportional to the latter; more will be said on this later. These trends are consistent with those reported by Veers[2]. They also qualitatively corroborate the finding by Lobitz and Sullivan[37] that use of the CARDAA steady-state performance model (to which the steady-state model discussed here is quite similar) overestimates the measured blade stress response in high winds.

5.2 Case 2: 20.1 m/sec (45 mph), 30% Turbulence

Case 2 is identical with Case 1 except that the relative turbulence intensity is increased from 10% to 30%. Thus the interference factors displayed in Fig. 7 apply here as well, as do the turbulence values in Figs. 8 and 9, keeping in mind that σ_u is now three times larger. The mean and stochastic fluctuations in α_g for this case are presented in Fig. 15. Again, the solid line shows the variation produced by just the mean wind, and the open symbols that with the 30% turbulence added. As one would expect, the increased turbulence intensity relative to Fig. 10 has amplified the departures from the solid curve.

Figure 16 compares the rotor torque distribution produced by the mean wind (same as in Fig. 11) to the ensemble-averaged curve. The discrepancies between the two are much greater than for Case 1, *i.e.*, increasing the turbulence level exacerbates the influence of aerodynamic nonlinearities. This point is of more than academic interest. Steady-state performance models predict the solid curve in Figs. 11 and 16. But experimental data, to be at all meaningful, are averaged over many revolutions, and hence really represent an ensemble-average. Hence whenever data contaminated by the presence of turbulence, which is virtually unavoidable, are used to validate steady-state performance models, discrepancies of the sort shown in these figures are to be expected. They do not *necessarily* reflect inadequacies in the aerodynamic model, which is the reason often cited at low tip speed ratios. Though perhaps not obvious, the area under the dashed curve in Fig. 16 is less than that under the steady-state distribution, implying again that turbulence acts to reduce the average output power. More will be said on this in Section 5.5.

Figure 17 shows the convergence of the ensemble-averaged curve vs. the number of samples. It is interesting to observe that there appears to be somewhat less scatter exhibited in Fig. 17 compared to Fig. 12. This may simply be the result of the ensemble-averaged curve no longer passing through zero. Even at this intensity, which is probably higher than would be typical of most

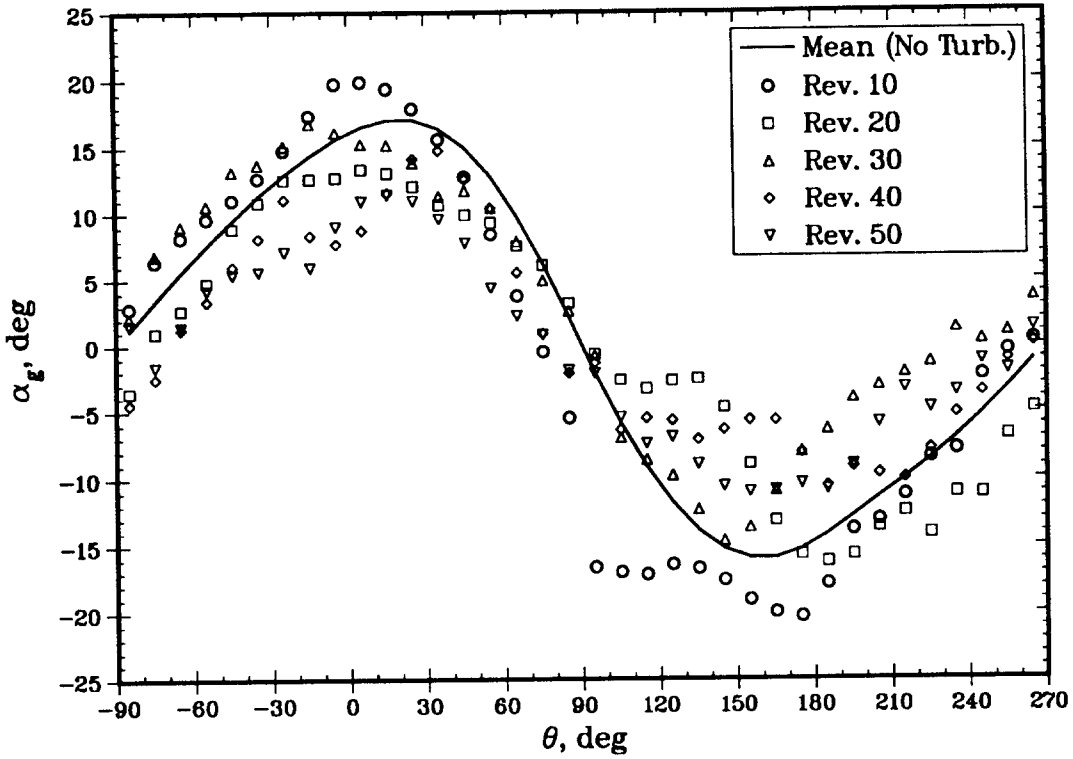


Figure 15. Variations in Angle-of-Attack for Case 2

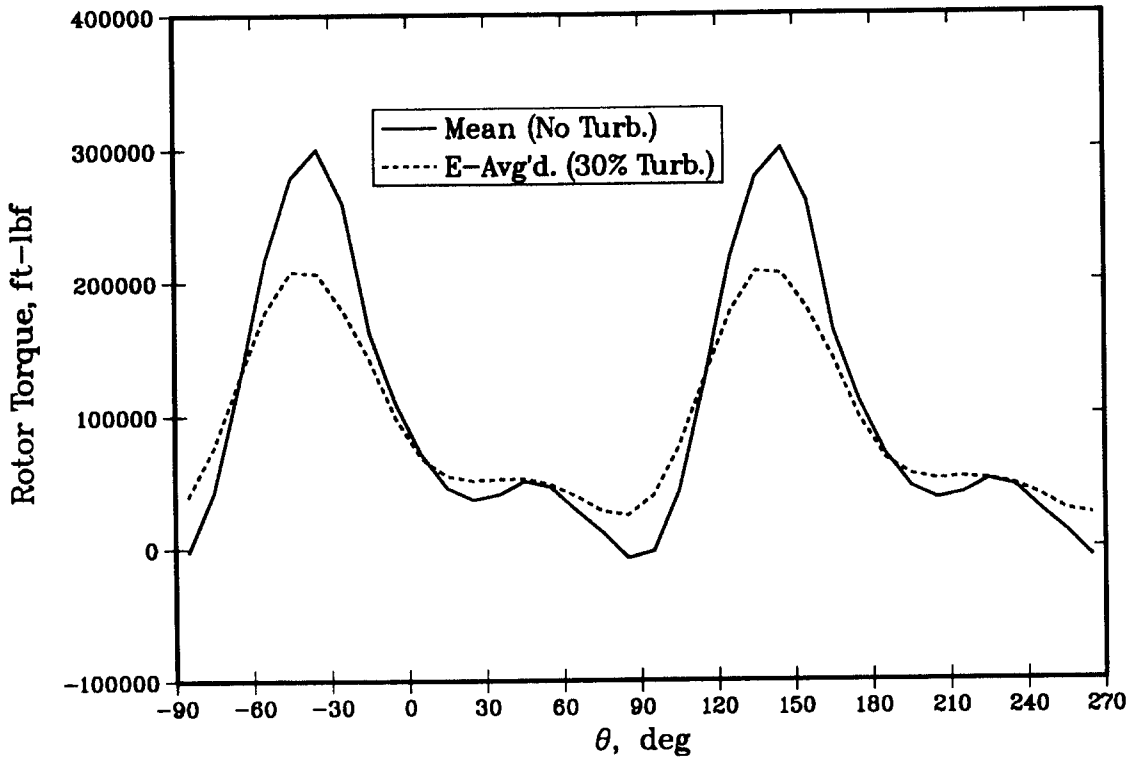


Figure 16. Mean and Ensemble-Averaged Rotor Torque vs. θ for Case 2

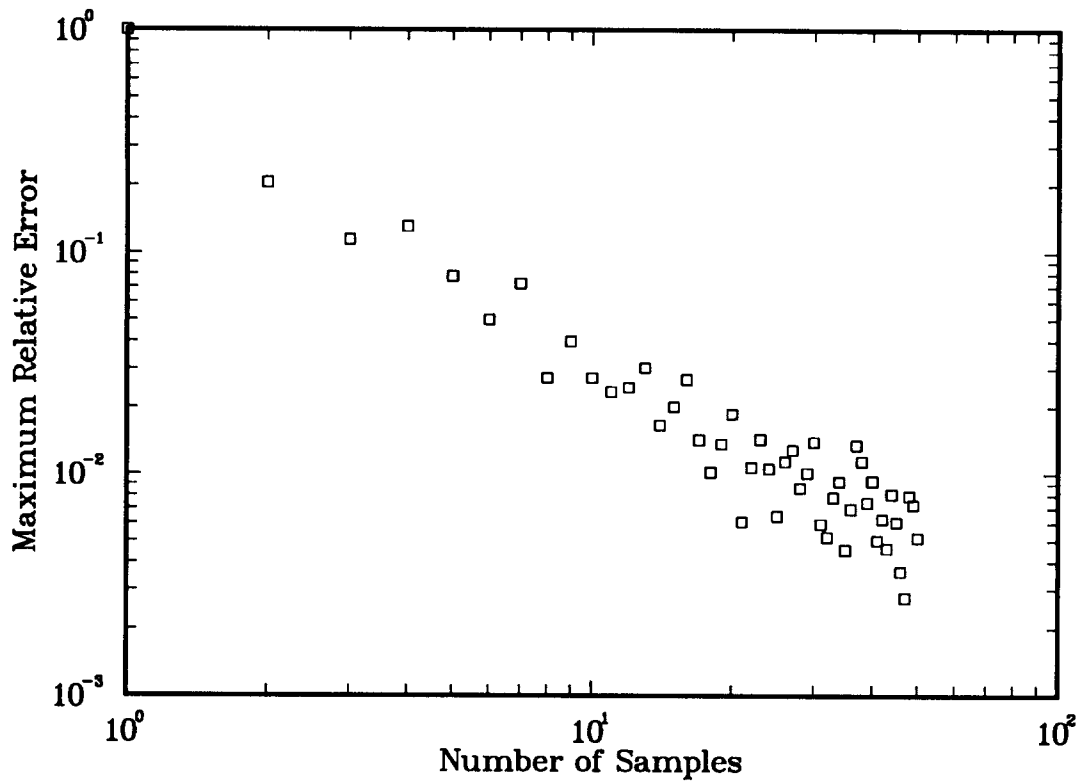


Figure 17. Maximum Relative Error vs. Number of Samples for Case 2

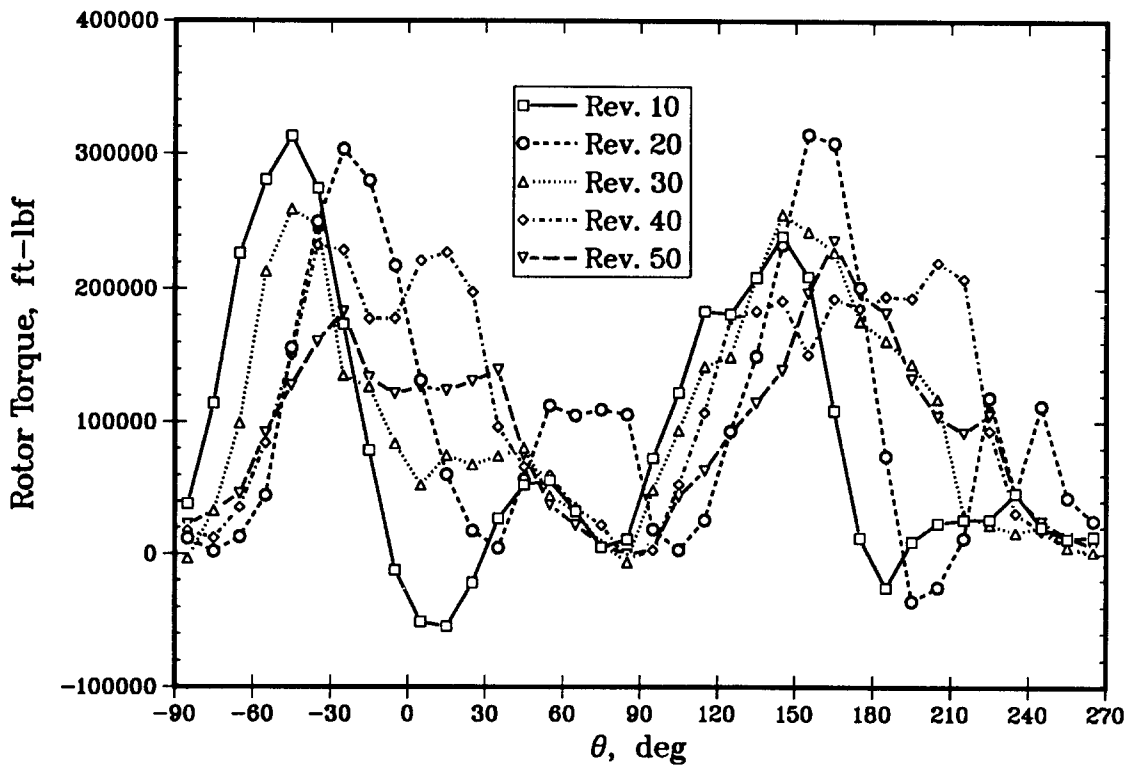


Figure 18. Instantaneous Rotor Torques vs. θ for Case 2

real world applications, it seems that simulating 30 or so samples (~ 1700 revolutions) should be adequate for most engineering purposes.

Figure 18 shows the instantaneous excursions of the rotor torque, which are considerably amplified relative to Case 1 (*cf.* Fig. 13). What's more, even the *shape* of the individual curves has been altered by the increasingly important nonlinear effects. The changes in overall level between revolutions in Fig. 18 are the result of the convection of low-frequency (large-eddy) turbulence through the turbine. The more rapid oscillations within a revolution result from a combination of the higher-frequency turbulence and changes in azimuth.

Figure 19 compares the ensemble-averaged PSD against the discrete spectrum produced by the mean wind alone; the latter is the same as was shown in Fig. 14. At the first few harmonics, levels in the ensemble-average are somewhat lower than in Fig. 14. It is difficult to discern a consistent

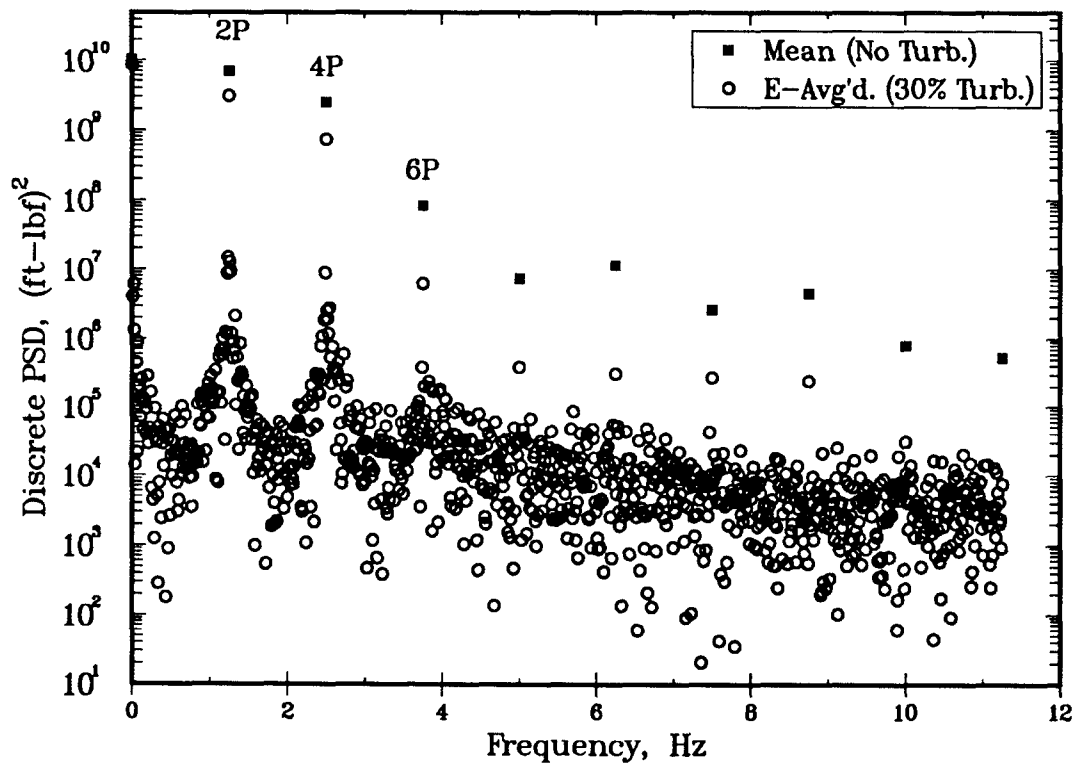


Figure 19. Mean and Ensemble-Averaged Rotor Torque PSD for Case 2

pattern in the higher harmonics, except that they disappear sooner into the broadband background, which is higher than it was for Case 1. This is consistent with a greater proportion of the variations being random in nature. Hence for Cases 1 and 2 turbulence acts to remove energy from the discrete harmonic (cyclic) frequencies, and introduces additional excitation over a broadband (random) background.

5.3 Case 3: 8.9 m/sec (20 mph), 10% Turbulence

Case 3 assumes a more moderate wind speed of $V_{ref} = 8.9$ m/sec (29.3 fps or 20 mph), and a 10% relative turbulence intensity. This mean wind corresponds to $\chi = 7.36$, which is quite near the design point. The predicted interference factors are shown in Fig. 20. As was the case with Fig. 7, the open symbols connected by solid lines are the azimuthal variation predicted by the current

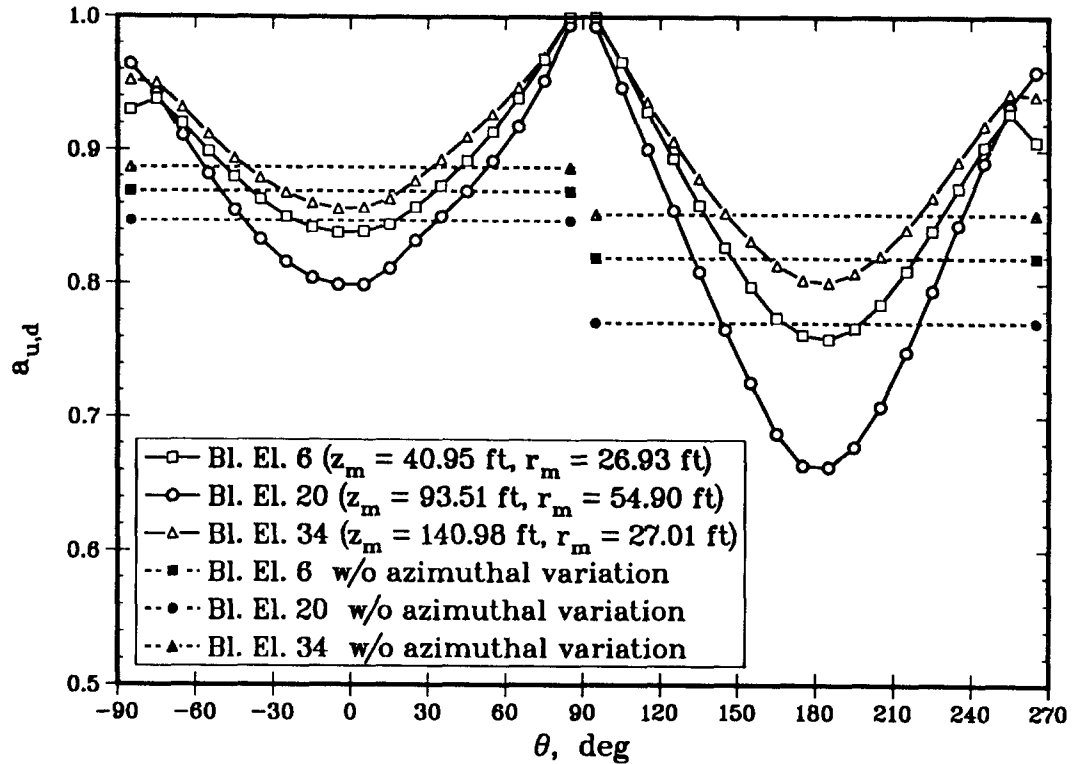


Figure 20. Aerodynamic Interference Factors for Cases 3 and 4

model; the filled in symbols connected by dashed lines are the predictions made earlier assuming the $a_{u,d}$ were independent of θ . The biggest difference between the two figures is that the $a_{u,d}$ are significantly lower at the lower wind speed, indicating a greater relative energy extraction. The reason for this can be seen in the next figure, Fig. 21, which compares the angle-of-attack variations with and without 10% turbulence present. The angle-of-attack excursions are much less than was the case in either of Figs. 10 or 15, owing to the reduced wind speed. As a result, the blades are operating in a largely unstalled condition, and hence are more efficient at extracting energy, resulting in the lower $a_{u,d}$. Note also that the θ -variation in Fig. 20 is much smoother than was the case in Fig. 7, particularly on the downwind side. This also can be attributed to the blades' remaining on the linear portion of their aerodynamic characteristics (*cf.* discussion following Fig. 7).

In addition to amplitude, there is another significant difference in the angle-of-attack distribution between the moderate and high wind speed cases. Whereas Figs. 10 and 15 exhibit variations that are more or less antisymmetric about $\theta = 90^\circ$, Fig. 21 indicates an almost constant α_g over the entire downwind passage. This would appear to contradict the obvious θ -dependence displayed by Eq. (18). However, it must be remembered that the V there is not a constant, but rather is obtained from the $a_{u,d}$ through either Eq. (19) or (24), as appropriate, and the $a_{u,d}$ themselves are now functions of θ . It just happens that at moderate windspeeds the implicit θ -dependence in $a_{u,d}$ nearly cancels the explicit dependence shown in Eq. (18). Note also that $|(\alpha_g)_{min}|$ is only about half of $|(\alpha_g)_{max}|$, whereas the simple asymptotic argument following Eq. (18) suggested they should be about equal. This serves to point out the need for caution when applying such simple rules for anything beyond order of magnitude estimates.

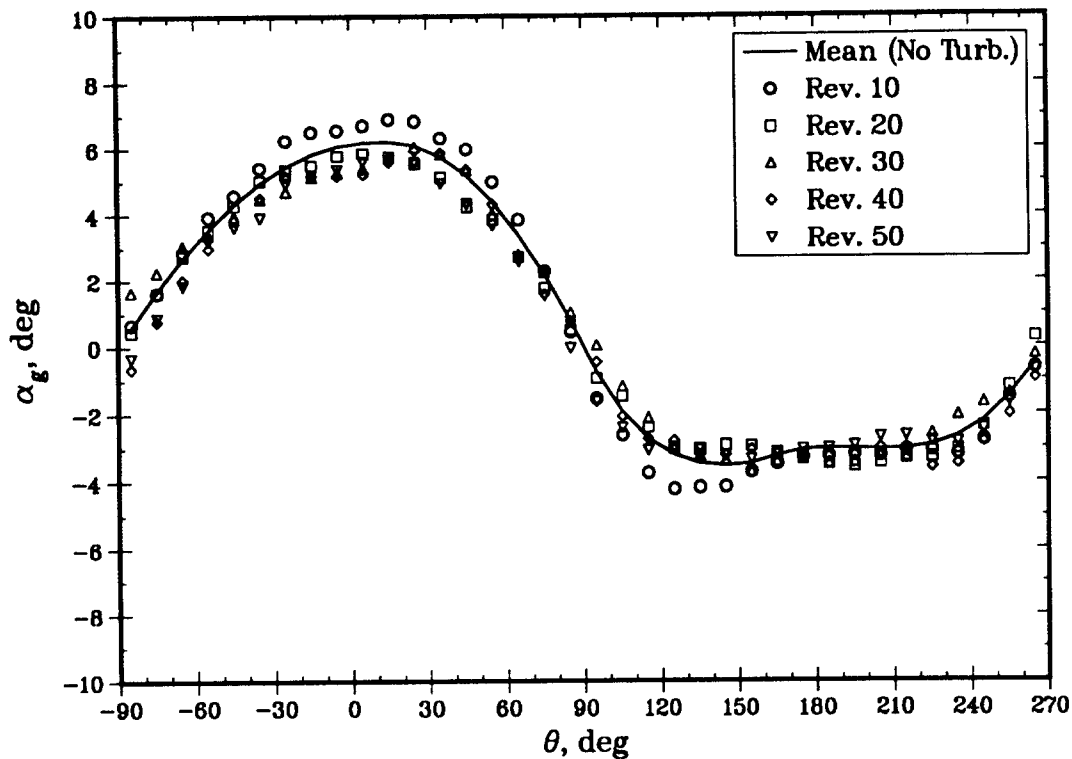


Figure 21. Variations in Angle-of-Attack for Case 3

The rotor torque distributions for Case 3 are displayed in Fig. 22. The mean wind (solid curve) and ensemble-averaged turbulent wind (dashed curve) distributions are quite close at these conditions, reflecting both the relatively low turbulence intensity and the blades' largely linear aerodynamic response. Compared with Cases 1 and 2, the steady-state analysis predicts less absolute power, $P_0 = 178$ kw, but this represents a much higher fraction of what is available, since $C_p = 0.44$. The rotor is much more aerodynamically efficient, but there is less wind energy available to convert at 8.9 m/sec compared with 20.1 m/sec. (Note the different scales used for the ordinate in Figs. 11 and 16 vs. Fig. 22.) The variations in Fig. 22 are also smoother, owing to the lack of nonlinear stall phenomena. As before, including turbulence in the simulations reduces the peak levels, while increasing the valleys. The net effect on the area under the curve, and hence the average output power, is difficult to ascertain by eye, but it turns out that P is increased slightly by the presence of the turbulence in this case. The convergence of the ensemble-averaged distribution is shown in Fig. 23, and is qualitatively similar to that in the previous cases.

The instantaneous rotor torque fluctuations for five separate revolutions are shown in Fig. 24, and again show significant departures from their average. The mean and ensemble-averaged rotor torque PSD are compared in Fig. 25. These spectra, both with and without turbulence, exhibit a more rapid falloff in excitation level at the harmonic frequencies than was the case at 45 mph (*cf.* Fig. 14). This is consistent with the curves in Fig. 22 being smoother, and hence less "impulsive", than those in Fig. 11. Interestingly, the addition of turbulence in this case seems not to reduce the harmonic levels as much as before; indeed, a few of the harmonics (at 4P, 8P, 14P, and 16P) are actually *increased* relative to the mean wind spectrum. Also note that, whereas the background continuum excitation in Fig. 14 was about 6–7 decades below the $f = 0$ (average) component, in Fig. 25 it is more like 7–8 decades below. All this suggests that when turbulence is introduced into

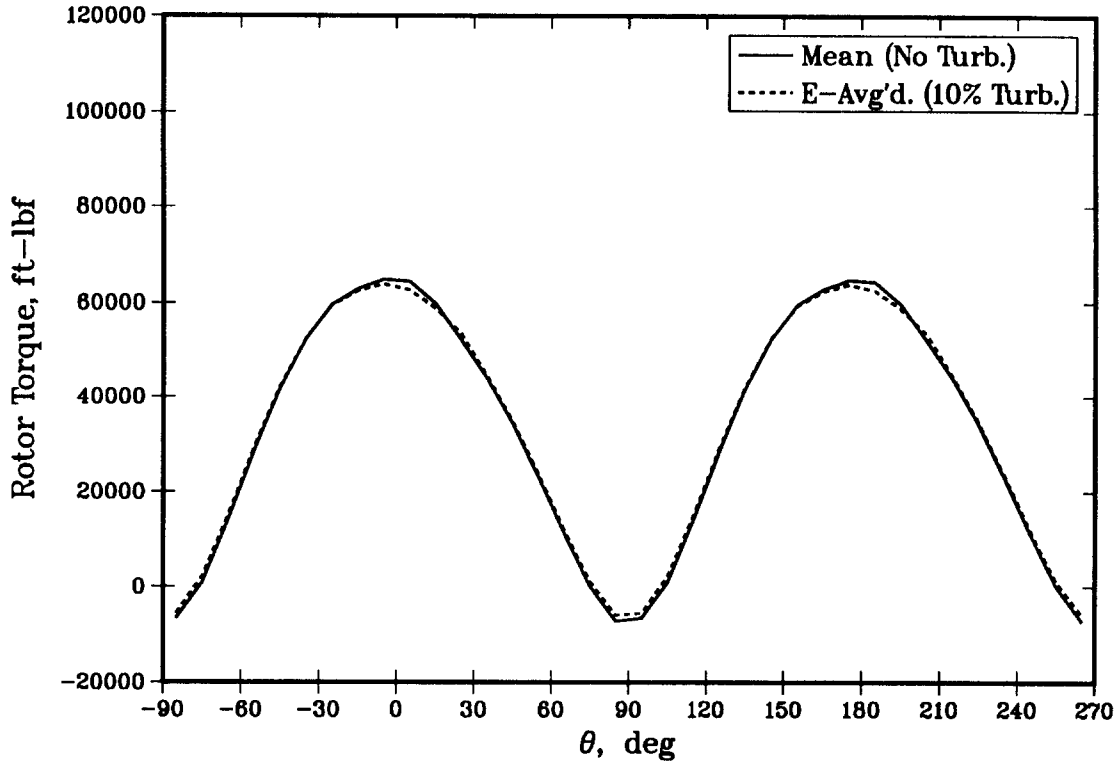


Figure 22. Mean and Ensemble-Averaged Rotor Torque vs. θ for Case 3

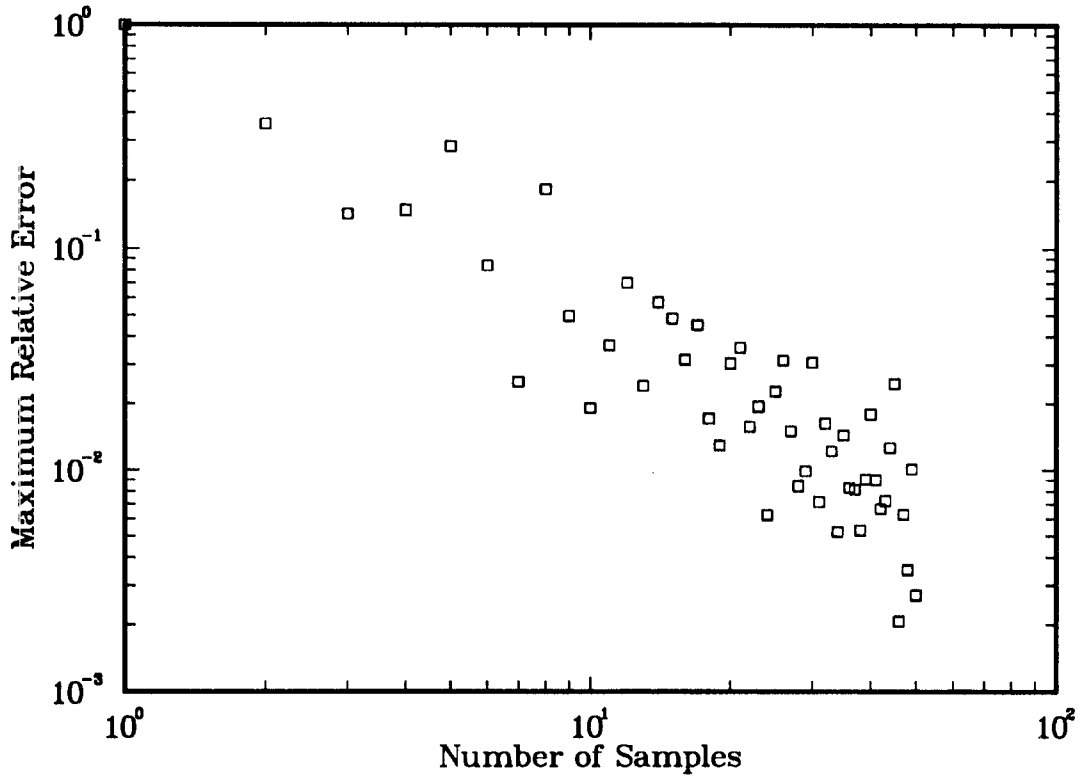


Figure 23. Maximum Relative Error vs. Number of Samples for Case 3

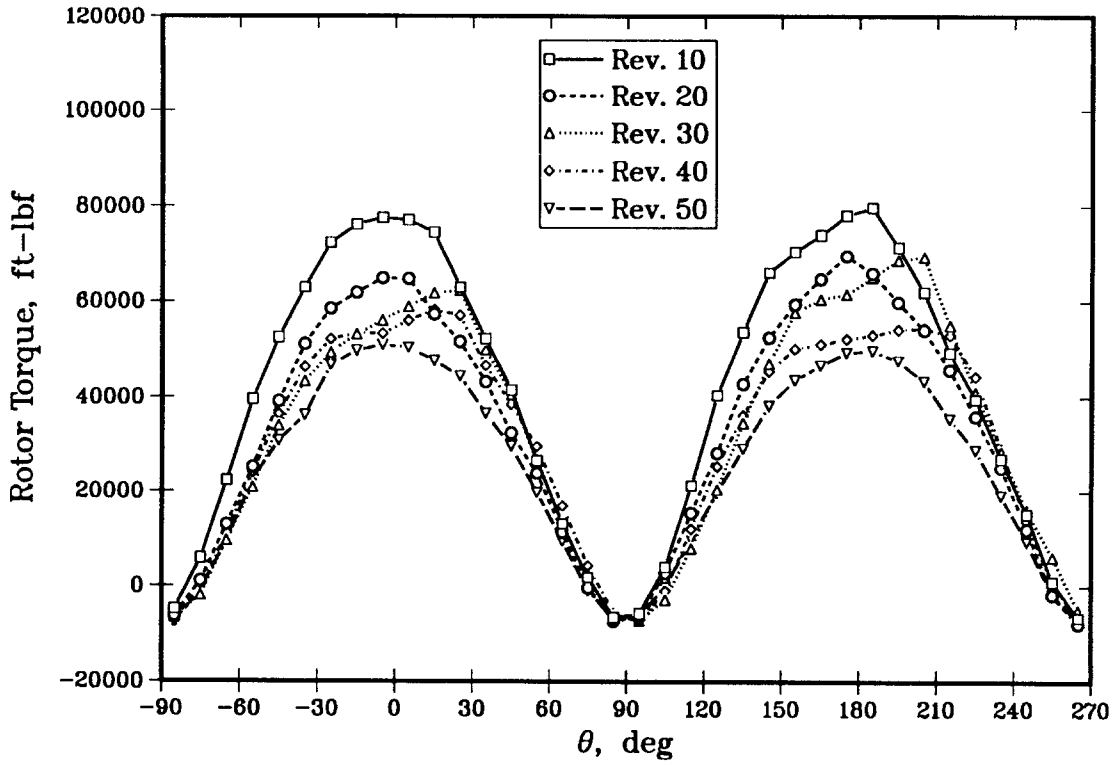


Figure 24. Instantaneous Rotor Torque vs. θ for Case 3

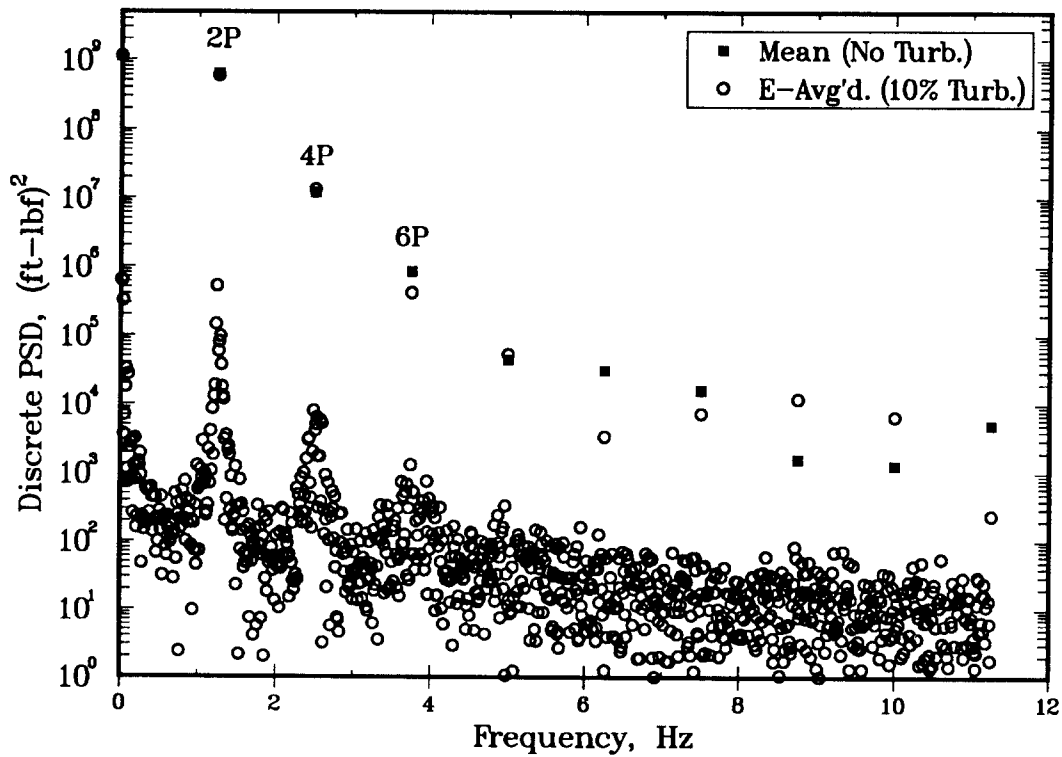


Figure 25. Mean and Ensemble-Averaged Rotor Torque PSD for Case 3

the simulation, the more linear a rotor's aerodynamic response, the more energy will be retained by harmonics in the load fluctuations, and less in the broadband (*i.e.*, random) background. Of course, such a conclusion would need to be corroborated with experimental data. Though imperceptible on a logarithmic scale, the turbulence also creates a slight increase in the $f=0$ level; this is another manifestation of the rise in average power mentioned above in connection with Fig. 22.

5.4 Case 4: 8.9 m/sec (20 mph), 30% Turbulence

Case 4 is identical to Case 3, except that the relative turbulence intensity is increased from 10% to 30%. Hence the interference factors shown in Fig. 20 for Case 3 apply here as well. The increased turbulence is apparent in Fig. 26, which shows the steady-state (same as in Fig. 21) and

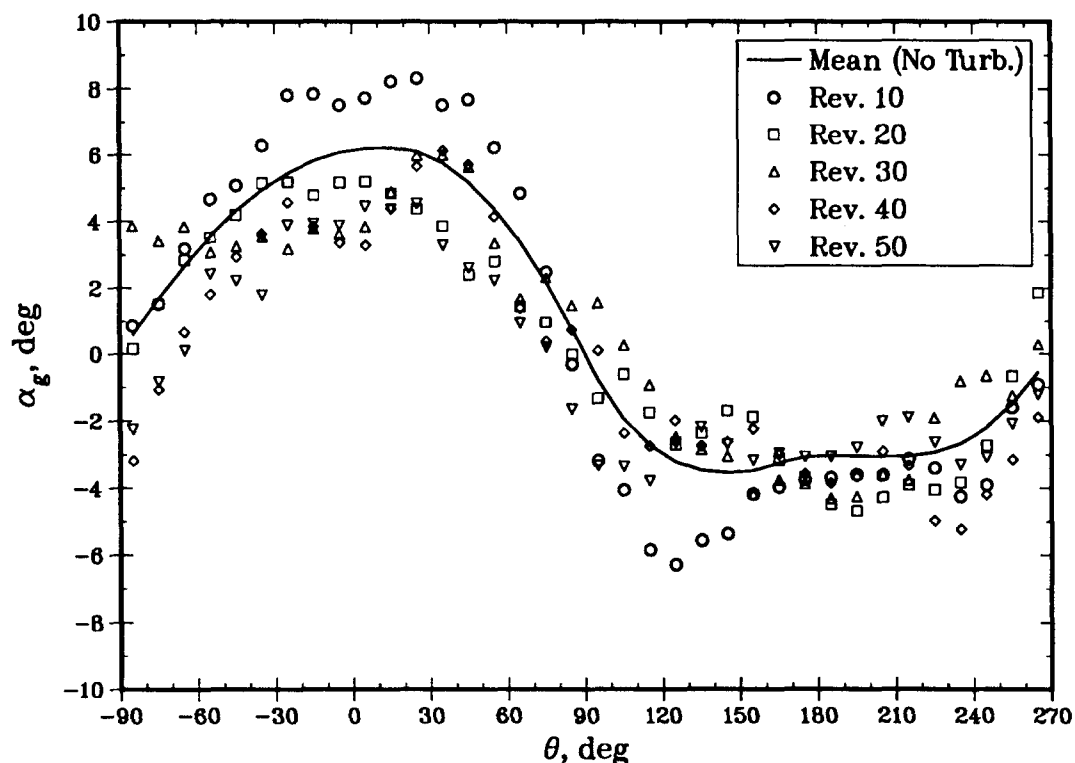


Figure 26. Variations in Angle-of-Attack for Case 4

stochastic variations in α_g . Even on the downwind passage, where the mean wind produces a relatively constant α_g , individual revolutions exhibit significant fluctuations at this intensity. Figure 27 presents the mean-wind rotor torque vs. θ (same as in Fig. 22), compared with the ensemble-average of the stochastic variations. This plot shows significantly greater deviations between the two curves than was the case in Fig. 22 for 10% turbulence at the same mean wind speed. On the other hand, the differences are not as great as they were in Fig. 16, which had the same turbulence intensity but at a much higher wind speed where the blades are stalled much of the time. This suggests that the primary factor determining the divergence of these two curves is the degree to which the aerodynamic response is nonlinear, which is mainly a function of mean wind speed. Secondly, increased turbulence intensity will cause the two to deviate more, because it exacerbates whatever nonlinearities are present.

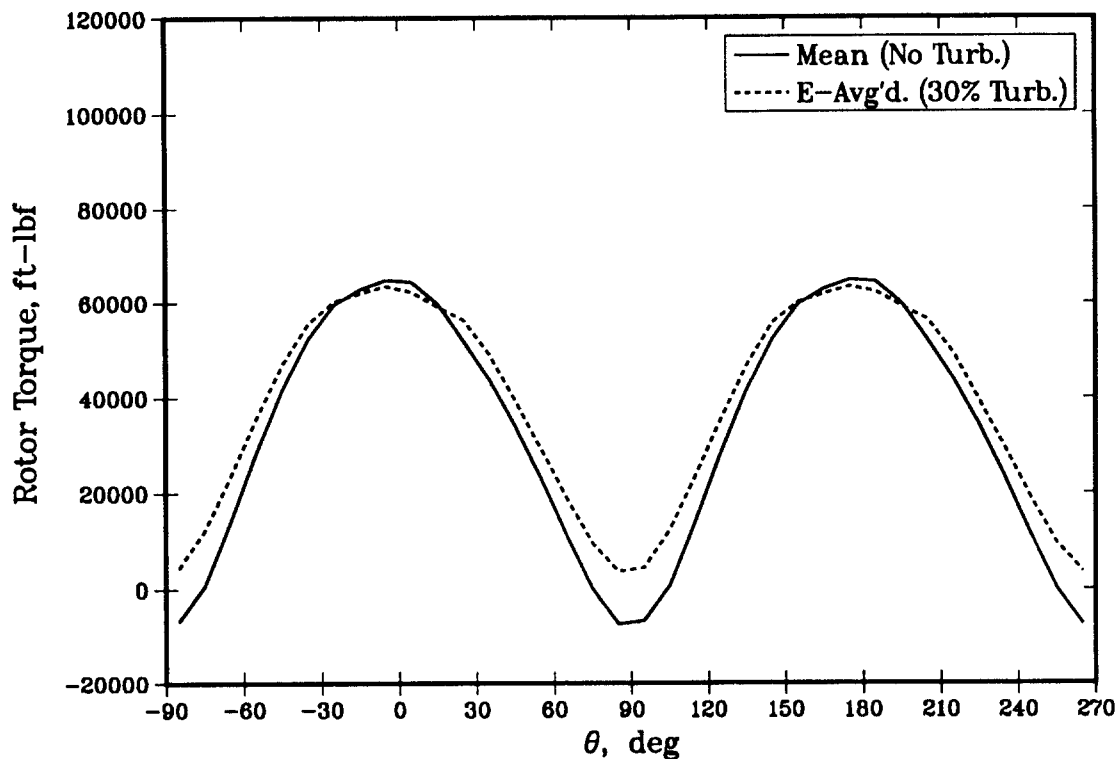


Figure 27. Mean and Ensemble-Averaged Rotor Torque vs. θ for Case 4

Consistent with the previous cases, turbulence acts to reduce the peaks, and raise the valleys, relative to a mean-wind-only calculation. In this case, it is evident that the valleys have been raised more than the peaks have been lowered. This means that the area under the curve, and hence the average output power, is increased by the presence of turbulence. This influence of turbulence on output power will be discussed at more length in the next section. The convergence of the ensemble-averaged distribution is shown in Fig. 28. Again, there seems to be somewhat less scatter in these data than was exhibited in Fig. 23, which is probably the result of the dashed curve in Fig. 27 no longer passing through zero.

Figure 29 displays the instantaneous variations, which for this case are quite extreme. For example, the peak loading during Revolution 10 exceeds the mean wind response by some 60–70% at times. These fluctuations also appear more erratic than those in Fig. 24 for 10% turbulence. It should be noted that even though the loading magnitudes for Cases 3 and 4 (Figs. 24 and 29) are well below those for Cases 1 and 2 (Figs. 13 and 18), the former may ultimately be responsible for most of the blade fatigue damage. This is because fatigue is a cumulative phenomena, and a turbine is likely to spend the great majority of its life in moderate winds; the mean wind of 20.1 m/sec (45 mph) assumed for Cases 1 and 2 is getting near the point at which most turbines would be shut down.

Finally, Fig. 30 compares the mean and ensemble-averaged rotor torque PSD. In contrast to Fig. 25, here the only harmonics increased by turbulence are those at 4P, 10P, 12P, and 14P. The increased turbulence intensity has also increased the broadband background in the ensemble-averaged spectrum. The rise in the $f = 0$ level is greater than that in Fig. 25, reflecting the obvious increase in average torque level in Fig. 27.

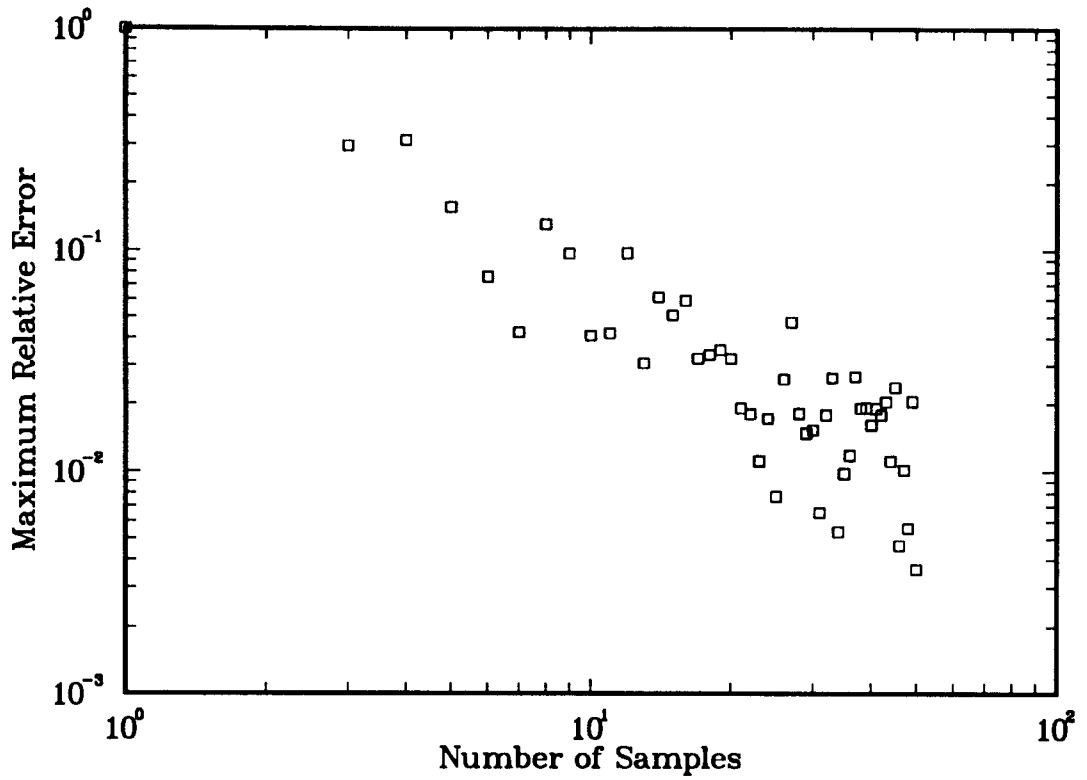


Figure 28. Maximum Relative Error vs. Number of Samples for Case 4

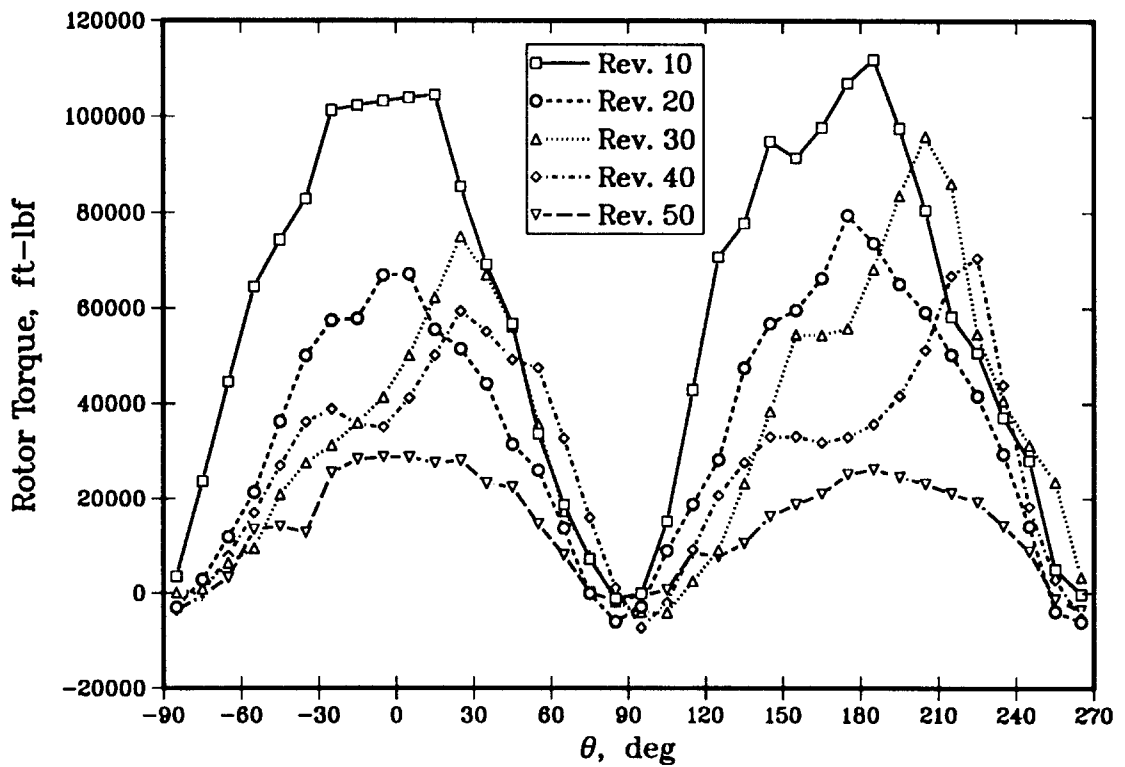


Figure 29. Instantaneous Rotor Torque vs. θ for Case 4

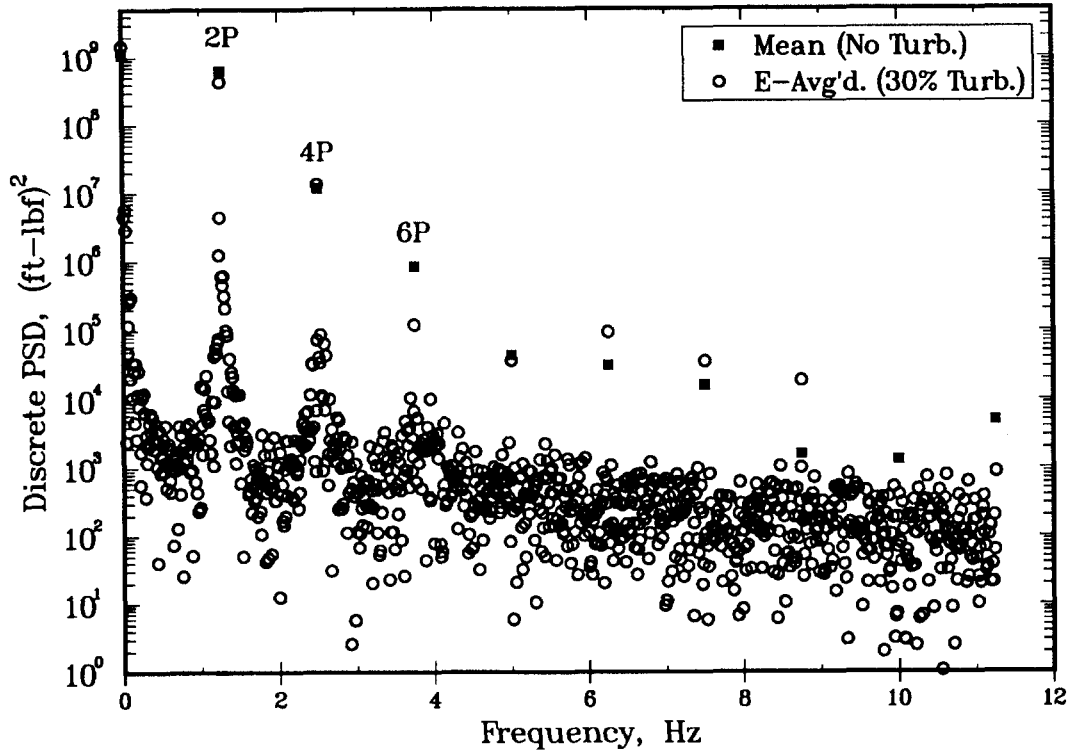


Figure 30. Mean and Ensemble-Averaged Rotor Torque PSD for Case 4

5.5 Effect of Turbulence on Average Output Power

The increased area under the ensemble-averaged curve compared to the mean wind curve in Fig. 27 (and to a lesser extent in Fig. 22) means that the turbulence has the effect of increasing the time-averaged torque, \overline{T}_t , and hence P . The increase is about 15% for Case 4. But in Cases 1 and 2 the predicted effect was a *decrease* in power. Examination of the results shows the predicted ratio of average power with turbulence, to the average power without turbulence in the same mean wind, $\langle P \rangle / P_0$, for Cases 1–4 is 0.99, 0.92, 1.01, and 1.15, respectively. Turbulence apparently lowers the output power at low tip speed ratio, and increases it at high tip speed ratio.

Classical View. This stands in contrast to the classical view that turbulence always acts to increase output power, as based on the following argument (see *e.g.*, de Vries[38], §2.2). If Eq. (76) is rewritten with P as the unknown variable, and for simplicity we drop the subscript on V :

$$P = \frac{1}{2} \rho V^3 A C_p \quad , \quad (77)$$

the explicit dependence of P on the third power of some characteristic velocity is displayed. If the ambient wind is perfectly steady in time, there is no ambiguity. But with turbulence present, $V \equiv \langle V \rangle + u$. If this is substituted in the above relation, and the resulting cubic expanded, we get

$$P = \frac{1}{2} \rho A C_p [\langle V \rangle^3 + 3u \langle V \rangle^2 + 3 \langle V \rangle u^2 + u^3] \quad .$$

If we ensemble-average this expression, the term proportional to u drops out, since by definition $\langle u \rangle = 0$. Similarly, if we make the reasonable approximation that the probability density function

for u is symmetric, *i.e.*, positive and negative values are equally likely to occur, then the average of u^3 is zero as well. The result is

$$\langle P \rangle = \frac{1}{2} \rho A C_P [\langle V \rangle^3 + 3 \langle V \rangle \langle u^2 \rangle] .$$

Because we have assumed that the turbulence statistics are stationary in time, the ensemble-averages are equivalent to time-averages, $\langle V \rangle = \bar{V}$, and $\langle u^2 \rangle = \bar{u}^2$. Hence, this analysis predicts that the ratio $\langle P \rangle / P_0$ will be of the form:

$$\frac{\langle P \rangle}{P_0} = 1 + 3 \left(\frac{\sigma_u}{\bar{V}} \right)^2 . \quad (78)$$

The second term is always positive, and hence leads to the conclusion that turbulence always increases output power. Simply stated, in a turbulent flow the average of the wind speed cubed is greater than the cube of the average wind speed; hence the available energy flux will increase, leading to an increase in output power, *provided C_P is independent of V* .

Postulate. To ascertain the degree to which C_P depends on V , the model was run at $\Omega = 37.5$ rpm, with the turbulence simulation turned off, for one hundred equally-spaced values of V_{ref} , corresponding approximately to $2 < \chi < 11$. Figure 31 shows the resulting steady-state performance

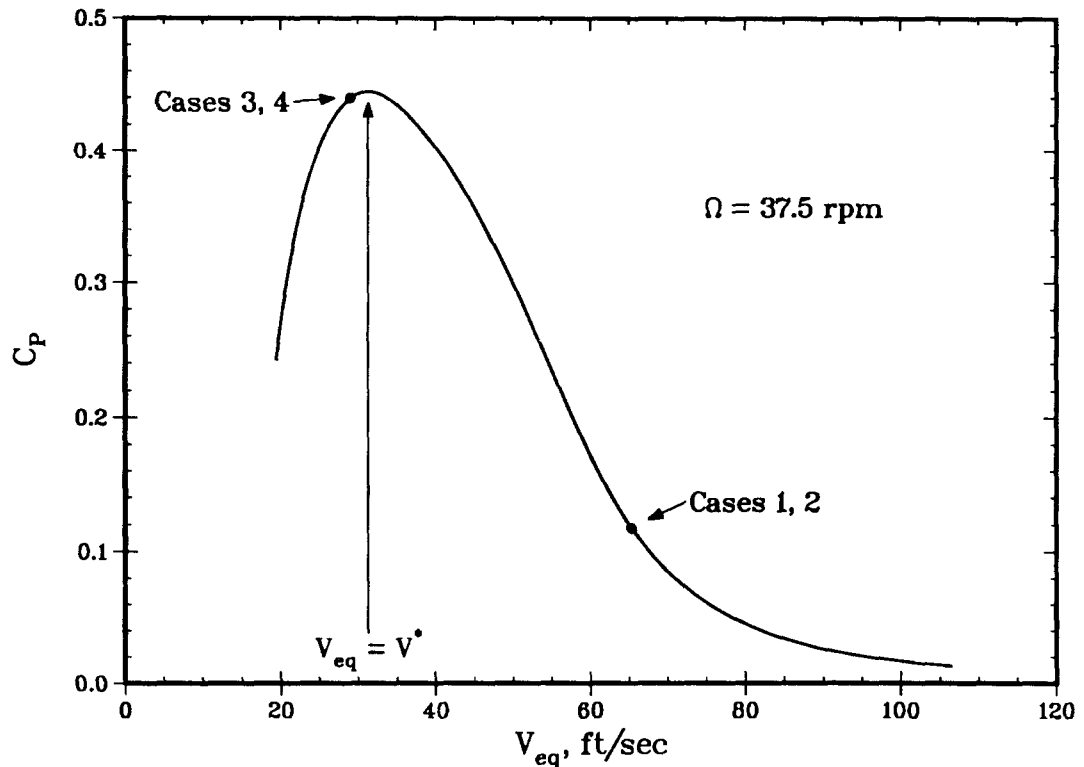


Figure 31. Steady-State Performance Curve for Constant Ω

curve of C_P vs. V_{eq} . It is evident that C_P is strongly dependent on V_{eq} , with a well-defined peak at V^* (in this case ~ 10 m/sec (32 fps)), trailing off sharply to either side. As one moves away from the maximum for $V_{eq} > V^*$, the blades get progressively deeper into stall, resulting in a loss of aerodynamic efficiency, with $C_P \rightarrow 0$. Going in the other direction $V_{eq} < V^*$, the angle-of-attack gets ever smaller and C_P decreases because the L/D ratio of the blades is progressively less

favorable. If the curve had been continued until $V_{eq} \rightarrow 0$, the lift would vanish altogether, leaving a finite drag that must be overcome to turn the rotor; hence C_p would actually go negative. The shape of this curve is typical of constant rpm operation, even for HAWT designs, though the details will vary depending on the particular configuration.

It is postulated that changes in the ambient wind created by turbulence can be viewed parametrically as movements back and forth along a curve such as this. The operating points corresponding to the four stochastic cases discussed earlier are indicated in Fig 31. Cases 1 and 2 lie well to the right of the maximum. Though turbulence increases the available energy at some instants, this is more than offset by the decline in C_p . Conversely, during those instants when the wind is down, C_p will rise, but not enough to compensate for the reduced energy available. The net result is a decline in average power with increasing turbulence intensity, albeit a weak one. Cases 3 and 4 lie very near the maximum; in this vicinity C_p is much less sensitive to changes in the wind. Here the turbine can take advantage of the added energy available during high wind periods without stalling. This more than makes up for the reduced output during low wind gusts. The net result is an increase in average power out with increasing turbulence intensity.

Analysis. The question remaining is whether such heuristic reasoning can be incorporated into an analytical prediction analogous to Eq. (78). Let us start again from Eq. (77), and this time expand the right-hand side in a Taylor series about the nominal operating point $\langle V \rangle = \bar{V}$:

$$P = \frac{1}{2} \rho A \left\{ \bar{V}^3 C_p(\bar{V}) + \left[\frac{d(V^3 C_p)}{dV} \right]_0 (V - \bar{V}) + \frac{1}{2} \left[\frac{d^2(V^3 C_p)}{dV^2} \right]_0 (V - \bar{V})^2 + \frac{1}{6} \left[\frac{d^3(V^3 C_p)}{dV^3} \right]_0 (V - \bar{V})^3 + \dots O(V - \bar{V})^4 \right\}$$

where $[\dots]_0$ indicates a quantity evaluated at $V = \bar{V}$. Now $(V - \bar{V}) = u$, so upon averaging this expression, the second and fourth terms on the right will vanish for the same reasons cited before. After some manipulation, we are left with:

$$\frac{\langle P \rangle}{P_0} = 1 + \frac{1}{2 \bar{V} C_p(\bar{V})} \left[\frac{d^2(V^3 C_p)}{dV^2} \right]_0 \left(\frac{\sigma_u}{\bar{V}} \right)^2,$$

where terms of $O(\sigma_u \bar{V})^4$ have been neglected. It seems natural to define a turbine's *power sensitivity to turbulence*, S_t , as the ratio of the relative change in output power to the square of the relative turbulence intensity, *i.e.*,

$$S_t \equiv \frac{\frac{\langle P \rangle}{P_0} - 1}{\left(\frac{\sigma_u}{\bar{V}} \right)^2} \quad (79)$$

Thus, positive and negative values of S_t correspond, respectively, to an increase or decrease in output power. The classical result, Eq. (78), thus predicts $S_t = 3$, while the above analysis suggests

$$S_t = \frac{1}{2 \bar{V} C_p(\bar{V})} \left[\frac{d^2(V^3 C_p)}{dV^2} \right]_0 = 3 + 3 \left(\frac{V}{C_p} \frac{dC_p}{dV} \right)_0 + \frac{1}{2} \left(\frac{V^2}{C_p} \frac{d^2 C_p}{dV^2} \right)_0 \quad (80)$$

We see that the only differences lie in those terms which recognize the variation of C_p with V . The important thing to keep in mind regarding this result is that the only information required to evaluate it is a steady-state performance curve, such as that shown in Fig. 31. No stochastic simulations are involved.

The same data used to plot Fig. 31 are replotted in Fig. 32 as the open circles, to emphasize their discrete nature. As a first attempt to evaluate Eq. (80), finite-differences were applied directly to the raw data, which proved unsatisfactory. Any such discrete data, whether generated numerically or through measurement, inevitably contain errors which are amplified through differentiation. Even though the raw data in the present case were smoothly varying, the first derivative showed moderate contamination by noise; in the second derivative, "hash" was so prevalent as to render it meaningless. In addition, significantly different results were obtained depending on whether one

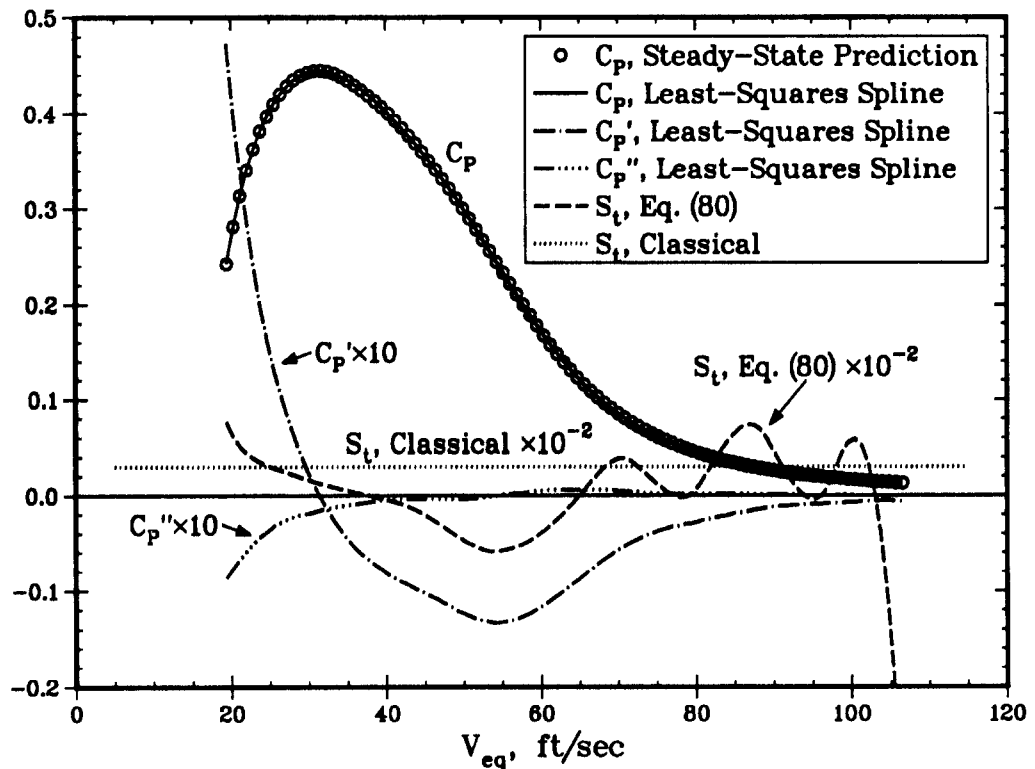


Figure 32. Turbine Power Sensitivity to Turbulence, S_t

chose to use centered, backward, or forward differences, and whether they were first- or second-order, *etc.* This prevented placing much confidence in the results.

In an attempt to avoid differencing the raw data, the next try consisted of fitting the C_p vs. V_{eq} data exactly, using splines of various orders. The spline fit was then used to analytically evaluate the needed derivatives. The results of this exercise were not much better.

The fact that the errors causing the noise were random suggested that a better approach might be to not fit the raw data exactly, but only in an approximate sense. The additional degrees of freedom accorded by not having to pass right through the data can be used to guarantee continuity of higher-order derivatives, which is what we desire. Accordingly, the unconstrained least-squares spline routine EFC from the SLATEC Library (Ref. [39]) was used to fit the data; this gave a much more satisfactory result. The smoothest results were obtained by fitting a 5th order spline

(polynomials of degree 4), and enforcing continuity at 11 equally-spaced “knots” over the data interval, including the two endpoints. This is shown as the solid curve in Fig. 32. It is clear that even though the data were only fit in a least-squares sense, the naked eye could not differentiate this from an exact fit. Also shown are two curves representing $10 \times C_p'$ and $10 \times C_p''$, respectively, as determined from the spline fit. (Note that different scale factors have been applied to the various curves in Fig. 32 to enable a common ordinate to be used for all.) These were used to evaluate S_i from Eq. (80); the result, multiplied by 10^{-2} , is displayed as the dashed line in Fig. 32. The classical result, $S_i = 3$, is shown for comparison as a dotted line.

S_i from Eq. (80) shows considerable deviation from the classical result. Below ~ 25 fps, it is positive and greater than the classical result. Between 25 and 40 fps, S_i falls below the classical result, but remains positive. From 40 to about 65 fps S_i becomes negative, indicating a decrease in output power due to turbulence. For $V_{eq} > 70$ fps the curve begins to oscillate; in retrospect, this is not surprising. As Fig. 32 plainly shows, not only C_p , but also C_p' and C_p'' , asymptote toward zero. As C_p' and C_p'' become negligible, Eq. (80) shows that $S_i \rightarrow 3$, the classical result. The oscillations, which appear to have a mean value very near 3, are an artifact introduced by the random noise in the data. Thus, the “true” curve of S_i vs. V_{eq} would probably coincide with that shown in the figure below 60–70 fps, and then asymptote into the classical result.

Analysis vs. Stochastic Simulations. Finally, comparisons were made between the changes in output power as predicted by this approximate analysis and the stochastic simulations discussed in Sections 5.1–5.4. These are summarized in Table 1 below for the four cases presented thus far, plus

Table 1. Predicted Changes in Output Power Produced by Turbulence
(Numerical values represent $\langle P \rangle / P_0$)

	Case 1 $V_{eq} = 65.57$ fps 10% Turb.	Case 2 $V_{eq} = 65.57$ fps 30% Turb.	Case 3 $V_{eq} = 29.08$ fps 10% Turb.	Case 4 $V_{eq} = 29.08$ fps 30% Turb.	Case 5 $V_{eq} = 54.48$ fps 10% Turb.	Case 6 $V_{eq} = 54.48$ fps 30% Turb.
Stochastic Simulation	0.994	0.915	1.009	1.152	0.977	0.862
Eqs. (79)–(80)	1.004	1.035	1.019	1.172	0.941	0.465

two additional cases introduced for reasons to be discussed shortly. Note that the mean wind speeds quoted here are in terms of V_{eq} , rather than V_{ref} , to allow easier correlation with Fig. 32. The first row of figures are the values of $\langle P \rangle / P_0$ predicted by the stochastic simulations; the second row are those predicted by Eqs. (79)–(80). The agreement for Cases 1 and 2 is not very good—the numerical model predicts a decrease in power, while the approximate formula predicts a slight increase. In hindsight, Cases 1 and 2 are perhaps too severe a test of such an analysis because they lie practically at the point where S_i makes its second pass through zero (Fig. 32). Small errors in the numerical data could cause the location of this zero to shift slightly. In fact, in the earlier version of the code which assumed the $a_{u,d}$ were independent of θ , a similar comparison exhibited a negative (though very small) S_i , and hence values of $\langle P \rangle / P_0 < 1$. The approximate formula does a much better job for Cases 3 and 4, for which its predictions are within a few percent of the simulations at both turbulence levels. Cases 5 and 6, which are not discussed in any detail here,

were run to assess the ability of the formula to mimic a falloff in power well away from any zeroes of S_t . The wind speed was chosen to be near the minimum S_t in Fig. 32. The simulations and the simple analysis exhibit qualitative agreement in that both predict declines in output power, but the latter significantly overestimates the magnitude of the change.

Perhaps good quantitative agreement is too much to expect from such an analysis. After all, it totally neglects the effects of fluctuations in v , lateral variations in u and v , and other details included in the stochastic simulations. Also, treating turbulence as a small perturbation of the mean wind, as implied by the Taylor series expansion leading to Eqs. (79)–(80), may not be justified at intensities of 30%. Including terms of $O(\sigma_u/\bar{V})^4$ could conceivably improve the agreement, but in light of the approximations in both the simulations and the simple analysis, this is doubtful. The analysis serves mainly as a reminder that it may be an oversimplification to assume that turbulence will always increase output power. The possibility that power could either increase or decrease depending on the operating conditions was anticipated earlier by Hansen[40], though no experimental or numerical evidence was cited. Interestingly, the present results also parallel those of Swift and Kirkland[41] in their study of turbulence effects on HAWT designs. Whether such an effect can be measured in the field remains to be seen; to the author's knowledge, quantitative data on the effects of turbulence on output power have never been published. This point is raised again in Section 6 in connection with suggested future work.

5.6 Run Times

Running on a VAX 8820, Cases 1, 2, 5 and 6 each consumed approximately 145–160 min of CPU time. Cases 3 and 4 took approximately 120 – 130 min. This difference is attributed primarily to the fact that the first group was for conditions where the blades are stalled, and more interpolations are required to evaluate the Gormont dynamic stall model, as compared to when the blades are operating on the linear portion of their characteristics. Of the total time, only ~ 10–12 sec is consumed by the mean wind (steady-state) response calculation, including the iterations for the $a_{u,d}$. For the stochastic response, run time varies nearly linearly with the number of node points at which loads are requested times the total number of time steps. Hence, a more meaningful performance figure is CPU time/(node point - time step), which is in the range $(1.0 - 1.3) \times 10^{-3}$ sec.

6 CONCLUSIONS & SUGGESTIONS FOR FUTURE WORK

This report has described the theory underlying the VAWT Stochastic Aerodynamic Loads (VAWT-SAL) computer code, whose purpose is to numerically simulate the random loads created by atmospheric turbulence. The code employs a Double-Multiple-StreamTube (DMST) analysis, which is a combination of actuator-disc and blade element theories, for predicting the rotor's aerodynamic response. The analysis includes the effects of Reynolds number variations, different airfoil sections and chord lengths along the blade span, and an empirical model for dynamic stall effects. The mean ambient wind is assumed to have a shear profile which is described by either a power law or a logarithmic variation with height above ground. Superimposed on this is a full 3-D field of turbulence: *i.e.*, in addition to random fluctuations in time, the turbulence is allowed to vary randomly in planes perpendicular to the mean wind. The influence of flow retardation on the convection of turbulence through the turbine is also modeled. Illustrative calculations are presented for the VAWT 34-m Test Bed currently in operation at Bushland, Texas.

Though the model's quantitative predictions remain to be validated by comparison with experimental data, the following qualitative conclusions have been drawn:

- The effects of turbulence do not “average out to zero”. The ensemble-averaged load distributions *vs.* θ do not coincide with the periodic variations produced by a steady mean wind. This is the result of aerodynamic nonlinearities. Hence, deviations of predicted steady-state performance from measured data should not *necessarily* be ascribed to deficiencies in the aerodynamic model. For a meaningful comparison, the predicted loads should account for the presence of turbulence.
- The ensemble-averaged load distributions tend to be smoother than a steady-state analysis would predict—the peaks are lower, and the valleys higher. However, the *instantaneous* load-time histories, which are responsible for blade fatigue, exhibit significant high-amplitude, high-frequency excursions about the ensemble-average.
- Turbulence introduces broadband excitation in the loading power spectral density (PSD) between the “per rev” frequencies ($B\Omega$ and its harmonics). At low tip-speed ratios, turbulence acts to reduce the excitation at the per rev frequencies. At moderate to high tip-speed ratios, some of the higher harmonics are reduced, while others are increased.
- The effects noted above become more pronounced as turbulence intensity increases.
- An unexpected finding is that for low tip-speed ratios (high winds), output power decreases slightly with increasing turbulence intensity, while for tip-speed ratios near the maximum C_p (low to moderate winds), power increases as the turbulence level is raised. A heuristic analysis has been developed that explains these seemingly contradictory results in a qualitative sense. Whether such behavior truly reflects the real world remains to be seen.

The above conclusions are tempered somewhat by the uncertainty associated with use of the Gormont stall model[16], which is felt to be the weakest link in the present analysis. As noted earlier, Gregorek and Hoffman[18] have carried out extensive investigations of the unsteady characteristics of VAWT-type airfoil sections. Work is underway on compiling and analyzing this data; it is hoped this will lead to a better understanding of the basic fluid mechanics involved, and suggest means for improving the fidelity of empirical models such as Gormont's for use in practical design codes.

There is a need for experimental data against which stochastic simulations such as those presented here may be quantitatively compared. Such comparisons would require *simultaneous* measurements of turbulence properties and, at the very least, rotor torque, preferably azimuthally resolved. Ideally, measurements of the local aerodynamic loads at several representative spanwise stations would be performed as well. To be meaningful, data should be averaged over a time interval several times the period of the lowest energy-bearing frequencies in the turbulence. The mean wind, turbulence intensity and PSD would all need to be constant for the duration of the measurements. Such conditions would be difficult if not impossible to achieve in the field, where the experimenter has little control over the vagaries of the weather. Perhaps a sub-scale wind tunnel investigation is the best hope of obtaining data useful for validating models such as that presented here.

The reader is reminded that we have chosen to focus on the fluid dynamic aspects of the problem. Accordingly, the integrated rotor torque was examined as a global indicator of the influence of turbulence on VAWT aerodynamics. Fatigue predictions require attention to the local loads, and their distribution in space as well as time (frequency). Though these are predicted by the present simulation as well, a detailed discussion of the influence of turbulence on blade fatigue is beyond the scope of this report. More comprehensive simulations, which allow the predicted loads of this model to serve as input to structural analyses of the turbine, are currently being developed.

REFERENCES

1. Dragt, J. B., "Load Fluctuations and Response of Rotor Systems in Turbulent Wind Fields," presented at *Windpower '85 Conference*, San Francisco, August 1985.
2. Veers, P. S., *Modeling Stochastic Wind Loads on Vertical Axis Wind Turbines*, Sandia National Laboratories Report SAND83-1909, September 1984.
3. Anderson, M. B., Powles, S. J. R., and Bossanyi, E. A., "The Response of a Vertical Axis Wind Turbine to Fluctuating Aerodynamic Loads," presented at the *7th British Wind Energy Association Conference*, Oxford University, March 27-29, 1985.
4. Malcolm, D. J., "Modal Loading and Response of Darrieus Rotors in Turbulent Flow," presented at the *7th Annual VAWT Aerodynamics Seminar*, held at Bushland, Texas, April 23-24, 1987.
5. Homicz, G. F., "VAWT Stochastic Loads Produced by Atmospheric Turbulence," presented at the *7th ASME Wind Energy Symposium*, New Orleans, La., January 10-13, 1988, pp. 127-137.
6. Homicz, G. F., "VAWT Stochastic Loads Produced by Atmospheric Turbulence," *ASME Journal of Solar Energy Engineering*, Vol. 111, November 1989, pp.358-366.
7. Veers, P. S., *Three-Dimensional Wind Simulation*, Sandia National Laboratories Report SAND88-0152, March 1988.
8. Paraschivoiu, I., "Aerodynamic Loads and Performance of the Darrieus Rotor," *AIAA Journal of Energy*, Vol. 6, No. 6, November-December 1982, pp. 406-412.
9. Paraschivoiu, I., and Delclaux, F., "Double Multiple Streamtube Model with Recent Improvements," *AIAA Journal of Energy*, Vol. 7, No. 3, May-June 1983, pp. 250-255.
10. Paraschivoiu, I., "Predicted and Experimental Forces on the Darrieus Rotor," *AIAA Journal of Energy*, Vol. 7, No. 6, November-December 1983, pp. 610-615.
11. Strickland, J. H., Webster, B. T., and Nguyen, T., "A Vortex Model of the Darrieus Turbine: An Analytical and Experimental Study," *ASME Transactions, Journal of Fluids Engineering*, Vol. 101, December 1979, pp. 500-505.
12. Amos, G. W., and Bragg, G. M., "A Comparison of Analytic Prediction Methods for Vertical Axis Wind Turbines," *Proceedings of the European Wind Energy Conference*, held in Hamburg, Federal Republic of Germany, October 22-26, 1984.
13. Strickland, J. H., "A Review of Aerodynamic Analysis Methods for the Vertical-Axis Wind Turbine," *Proceedings of the 5th ASME Wind Energy Symposium, 9th Annual Energy Sources Technology Conference and Exhibition*, held in New Orleans, La., February 23-26, 1986, pp. 7-17.
14. Sheldahl, R. E., and Klimas, P. C., *Aerodynamic Characteristics of Seven Symmetrical Airfoil Sections Through 180-Degree Angle of Attack for Use in Aerodynamic Analysis of Vertical Axis Wind Turbines*, Sandia National Laboratories Report SAND80-2114, March 1981.
15. Berg, D. E., "An Improved Double-Multiple Streamtube Model for the Darrieus-Type Vertical Axis Wind Turbine," *6th Biennial Wind Energy Conference and Workshop*, Minneapolis, Minnesota, June 1-3, 1983.

16. Gormont, R. E., *An Analytical Model of Unsteady Aerodynamics and Radial Flow for Application to Helicopter Rotors*, U. S. Army Air Mobility Research and Development Laboratory Technical Report 72-67, prepared by the Boeing Company, Vertol Division, May 1973.
17. Massé, B., *Description de Deux Programmes d'Ordinateur pour le Calcul des Performances et des Charges Aérodynamiques pour les Éoliennes à Axe Vertical*, Institut de Recherche de l'Hydro-Québec, IREQ-2379, Quebec, Canada, July 1981.
18. Gregorek, G. M., and Hoffmann, M. T., "Dynamic Stall Measurements on Wind Turbine Airfoils," *Proceedings of the 6th ASME Wind Energy Symposium*, held in Dallas, Texas, February 15-18, 1987.
19. Frost, W., Long, D. H., and Turner, R. E., *Engineering Handbook on the Atmospheric Environment Guideline for Use in Wind Turbine Generator Development*, NASA TP-1379, December 1978.
20. Hildebrand, F. B., *Introduction to Numerical Analysis*, 2nd edition, McGraw-Hill, 1974.
21. Thresher, R. W., Holley, W. E., Smith, C. E., Jafarey, N., and Lin, S.-R., *Modeling the Response of Wind Turbines to Atmospheric Turbulence*, Mechanical Engineering Department, Oregon State University. U. S. Department of Energy Report DOE/ET/23144-81/2, prepared for Pacific Northwest Laboratory, August, 1981.
22. Thresher, R. W., Holley, W. E., Hershberg, E. L., and Lin, S.-R., *Response of the MOD-0A Wind Turbine Rotor to Turbulent Atmospheric Wind*, Mechanical Engineering Department, Oregon State University. U. S. Department of Energy Report DOE/RL/10378-82/1, prepared for Pacific Northwest Laboratory, October, 1983.
23. Powell, D. C., and Connell, J. R., *A Model for Simulating Rotational Data for Wind Turbine Applications*, Pacific Northwest Laboratory Report PNL-5857, April, 1986.
24. Walker, S. N., Weber, T. L., and Wilson, R. E., *State-of-the-Art in Turbulence Simulation*, Department of Mechanical Engineering, Oregon State University. Report prepared for Midwest Research Institute, Solar Energy Research Institute Division, July, 1988.
25. Shinozuka, M., and Jan, C.-M., "Digital Simulation of Random Processes and Its Applications," *Journal of Sound and Vibration*, Vol. 25, No. 1, 1972, pp. 11-128.
26. Kaimal, J. C., "Turbulence Spectra, Length Scales and Structure Parameters in the Stable Surface Layer," *Boundary-Layer Meteorology*, Vol. 4, 1973, pp. 289-309.
27. Strickland, J. H., *VAWT Stochastic Wind Simulator*, Sandia National Laboratories Report SAND87-0501, April 1987.
28. Campbell, C. W., "Monte Carlo Turbulence Simulation Using Rational Approximations to von Kármán Spectra," *AIAA Journal*, Vol. 24, No. 1, January 1986, pp. 62-66.
29. Bendat, J. S., and Piersol, A. G., *Random Data: Analysis and Measurement Procedures*, John Wiley & Sons, Inc., New York, 1971.
30. Solari, G., "Turbulence Modeling for Gust Loading," *ASCE Journal of Structural Engineering*, Vol. 113, No. 7, July 1987, pp. 1550-1569.
31. Taylor, G. I., "The Spectrum of Turbulence," *Proceedings of the Royal Society of London*, Series A, Vol. 164, 1938, pp. 476-490.

16. Gormont, R. E., *An Analytical Model of Unsteady Aerodynamics and Radial Flow for Application to Helicopter Rotors*, U. S. Army Air Mobility Research and Development Laboratory Technical Report 72-67, prepared by the Boeing Company, Vertol Division, May 1973.
17. Massé, B., *Description de Deux Programmes d'Ordinateur pour le Calcul des Performances et des Charges Aérodynamiques pour les Éoliennes à Axe Vertical*, Institut de Recherche de l'Hydro-Québec, IREQ-2379, Quebec, Canada, July 1981.
18. Gregorek, G. M., and Hoffmann, M. T., "Dynamic Stall Measurements on Wind Turbine Airfoils," *Proceedings of the 6th ASME Wind Energy Symposium*, held in Dallas, Texas, February 15-18, 1987.
19. Frost, W., Long, D. H., and Turner, R. E., *Engineering Handbook on the Atmospheric Environment Guideline for Use in Wind Turbine Generator Development*, NASA TP-1379, December 1978.
20. Hildebrand, F. B., *Introduction to Numerical Analysis*, 2nd edition, McGraw-Hill, 1974.
21. Thresher, R. W., Holley, W. E., Smith, C. E., Jafarey, N., and Lin, S.-R., *Modeling the Response of Wind Turbines to Atmospheric Turbulence*, Mechanical Engineering Department, Oregon State University. U. S. Department of Energy Report DOE/ET/23144-81/2, prepared for Pacific Northwest Laboratory, August, 1981.
22. Thresher, R. W., Holley, W. E., Hershberg, E. L., and Lin, S.-R., *Response of the MOD-0A Wind Turbine Rotor to Turbulent Atmospheric Wind*, Mechanical Engineering Department, Oregon State University. U. S. Department of Energy Report DOE/RL/10378-82/1, prepared for Pacific Northwest Laboratory, October, 1983.
23. Powell, D. C., and Connell, J. R., *A Model for Simulating Rotational Data for Wind Turbine Applications*, Pacific Northwest Laboratory Report PNL-5857, April, 1986.
24. Walker, S. N., Weber, T. L., and Wilson, R. E., *State-of-the-Art in Turbulence Simulation*, Department of Mechanical Engineering, Oregon State University. Report prepared for Midwest Research Institute, Solar Energy Research Institute Division, July, 1988.
25. Shinozuka, M., and Jan, C.-M., "Digital Simulation of Random Processes and Its Applications," *Journal of Sound and Vibration*, Vol. 25, No. 1, 1972, pp. 11-128.
26. Kaimal, J. C., "Turbulence Spectra, Length Scales and Structure Parameters in the Stable Surface Layer," *Boundary-Layer Meteorology*, Vol. 4, 1973, pp. 289-309.
27. Strickland, J. H., *VAWT Stochastic Wind Simulator*, Sandia National Laboratories Report SAND87-0501, April 1987.
28. Campbell, C. W., "Monte Carlo Turbulence Simulation Using Rational Approximations to von Kármán Spectra," *AIAA Journal*, Vol. 24, No. 1, January 1986, pp. 62-66.
29. Bendat, J. S., and Piersol, A. G., *Random Data: Analysis and Measurement Procedures*, John Wiley & Sons, Inc., New York, 1971.
30. Solari, G., "Turbulence Modeling for Gust Loading," *ASCE Journal of Structural Engineering*, Vol. 113, No. 7, July 1987, pp. 1550-1569.
31. Taylor, G. I., "The Spectrum of Turbulence," *Proceedings of the Royal Society of London*, Series A, Vol. 164, 1938, pp. 476-490.

32. Connell, J. R., and Morris, V. R., "Turbulent Wind at the Equatorial Segment of an Operating Darrieus Wind Turbine Blade," *Proceedings of the 9th ASME Wind Energy Symposium*, held in New Orleans, Louisiana, January 14-18, 1990
33. Gregorek, G. M., and Klimas, P. C., "Tailored Airfoils for Wind Turbine Applications," *Proceedings of the 6th ASME Wind Energy Symposium*, held in Dallas, Texas, February 15-18, 1987.
34. Berg, D. E., *Structural Design of the Sandia 34-Meter Vertical-Axis Wind Turbine*, Sandia National Laboratories Report SAND84-1287, April 1985.
35. Berg, D. E., and Ashwill, T. D., "An Update on the Structural Design of the Sandia 34-M Vertical Axis Wind Turbine," *Proceedings of the 5th ASME Wind Energy Symposium*, held in New Orleans, Louisiana, February 23-26, 1986.
36. Reda, D. C., "Observations of Dynamic Stall Phenomena on the SAND 0018/50 Airfoil with Shear Stress Sensitive Liquid Crystal Coatings," *Proceedings of the 9th ASME Wind Energy Symposium*, held in New Orleans, LA, January 14-17, 1990.
37. Lobitz, D. W., and Sullivan, W. N., *A Comparison of Finite Element Predictions and Experimental Data for the Forced Response of the DOE 100 kw Vertical-Axis Wind Turbine*, Sandia National Laboratories Report SAND82-2534, February 1984.
38. de Vries, O., *Fluid Dynamic Aspects of Wind Energy Conversion*, AGARDograph No. 243, North Atlantic Treaty Organization, Advisory Group for Aerospace Research and Development, July, 1979.
39. Haskell, K.H., Vandevender, W. H., and Walton, E. L., *The SLATEC Common Mathematical Subprogram Library: SNLA Implementation*, Sandia National Laboratories Report SAND80-2792, 1980.
40. Hansen, A. C., "Turbulence and Wind Turbine Performance," *Proceedings of the ASCE, Transportation Engineering Journal*, Vol. 106, No. TE6, November 1980, pp. 675-683.
41. Swift, A., and Kirkland, M., "The Effects of Turbulence on the Performance of Both Variable and Constant Rotor Speed Wind Turbines," *Proceedings of the 4th ASME Wind Energy Symposium*, held in Dallas, Texas, February 17-21, 1985, pp. 131-138.

EXTERNAL DISTRIBUTION:

D. K. Ai
Alcoa Technical Center
Aluminum Company of America
Alcoa Center, PA 15069

Dr. R. E. Akins
Washington & Lee University
P.O. Box 735
Lexington, VA 24450

The American Wind Energy Association
777 N. Capitol Street, NE
Suite 805
Washington, DC 20002

Dr. Mike Anderson
VAWT, Ltd.
1 St. Albans
Hemel Hempstead
Herts HP2 4TA
UNITED KINGDOM

Dr. M. P. Ansell
School of Material Science
University of Bath
Claverton Down
Bath BA2 7AY
Avon
UNITED KINGDOM

Holt Ashley
Dept. of Aeronautics and Astronautics
Stanford University
Stanford, CA 94305

K. Bergey
University of Oklahoma
Aero Engineering Department
Norman, OK 73069

Ir. Jos Beurskens
Programme Manager for Renewable Energies
Netherlands Energy Research
Foundation ECN
Westerduinweg 3
P.O. Box 1
1755 ZG Petten (NH)
THE NETHERLANDS

J. R. Birk
Electric Power Research Institute
3412 Hillview Avenue
Palo Alto, CA 94304

N. Butler
Bonneville Power Administration
P.O. Box 3621
Portland, OR 97208

Monique Carpentier
Energy, Mines and Resources
Renewable Energy Branch
460 O'Connor Street
Ottawa, Ontario K1A 0E4
CANADA

Dr. R. N. Clark
USDA
Agricultural Research Service
Southwest Great Plains Research Center
Bushland, TX 79012

Otto de Vries
National Aerospace Laboratory
Anthony Fokkerweg 2
Amsterdam 1017
THE NETHERLANDS

E. A. DeMeo
Electric Power Research Institute
3412 Hillview Avenue
Palo Alto, CA 94304

C. W. Dodd
Universal Data Systems
5000 Bradford Drive
Huntsville, AL 35805

J. B. Dragt
Physics Department
Netherlands Energy Research Foundation
(E.C.N.)
Westerduinweg 3 Petten (NH)
THE NETHERLANDS

A. J. Eggers, Jr.
RANN, Inc.
260 Sheridan Ave., Suite 414
Palo Alto, CA 94306

John Ereaux
RR No. 2
Woodbridge, Ontario L4L 1A6
CANADA

Dr. R. A. Galbraith
Dept. of Aerospace Engineering
James Watt Building
University of Glasgow
Glasgow G12 8QG
Scotland

A. D. Garrad
Garrad Hasson
9-11 Saint Stephens Street
Bristol BS1 1EE
ENGLAND

P. R. Goldman
Wind/Hydro/Ocean Division
U.S. Department of Energy
1000 Independence Avenue
Washington, DC 20585

Dr. I. J. Graham
Dept. of Mechanical Engineering
Southern University
P.O. Box 9445
Baton Rouge, LA 70813-9445

Professor G. Gregorek
Aeronautical & Astronautical Dept.
Ohio State University
2300 West Case Road
Columbus, OH 43220

Professor N. D. Ham
Aero/Astro Dept.
Massachusetts Institute of Technology
77 Massachusetts Avenue
Cambridge, MA 02139

Loretta Helling
Librarian
National Atomic Museum
Albuquerque, NM 87185

T. Hillesland
Pacific Gas and Electric Co.
3400 Crow Canyon Road
San Ramon, CA 94583

Eric N. Hinrichsen
Power Technologies, Inc.
P.O. Box 1058
Schenectady, NY 12301-1058

W. E. Holley
U.S. WindPower
6952 Preston Avenue
Livermore, CA 94550

M. A. Ilyan
Pacific Gas and Electric Co.
3400 Crow Canyon Road
San Ramon, CA 94583

K. Jackson
Dynamic Design
123 C Street
Davis, CA 95616

O. Krauss
Division of Engineering Research
Michigan State University
East Lansing, MI 48825

V. Lacey
Indal Technologies, Inc.
3570 Hawkestone Road
Mississauga, Ontario L5C 2V8
CANADA

A. Laneville
Faculty of Applied Science
University of Sherbrooke
Sherbrooke, Quebec J1K 2R1
CANADA

G. G. Leigh
New Mexico Engineering Research Institute
Campus P.O. Box 25
Albuquerque, NM 87131

L. K. Liljegren
120 East Penn Street
San Dimas, CA 91773

R. R. Loose, Director
Wind/Hydro/Ocean Division
U.S. Department of Energy
1000 Independence Ave., SW
Washington, DC 20585

Robert Lynette
R. Lynette & Assoc., Inc.
15042 NE 40th Street
Suite 206
Redmond, WA 98052

Peter Hauge Madsen
Riso National Laboratory
Postbox 49
DK-4000 Roskilde
DENMARK

David Malcolm
Lavalin Engineers, Inc.
Atria North - Phase 2
2235 Sheppard Avenue East
Willowdale, Ontario M2J 5A6
CANADA

Bernard Masse
Institut de Recherche d'Hydro-Quebec
1800, Montee Ste-Julie
Varenes, Quebec J3X 1S1
CANADA

Gerald McNerney
U.S. Windpower, Inc.
6952 Preston Avenue
Livermore, CA 94550

R. N. Meroney
Dept. of Civil Engineering
Colorado State University
Fort Collins, CO 80521

Alan H. Miller
10013 Tepopa Drive
Oakdale, CA 95361

D. Morrison
New Mexico Engineering Research Institute
Campus P.O. Box 25
Albuquerque, NM 87131

V. Nelson
Department of Physics
West Texas State University
P.O. Box 248
Canyon, TX 79016

J. W. Oler
Mechanical Engineering Dept.
Texas Tech University
P.O. Box 4289
Lubbock, TX 79409

Dr. D. I. Page
Energy Technology Support Unit
B 156.7 Harwell Laboratory
Oxfordshire, OX11 0RA
UNITED KINGDOM

Ion Paraschivoiu
Dept. of Mechanical Engineering
Ecole Polytechnique
CP 6079
Succursale A
Montreal, Quebec H3C 3A7
CANADA

Troels Friis Pedersen
Riso National Laboratory
Postbox 49
DK-4000 Roskilde
DENMARK

Helge Petersen
Riso National Laboratory
Postbox 49
DK-4000 Roskilde
DENMARK

Dr. R. Ganesh Rajagopalan
Assistant Professor
Aerospace Engineering Department
Iowa State University
404 Town Engineering Bldg.
Ames, IA 50011

R. Rangi
Low Speed Aerodynamics Laboratory
NRC-National Aeronautical Establishment
Montreal Road
Ottawa, Ontario K1A 0R6
CANADA

Markus G. Real, President
Alpha Real Ag
Feldeggstrasse 89
CH 8008 Zurich
Switzerland

R. L. Scheffler
Research and Development Dept.
Room 497
Southern California Edison
P.O. Box 800
Rosemead, CA 91770

L. Schienbein
FloWind Corporation
1183 Quarry Lane
Pleasanton, CA 94566

Thomas Schweizer
Princeton Economic Research, Inc.
12300 Twinbrook Parkway
Rockville, MD 20852

David Sharpe
Dept. of Aeronautical Engineering
Queen Mary College
Mile End Road
London, E1 4NS
UNITED KINGDOM

J. Sladky, Jr.
Kinetics Group, Inc.
P.O. Box 1071
Mercer Island, WA 98040

M. Snyder
Aero Engineering Department
Wichita State University
Wichita, KS 67208

L. H. Soderholm
Agricultural Engineering
Room 213
Iowa State University
Ames, IA 50010

Peter South
ADECON
6535 Millcreek Dr., Unit 67
Mississauga, Ontario L5N 2M2
CANADA

W. J. Steeley
Pacific Gas and Electric Co.
3400 Crow Canyon Road
San Ramon, CA 94583

Forrest S. Stoddard
West Texas State University
Alternative Energy Institute
WT Box 248
Canyon, Texas 79016

Derek Taylor
Alternative Energy Group
Walton Hall
Open University
Milton Keynes MK7 6AA
UNITED KINGDOM

G. P. Tennyson
DOE/AL/ETWMD
Albuquerque, NM 87115

Walter V. Thompson
410 Ericwood Court
Manteca, CA 95336

R. W. Thresher
Solar Energy Research Institute
1617 Cole Boulevard
Golden, CO 80401

K. J. Touryan
3701 Hawkins Street, NE
Albuquerque, NM 87109-4512

W. A. Vachon
W. A. Vachon & Associates
P.O. Box 149
Manchester, MA 01944

P. Vittecoq
Faculty of Applied Science
University of Sherbrooke
Sherbrooke, Quebec J1K 2R1
CANADA

T. Watson
Canadian Standards Association
178 Rexdale Boulevard
Rexdale, Ontario M9W 1R3
CANADA

L. Wendell
Battelle-Pacific Northwest Laboratory
P.O. Box 999
Richland, WA 99352

W. Wentz
Aero Engineering Department
Wichita State University
Wichita, KS 67208

R. E. Wilson
Mechanical Engineering Dept.
Oregon State University
Corvallis, OR 97331

INTERNAL DISTRIBUTION:

400	R. C. Maydew	6225	H. M. Dodd (50)
		6225	T. D. Ashwill
1510	J. C. Cummings	6225	D. E. Berg
1514	J. G. Arguello	6225	S. C. Newton
1514	H. S. Morgan	6225	M. A. Rumsey
1540	J. R. Asay	6225	L. L. Schluter
1544	K. E. Metzinger	6225	W. A. Stephenson
1544	E. D. Reedy	6225	H. J. Sutherland
1544	R. C. Reuter, Jr.	6225	P. S. Veers
1545	C. R. Dohrmann		
1545	D. W. Lobitz	7543	G. H. James III
1545	D. R. Martinez	7543	R. Rodeman
1550	C. W. Peterson	7543	T. G. Carne
1551	J. K. Cole	7543	J. P. Lauffer
1552	D. D. McBride		
1552	J. H. Strickland	8523	R. C. Christman
1553	W. L. Hermina		
1554	D. P. Aeschliman		
1555	W. P. Wolfe		
1556	W. L. Oberkampf		
1556	G. F. Homicz (20)		
3141	S. A. Landenberger (5)		
3145	Document Processing for DOE/OSTI (8)		
3151	G. C. Claycomb (3)		
3161	P. S. Wilson		
6000	V. L. Dugan, Acting		
6200	B. W. Marshall, Acting		
6220	D. C. Schueler		